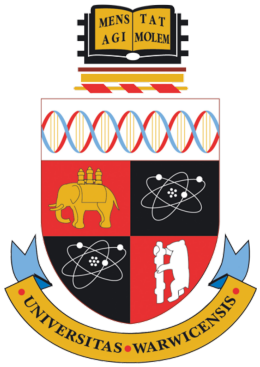

Multifunctional Scanning Ion Conductance Microscopy

by

Ashley Page

Thesis

Submitted to the University of Warwick

for the degree of

Doctor of Philosophy

Supervisor: Prof. Patrick R. Unwin

MOAC Doctoral Training Centre

September 2017

For Geraldine, Michael and Emily

Contents

List of Figures

List of Tables

Abbreviations

2D	Two-Dimensional
3D	Three-Dimensional
AC	Alternating Current
AFM	Atomic Force Microscopy
BM-SICM	Bias Modulated Scanning Ion Conductance Microscopy
CF	Carbon Fiber
CV	Cyclic Voltammogram
CVD	Chemical Vapour Deposition
DC	Direct Current
DI	Deionized (Water)
DM-SICM	Distance Modulation-Scanning Ion Conductance Microscopy
DNA	Deoxyribonucleic Acid
DTC	Doctoral Training Centre
EDL	Electrical Double Layer
EFM	Electrostatic Force Microscopy
EOF	Electroosmotic Flow
EPSRC	Engineering and Physical Sciences Research Council
FE-SEM	Field Emission Scanning Electron Microscopy
FEM	Finite Element Method (Modelling)
FIB	Focussed Ion Beam (Milling)
FluidFM	Fluid Force Microscopy
FPGA	Field-Programmable Gate Array
GC	Gouy-Chapman
ICR	Ion Current Rectification
IHP	Inner Helmholtz Plane
KPFM	Kelvin Probe Force Microscopy
MOAC	Molecular Organisation and Assembly in Cells
NP	Nanoparticle
OHP	Outer Helmholtz Plane
ORR	Oxygen Reduction Reaction
P-SICM	Potentiometric Scanning Ion Conductance Microscopy
PC12	Pheochromocytoma-12 (Cell Line)

QRCE	Quasi-Reference Counter Electrode
RPMI	Roswell Park Memorial Institute (Medium)
SCE	Saturated Calomel Electrode
SECCM	Scanning Electrochemical Cell Microscopy
SECM	Scanning Electrochemical Microscopy
SEM	Scanning Electron Microscopy
SEPM	Scanning Electrochemical Probe Microscopy
SICM	Scanning Ion Conductance Microscopy
SIR	Surface-Induced Rectification
SPM	Scanning Probe Microscopy
SPR	Surface Plasmon Resonance
STM	Scanning Tunnelling Microscopy
STP	Standard Temperature and Pressure
TEM	Transmission Electron Microscopy
UHV	Ultra-High Vacuum
UME	Ultramicroelectrode
ΔC-SICM	Differential Concentration Scanning Ion Conductance Microscopy

Acknowledgements

First and foremost, I would like to thank my supervisor Prof. Patrick R. Unwin for his advice and encouragement throughout the course of my Ph.D. His enthusiasm, be it for research, music, or running, has provided a constant source of inspiration over the last three years.

I would like to acknowledge the MOAC DTC via the EPSRC for both their funding and their support. Thank you in particular to the MOAC 2013 cohort for making our various trips to conferences and transferable skills courses so enjoyable, and to Naomi Grew for keeping us all on track when it seems so easy to fall off.

Finally, thank you to everyone in the Warwick Electrochemistry and Interfaces Group, particularly to Dr. David Perry, Minkyung Kang and Dr. Dmitry Momotenko, without whom much of the work in this thesis could not have been completed. Thank you also to all former group members and those in the Chemistry workshops who contributed to the WEC-SPM platform; your work now facilitates all of the research we have been able to do.

Declaration

The work presented in this thesis is entirely my own work, except where acknowledged at the beginning of each chapter. I confirm that this thesis has not been submitted for a degree at another university. This work is being submitted for thesis by publication.

Chapter 2 was published as:

Quantitative Visualization of Molecular Delivery and Uptake at Living Cells with Self-Referencing Scanning Ion Conductance Microscopy-Scanning Electrochemical Microscopy.

Ashley Page, Minkyung Kang, Alexander Armitstead, David Perry, and Patrick R. Unwin, *Anal. Chem.* **2017**, *89*, 3021-3028. This manuscript also appeared in the thesis of Minkyung Kang.

Chapter 3 was published as:

Fast Nanoscale Surface Charge Mapping with Pulsed-Potential Scanning Ion Conductance Microscopy.

Ashley Page, David Perry, Philip Young, Daniel Mitchell, Bruno G. Frenguelli, and Patrick R. Unwin, *Anal. Chem.* **2016**, *88*, 10854-10859. This manuscript also appeared in the thesis of Dr. David Perry.

Chapter 4 has been submitted as an article to *Analytical Chemistry* as:

Differential-Concentration Scanning Ion Conductance Microscopy.

David Perry, **Ashley Page**, Baoping Chen, Bruno G. Frenguelli, and Patrick R. Unwin, *Anal. Chem.* **2017**, submitted.

Chapter 5 was published as:

Write–Read 3D Patterning with a Dual-Channel Nanopipette.

Dmitry Momotenko, **Ashley Page**, Maria Adobes-Vidal, and Patrick R. Unwin, *ACS Nano*, **2016**, *10*, 8871-8878.

In addition to the above, I have contributed to the following publications that are not included in this thesis:

Surface Charge Visualization at Viable Living Cells.
David Perry, Binoy Paulose Nadappuram, Dmitry Momotenko, Philip D. Voyias, **Ashley Page**, Gyanendra Tripathi, Bruno G. Frenguelli, and Patrick R. Unwin, *J. Am. Chem. Soc.*, **2016**, *138*, 3152-3160.

Electrochemical Control of Calcium Carbonate Crystallization and Dissolution in Nanopipettes.
David Perry, Alexander S. Parker, **Ashley Page**, and Patrick R. Unwin, *ChemElectroChem*, **2016**, *3*, 2212-2220.

Simultaneous Topography and Reaction Flux Mapping At and Around Electrocatalytic Nanoparticles.
Minkyung Kang, David Perry, Cameron L. Bentley, Geoff West, **Ashley Page**, and Patrick R. Unwin, *ACS Nano*, **2017**, 10.1021/acsnano.7b05435.

And the following review articles:

Frontiers in Nanoscale Electrochemical Imaging: Faster, Multifunctional, and Ultrasensitive.
Minkyung Kang, Dmitry Momotenko, **Ashley Page**, David Perry, and Patrick R. Unwin, *Langmuir*, **2016**, *32*, 7993-8008.

Multifunctional Scanning Ion Conductance Microscopy.
Ashley Page, David Perry, and Patrick R. Unwin, *Proc. Roy. Soc. A*, **2017**, *473*, 20160889.

Abstract

Scanning ion conductance microscopy (SICM) is a nanopipette-based technique that has historically been used for the topographical imaging of soft samples. This thesis demonstrates the development of SICM into a multifunctional tool, capable of providing a host of additional information about both biological and inert samples, whilst maintaining the structural mapping capability for which it is usually employed.

Two approaches are taken to extend the functionality of SICM: (i) designing sophisticated potential, and positional, control functions that are then used with traditional single-channel nanopipettes; and (ii) incorporating an ion conductance channel into a multi-barrelled probe. In the single-channel setup, a pulsed-potential profile allows the extraction of surface charge density on extended substrates, and a ramped-potential profile permits spatially resolved mapping of redox reactions on an electrode substrate. When integrated into a more complex probe, SICM is used to study molecular uptake at cellular surfaces, and to print Cu microstructures on a Au substrate. While this thesis is primarily concerned with technique development, the studies herein have broad applications in cell biology, pharmaceuticals, materials science and beyond.

In addition to developing imaging modes that allow the extraction of functional information at a surface, this thesis also contributes to the fundamental understanding of the SICM system. Finite element method simulations are performed alongside experimental studies, in order to fully understand the contributions of the pipette geometry, ion current rectification, and pipette-surface interactions on the measured ionic current. The theoretical treatment herein provides a foundation upon which future multifunctional SICM regimes could be designed, extending the scope of this increasingly powerful technique.

1 Introduction

1.1 Thesis Summary

This thesis is concerned with the advancement of scanning ion conductance microscopy (SICM), a scanning electrochemical probe technique first introduced by Hansma et al. in 1989.[1] While SICM has typically been used for topographical imaging, this thesis focuses on the extension of its capabilities as an ever-more powerful tool for the investigation both of surfaces, and of ionic fluxes more generally. The additional functionality brought to SICM by the studies herein include the incorporation of SICM into a probe to map molecular uptake, the improvement of SICM as a tool for surface charge mapping, and the use of the SICM nanopipette to locally deliver and deposit Cu ions to print solid structures. Each chapter of the thesis has either been published or submitted to a peer-reviewed journal, and is thus presented in a manuscript format complete with supporting information. Contrary to the typical thesis layout, this means that each chapter contains introduction, experimental and conclusion sections and thus constitutes a complete piece of work.

Chapter 2 demonstrates the combination of SICM with scanning electrochemical microscopy (SECM) into a single probe in a technique known as SICM-SECM.[2] The SICM channel of this double-barrelled probe is then used both for topographical feedback and for the local delivery of a molecule of interest. The SECM channel monitors the local concentration of that molecule as the probe approaches a surface, with the SECM current dependent on the rate of molecular uptake at the cellular substrate. This response is then quantified using finite element method (FEM) modelling that allows the correspondence of the experimental SECM current to a theoretical uptake rate at the surface.

Chapter 3 of this thesis concerns the development of a new scanning regime for the use of SICM as a tool for surface charge mapping.[3] By improving both the approach rate of the probe towards the surface, and the potential control function used to extract surface charge information, the pixel acquisition rate of the technique increases by an order of magnitude. This enhancement of the scanning speed allows for the collection of images with a significantly higher pixel density, increasing the

viability of SICM as a technique for spatially resolved nanoscale surface charge mapping.

The typical SICM setup (in which both the pipette and the bath contain the same solution) is perturbed in Chapter 4, in which the effect of having solutions of differing ionic strength in the tip and the bath is explored. This study demonstrates that SICM can operate at zero applied bias, as well as in a setup in which the junction potential at the end of the nanopipette is the only driving force. This new approach to SICM is capable of both surface charge and local reaction mapping with equal or superior sensitivity to the standard setup. The additional benefit of a significantly lower electric field at the end of the nanopipette is also explored using FEM simulations.

Chapter 5 demonstrates the use of a double-barrel open nanopipette for the deposition of sub-micron Cu structures on a Au surface.[4] One channel is used as a source of Cu^{2+} ions, while the other is used for topographical feedback, allowing the probe to operate as a nanoscopic 3D printer. The technique is used to deposit high aspect ratio pillars, as well as Γ-like and zig-zag features that are subsequently imaged using a scanning electron microscope (SEM). The SICM capabilities of the probe are then utilised to create high-resolution topographical images of the deposits. The final chapter summarises and contextualises the studies herein, providing an insight into the possible applications of SICM in future studies.

1.2 Scanning Probe Microscopy

Scanning probe microscopy (SPM) differs significantly from conventional microscopy in that it does not irradiate the sample, but instead uses a physical probe to build up an image by moving over the surface.[5] There are many different kinds of SPM, each of which relies on some interaction between the probe and the surface that is being imaged. In many cases, the information collected may be simply the surface topography, though some scanning probes are capable of investigating other interfacial properties such as charge or porosity.

One of the earliest examples of SPM is the scanning tunnelling microscope (STM, Figure 1.1a),[6] which can be used to build atomic-resolution topographical images of a surface. It relies on the quantum tunnelling of electrons across the gap between an atomically fine tip and the surface to generate a feedback mechanism

known as the tunnelling current.[5–7] This current is then maintained at a constant level as the probe is scanned over the surface. Atomic force microscopy (AFM, Figure 1.1b) uses the deflection of a cantilever to detect the presence of a surface; via either the attractive or repulsive forces between a tip mounted on that cantilever and the surface itself.[8,9] In addition to the topographical imaging for which it is best known, AFM can also be used to conduct force measurements at a surface.[10–12] While for the majority of scanning regimes the resolution of AFM is typically not as high as in STM, it is still several orders of magnitude higher than what could be achieved with an optical microscope.[13–15]

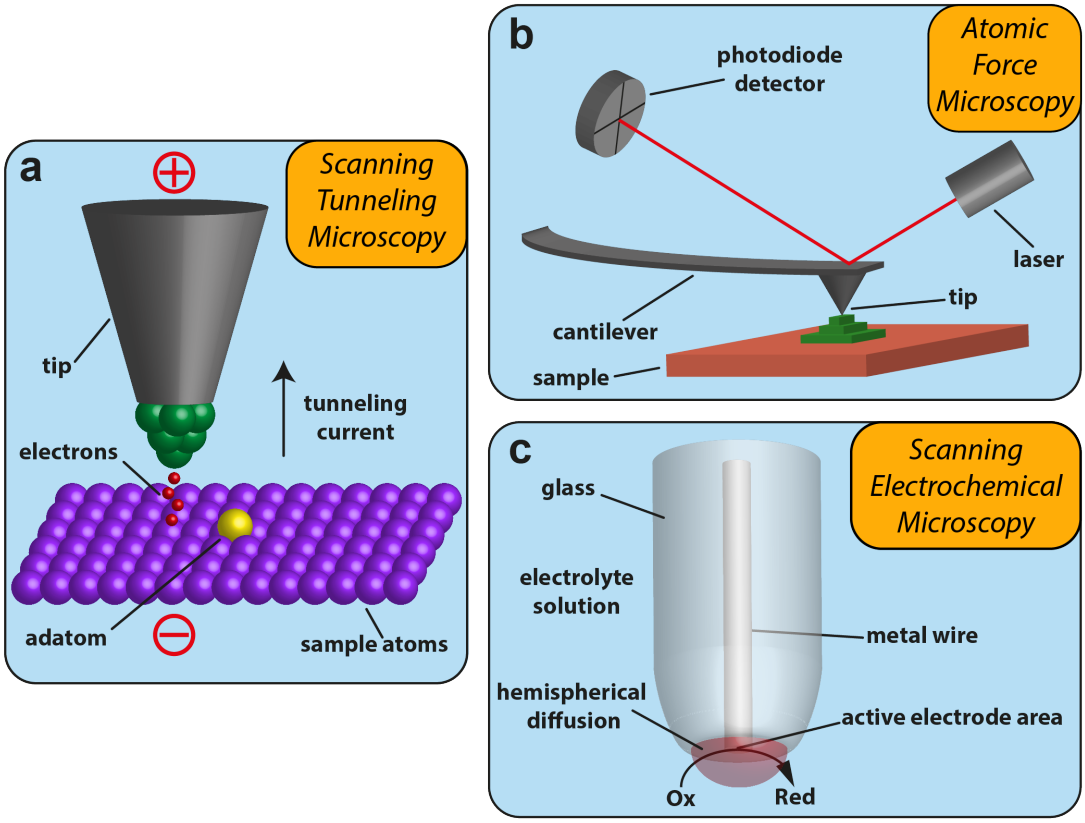

Figure 1.1. Scanning probe microscopy techniques. (a) Scanning tunnelling microscopy, in which an atomically-sharp conducting tip is brought close enough to a surface to allow electrons to tunnel across the gap. (b) Atomic force microscopy, in which a tip is mounted on a cantilever and scanned over a surface, with deflection monitored using a laser feedback system. (c) Scanning electrochemical microscopy, in which a microscale wire sealed in a glass sheath is used to detect the local concentration of an electrochemical species.

Within the family of all SPMs, some techniques, known as scanning electrochemical probe microscopies (SEPMs) use an electrochemical signal to detect a surface. This subfamily includes open-channel techniques such as SICM[1,16,17] and droplet-based techniques such as scanning electrochemical cell microscopy (SECCM),[18–21] though by far the most widely used since its inception in 1989 has been SECM (Figure 1.1c).[22–25] The SECM probe is constructed by sealing a thin conducting wire (typically a metal such as Pt or Au but may be carbon fiber) of diameter 1-25 μm inside a glass sheath. The glass is then polished back to reveal the disc-shaped cross section of the wire, creating a probe known as an ultramicroelectrode (UME).[26] The UME is then used as a working electrode for an electrochemical reaction (i.e. an oxidation or a reduction), and the faradaic current measured. As this current is dependent on the local concentration of an electrochemical species, the probe can be scanned over a surface to build up either a topographical or functional image.[24,27–30]

Each of the different scanning probe techniques has several advantages and disadvantages. For example, STM can provide some of the highest resolution images, the samples studied often requirement an ultra-high vacuum (UHV). AFM does not require an UHV, but contact between the probe and the sample makes most imaging modes (with non-contact AFM a notable exception) unsuitable for many applications in biological imaging. On the other hand, the SECM probe never comes into contact with the sample, and has thus been used extensively for live-cell studies.[28,31–35] SECM also opens up the possibility of functional imaging, and it has been used widely for the visualization of electrochemical activity on electrodes and other substrates.[30,36,37] However, SECM requires than the entire substrate be bathed in solution, something that is not desirable for all samples. Given the various advantages of different SPMs, efforts have been made to make hybrid probes that incorporate several techniques. One example of such a technique is SICM-SECM,[38–41] which allows simultaneous topographical and functional imaging in a single probe. Other hybrid techniques include AFM-SECM[42–45] and STM-SECM,[46,47] both of which aim to correlate structure and function using a single probe.

A common consideration for all SPMs is the resolution that they are able to achieve, as this determines the samples to which they can reasonably be applied. Of those SPMs described above, SECM typically has the lowest resolution due to the

difficulty of reliably fabricating sub-μm electrodes.[48] However, recent advances have seen some studies in which SECM is extended to the nanoscale.[49–54] Powerful piezoelectric positioning systems and smaller critical probe dimensions allow AFM to routinely achieve sub-nm resolution, and STM atomic resolution. A second consideration for SPMs is the speed of image acquisition; as the probe has to physically raster scan across the surface it can take anywhere from milliseconds to hours to obtain a single image. This often leads to a trade-off between image acquisition time and image quality that must be considered and optimised for the technique and substrate being imaged. Improving the rate of image acquisition in the use SICM for surface charge mapping is addressed in Chapter 3 of this thesis.

Scanning probe microscopy is a family of techniques that can provide significant topographical and functional information on both the micro- and nanoscale that is otherwise inaccessible with conventional microscopy. They have become integral to the study of many different systems at a diverse range of interfaces; a rise that is set to continue as their scope continues to widen.

1.3 Scanning Ion Conductance Microscopy

1.3.1 Operation: Scanning ion conductance microscopy (SICM) is a SEPM that utilises the current between two Ag/AgCl quasi-reference counter electrodes (QRCEs), one in a glass or quartz nanopipette and the other outside the nanopipette, as a feedback mechanism when scanning over a substrate (Figure 1.2a).[1,16,17] While SECM has been widely applied to functional imaging,[28,50,55] SICM has typically been used for topographical imaging, as the current flowing between the two electrodes is sensitive to the probe-substrate separation (Figure 1.2b,c). SICM is used to image a sample submerged in solution, and is commonly used for living cells.[56,57] Another characteristic that makes SICM particularly suitable to biological imaging is that, contrary to other SPMs, the probe never comes into contact with the sample, and thus living systems are not perturbed during scanning. The magnitude of the current between the two electrodes is determined by both the size of the opening of the nanopipette as well as the concentration of electrolyte. Typically, the same electrolyte composition is used in both the tip and the bath, and the high resistance at the end of the nanopipette governs the current magnitude. An exploration into the effects of deviating from such a setup comprises Chapter 4 of this thesis.

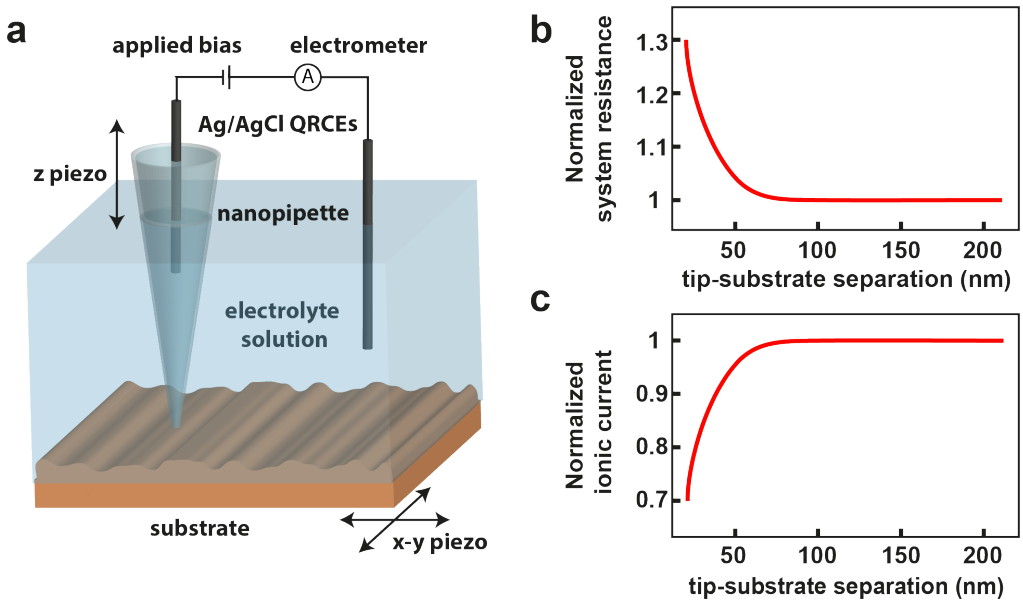

Figure 1.2. Operational principle of the scanning ion conductance microscope. In the basic SICM setup (a), a bias is applied between two Ag/AgCl electrodes, one in a glass or quartz nanopipette and the other in the bulk electrolyte solution. The nanopipette is translated normal to the surface using a piezoelectric positioner ('z piezo'), increasing the system resistance at small tip-substrate separations (b). The increase in system resistance induces a reduction in the ionic current measured at the electrometer (c). When scanning, the sample is moved laterally relative to the probe using a two-axis piezoelectric system ('x-y piezo').

During a scan, the SICM probe is mounted onto a vertical piezoelectric positioning system that allows precise movement of the nanopipette normal to the surface. The sample is mounted onto a two-axis piezoelectric stage that allows the substrate to move in the x-y plane while the tip remains stationary. One QRCE is inserted into the nanopipette while a second is placed in bulk solution. In the standard SICM setup, a bias is then applied between the two electrodes in order to drive an ionic current.

1.3.2 Feedback Types and Scanning Regimes: While the physical setup remains the same, there are several methods in which the SICM probe can be used to detect the surface of interest. The original, and most widely used feedback type is direct current (DC, Figure 1.3a). When DC feedback is used, the probe is approached

towards the surface and the ionic current is monitored for a percentage drop (typically 1-5%) from the value when the probe was in bulk. This decrease in current is attributed to the increased resistance in the system, as the gap resistance between the probe and substrate becomes comparable with that of the probe opening.

The second feedback type used for SICM mapping is distance modulation (DM, Figure 1.3b). In DM-SICM, an oscillation of the z-position is superimposed onto the overall movement of the probe. This oscillation is typically at several hundred Hz with an amplitude of 10-20% of the nanopipette diameter. As the probe approaches a surface, the oscillation will induce an alternating current (AC) component of the ionic current that can then be extracted at the same frequency as the physical oscillation using a lock-in amplifier. The quantity monitored is the amplitude of that AC signal, which should be zero in bulk and increase upon approach to the surface as the probe moves repeatedly from high to low current. A third feedback type, bias modulation (BM, Figure 1.3c), was recently introduced to SICM imaging.[58] In BM-SICM, the harmonic oscillation from the lock-in amplifier is superimposed on the bias between the two electrodes rather than the z-position of the probe. This oscillation induces a similar response in the ionic current; the AC phase of which is extracted and monitored at the same frequency as that applied. The AC phase is very sensitive to the probe-substrate separation and can thus be used as feedback for BM-SICM.

Each of the three feedback types has several advantages and disadvantages that make them suitable to different applications of SICM. DC-SICM typically allows for a faster approach rate than the oscillation feedback types, as there is no limitation from the time constant of the lock-in amplifier or potential damage to the z-piezo. However, the ionic current used for DC-SICM is prone to drifting during the course of a scan, making it very challenging to operate in a constant-distance scanning regime (*vide infra*). DM-SICM overcomes the problem of drift, as the feedback is reliant only on the change in ionic current during the period of the probe oscillation, rather than over the course of the entire scan. As BM-SICM considers only the phase of the AC signal relative to the applied bias, it does not require a net bias to be applied between the two electrodes. Minimizing the applied bias between the two electrodes has been shown to be highly beneficial for functional mapping with SICM, particularly when determining surface charge.[59,60]

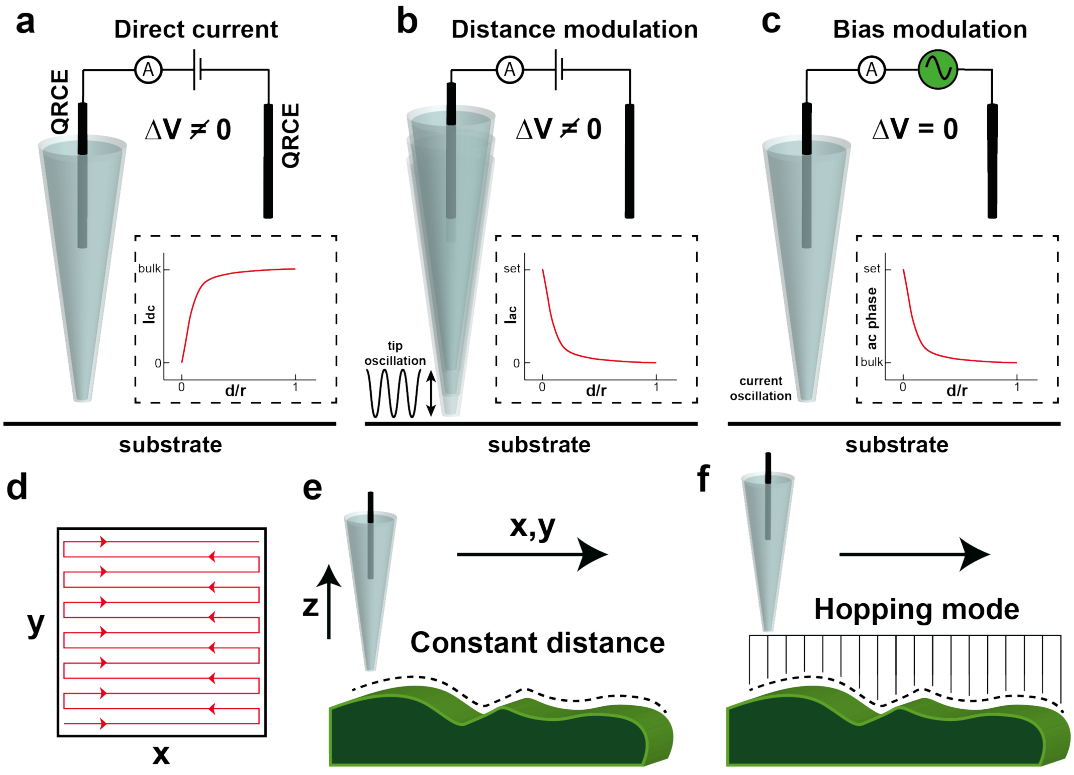

Figure 1.3. Feedback types and scanning regimes used in SICM. (a) DC-SICM, in which a decrease in ionic current is used to detect the surface. (b) DM-SICM, in which a physical oscillation is applied to the z-piezoelectric positioner, and the AC amplitude of the ionic current increases upon approach to the surface. (c) BM-SICM, in which a small harmonic oscillation is added to the voltage between the two QRCEs and the surface is detected via a change in the AC phase. (d) Raster scan pattern showing the typical path taken by the probe relative to the surface during an SICM experiment. (e) Constant-distance scanning mode, in which the probe-substrate separation is kept constant by adjustment of the z-position to maintain a given feedback threshold. (f) Hopping mode, in which the probe is approached to the surface at an array of discrete points. Adapted from Page et al.[17]

Once the appropriate feedback type has been chosen for an SICM experiment, it is necessary to consider how to scan the probe relative to the surface. The substrate is typically moved in a raster scan pattern (Figure 1.3d) under the nanopipette in one of two regimes. In constant-distance mode (Figure 1.3e), the z-positioner is continually adjusted during the scan in an attempt to maintain a constant separation between the probe and the surface, similar to constant-current STM. This

is achieved by maintaining a constant value of the feedback response, moving closer to the surface if the feedback needs to be increased, and away if it should be decreased. In 'hopping' or 'standing approach' mode (Figure 1.3f), the probe is translated towards the surface at each pixel of an image, before being retracted into the bulk solution. While the scan time for hopping mode experiments is significantly longer than constant-distance mode, it allows the probe to navigate large variances in topography without breaking the tip, something that can cause difficulties when using constant-distance mode. Hopping mode also allows functional measurements (for example uptake rate or surface charge, see Chapters 2 and 3 respectively) to be referenced to the bulk value at each pixel, which proves necessary when developing a meaningful quantitative method.

1.3.3 Applications of SICM: The non-invasive nature of SICM relative to other scanning probe techniques,[61] combined with the wide range of potential imaging media (any ionic species capable of carrying current), have made it a popular technique for live cell imaging.[56,57,62–72] The aim of such experiments is typically to map the topography of a cell or group of cells, either in their native state or under some kind of physical or chemical stress. The first images of live cells using SICM were collected in 1997,[73,74] and showed that while there was no damage to the cells as a result of the SICM probe, changes in surface topography could be detected by conducting several consecutive scans. The method of performing multiple scans of the same area of a sample has also been used to study changes in cellular volume and mobility of cardiac myocytes[56] and oligodendrocytes.[67] Later studies increased both the lateral and temporal resolution of the technique in order to study dynamic processes of subcellular features such as microvilli.[64,75] Examples of SICM topographical imaging of both biological and inert substrates are given in Figure 1.4.

While the topographical mapping of non-conducting, soft samples has remained the primary use of SICM, it has found several other applications in the 30 years since its inception. In the very first SICM study,[1] the nanopipette probe was used to detect pores in a membrane, with an increase in ionic current attributed to the increase in local conductance over a pore. This principle has been applied to both biological[76,77] and synthetic[78,79] nanopores, and the experimental and theoretical response of individual pores has been well studied.[80]

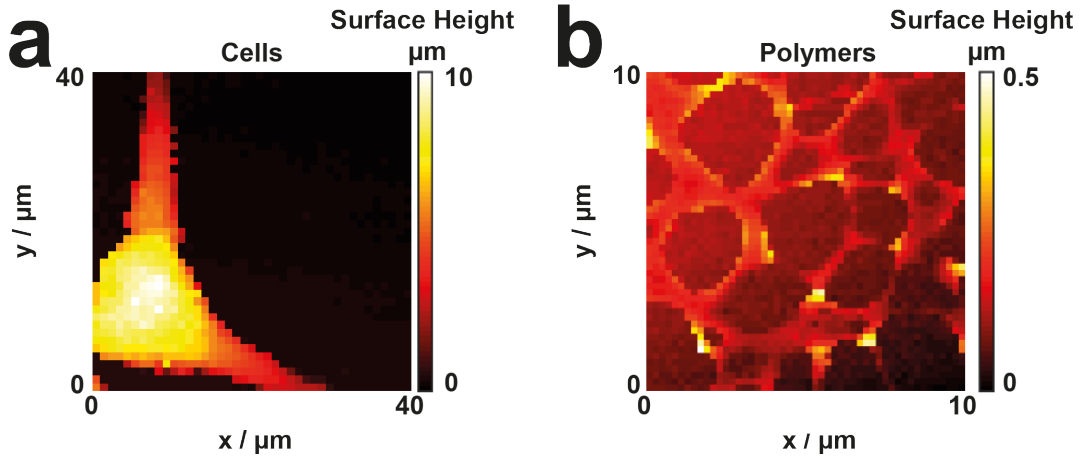

Figure 1.4. Topographical mapping using SICM. Both the PC12 cell (a) and the interrupted polystyrene film (b) are on a glass substrate. Adapted from Page et al.[17]

In addition to the applications of SICM to surface topography and nanopore conductance, it has also been used as a tool for local delivery to a surface. If the analyte of interest is charged in solution, the nanopipette can be used as a reservoir that will deliver on demand depending on the applied electric field. For example, if the analyte is positively charged in solution, a negative potential can be applied to the nanopipette QRCE relative to the bulk QRCE, holding the analyte in the probe. When the nanopipette is located over the desired region of the substrate, the polarity of the potential can be switched to release the analyte from the probe and deliver it to a highly specific location. This technique has been used to deliver negatively-charged DNA molecules from a nanopipette,[81,82] and deposit them in microscale aggregations on a streptavidin-coated glass surface.[83] It was subsequently used to deliver proteins to individual spermatozoa, demonstrating differences in localization to different subcellular compartments, whilst tracking the delivery using a fluorescence microscope.[84] Recent studies have demonstrated the delivery of capsaicin to neuronal cells[85] and isoproterenol to the T-tubules of cardiomyocytes.[86] In this thesis, the SICM nanopipette is used as a reservoir of an analyte to investigate cellular uptake (Chapter 2), a mediator that is locally delivered to a substrate electrode (Chapter 4), and Cu^{2+} ions that are deposited on a Au surface (Chapter 5).

While topographical/nanopore imaging and local delivery have been the most prevalent uses of SICM, the nanopipette probe it employs has also been utilised for

several other applications. The SICM nanopipette has been used for so-called 'nanobiopsies', in which the probe penetrates the cell membrane at a desired point before extracting a small quantity of intracellular material for further analysis.[87] It was demonstrated that RNA could be taken from the cell, amplified using the polymerase chain reaction, and then sequenced.[87] As the size of the nanopipette used is much smaller than the overall size of the cell, the technique is minimally invasive and the cell can remain viable after the nanobiopsy has been performed. Nanopipettes have also been used as electrospray ionization emitters, with a higher signal-to-noise ratio than typical nanospray emitters.[88] This technique was then developed into an SPM technique known as scanning electrospray microscopy, that was used to map topography at the nanoscale.[89] Careful control of the voltage regime used in SICM has allowed it to be used as a tool for surface charge mapping[59,60] (see Section 1.4 and Chapters 3 and 4), and for mapping electrochemical reactions at both electrode and nanoparticle (NP) substrates.[90,91]

1.3.4 Understanding the Ionic Current Response: In order to use SICM as a functional tool for the investigation of interfacial process, it is essential to fully understand the factors contributing to the experimental observations. These factors are several, and include the geometry of the nanopipette, the composition of the electrolyte solution, and the charge on both the tip and the surface.[60,92,93] While it is possible to approach a surface and build up a topographical map without a comprehensive consideration of each of these elements, it becomes necessary when attempting to extract functional information using SICM.

1.3.4.1 Probe Fabrication and Geometry: The nanopipette used in SICM is made from a glass or quartz capillary, typically with an inner diameter of 0.5-1 mm. The capillary is carefully placed into a laser puller, in which the centre of the capillary is heated to the point of melting whilst a pulling force is applied to either side. As the two halves of the capillary are pulled apart, they narrow to a fine point, eventually separating to create two nanopipettes of similar geometry. The size of the opening at the end of the nanopipette depends both on the material used and the parameters of the laser puller, such as the strength of the pulling force and the power of the laser itself. Tuning of these parameters allows the user to consistently produce

nanopipettes with the desired aperture, from several microns to several nanometers in diameter.

During an SICM experiment, the lateral resolution of the scan is directly linked to the size of the opening at the end of the nanopipette used, and is typically assumed to be around three times the radius of the opening.[93–95] Thus, a probe with a 200 nm diameter aperture would be able to resolve individual surface features of 150 nm in width. With some studies having demonstrated probes with an estimated aperture radius of 5-10 nm,[62,96] this gives SICM a limiting resolution of below 20 nm. While this is significantly higher resolution than can typically be achieved with SECM, it is still far from the sub-nm resolution routinely achieved with both STM and AFM. However, SICM has several advantages over both of these techniques in that the probes are inexpensive and easily fabricated, it can be used on living samples, and can operate at STP. As a result of these advantages, SICM has been viewed favourably for soft sample imaging when compared with AFM.[61]

As the SICM response is highly dependent on the pipette geometry, it is necessary to characterise the probes produced by a given set of laser puller parameters. There are several techniques that are used for pipette characterization, the most common of which is to consider the ionic current response at differing potential differences in a cyclic voltammogram (CV) regime. The pipette is then assumed to have a conical shape when calculating the aperture radius from the current magnitude. A more reliable technique for the study of nanopipette geometry is scanning electron microscopy (SEM, Figure 1.5a),[62,66,89,97] which can provide structural information about the size of the opening as well as the outer dimensions of the probe along its length. However, it has been recently demonstrated that the external geometry alone is not sufficient to fully predict the ionic current response,[92] and that the assumption of a conical internal geometry is incorrect. Thus, transmission electron microscopy (TEM, Figure 1.5b) has become a vital technique in the full characterization of the SICM probe. TEM provides significantly more information that SEM as it allows the inner lumen of the nanopipette to be visualised. This allows many geometrical parameters such as the glass thickness, diameter and inner cone angle to be extracted along the length of the pipette. The inner cone angle in particular has been shown to vary significantly along the length of the pipette,[92] while it is fixed in the assumption of a conical geometry.

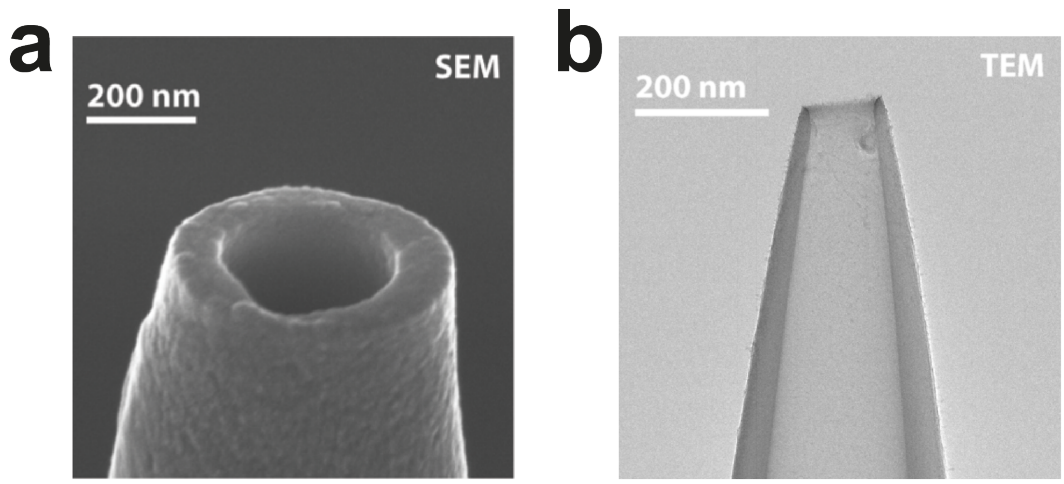

Figure 1.5. Electron micrographs of single-channel glass nanopipettes. SICM probes can be characterised by either SEM (a) or TEM (b).

1.3.4.2 Ion Current Rectification: In the absence of a nanopipette, the ionic current passed between Ag/AgCl QRCEs in an electrolytic solution follows a linear, Ohmic relationship with voltage. However, when one QRCE is in the bath and one in a nanopipette, both the geometry and the surface chemistry of that nanopipette can affect the magnitude of the current passed. More specifically, the silanol groups on the surface of the glass or quartz are dissociated at the typical pH values used in SICM, and they thus present a negative surface charge,[98] which in turn gives rise to an increase in concentration of cations near the surface. The fundamental properties of charged surfaces are discussed further in Section 1.4, as well as in Chapters 3 and 4 of this thesis. The negative charge, combined with the pseudo-conical geometry of the probe, gives rise to a phenomenon known as ion current rectification (ICR),[99–106] in which there is a nonlinear relationship between the applied bias and the observed ionic current. The degree to which the current is rectified, termed the rectification ratio, is dependent on many factors, one of the most significant being the nanopipette surface charge.[92,100,101] Figure 1.6 shows simulated current-voltage curves of a 90 nm-radius nanopipette with different surface charges applied to the nanopipette wall. The effect of ICR is stronger at higher surface charges, and is reversed in polarity when the polarity of the charge on the nanopipette is reversed. This is due to the preferential transport of either anions or cations at a given surface charge polarity. In addition to the geometry of the nanopipette and the charge on the glass or quartz,

ICR also depends on the concentration of electrolyte.[99] It is more prevalent at lower ionic strengths as the layer of solvated ions countering the charge at the surface extends further into the centre of the nanopipette (see Section 1.4).

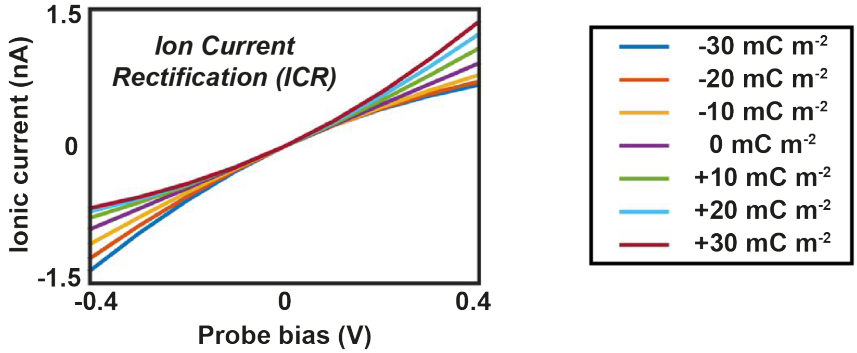

Figure 1.6. Dependence of ion current rectification on surface charge. When the nanopipette is negatively charged, the current is enhanced at negative probe bias and diminished at positive probe bias. When the charge is positive, the effect is reversed.

As the primary observable quantity in an SICM experiment is the ionic current, an understanding of the prevalence of ICR in a given experimental setup is essential if any attempt at quantification of functional information is to be attempted. Thus, both the relationship between nanopipette charge and ICR, as well as the separation of pipette-induced and surface-induced rectification have been thoroughly investigated.[3,60,92]

1.3.4.3 Finite Element Method Modelling: The complex range of variables that contribute to the ionic current make the interpretation of the SICM response a challenging process. In order to provide clarity, a theoretical treatment of the SICM setup is often performed in tandem with the experiments.[60,92] As the partial differential equations that treat both the transport of species in solution and the electric field distribution cannot be solved analytically (see Chapters 2 and 4), they are typically treated numerically to provide approximate solutions with arbitrary accuracy. One such numerical method is finite element method (FEM) modelling, in which a one, two, or three-dimensional domain is divided into a finite number of regions using a technique known as 'meshing', using software such as COMSOL

Multiphysics (used herein). The necessary equations are then solved numerically at the intersection of the different regions (known as 'mesh points') to the desired degree of error with an iterative solving method.

Designing a FEM model for SICM first requires the reproduction of the experimental geometry. If both the probe used and the solution domain are symmetric about their central axis, then SICM can be modelled with a 2D, axisymmetric geometry, as in Chapters 3 and 4 of this thesis. If the probe is not symmetric about its central axis, as is often the case with multi-channelled nanopipettes (see Section 1.3.5), then the experimental setup can be reproduced with a 3D geometry, as in Chapter 2 of this thesis. It should be noted that 3D simulations are typically significantly more computationally expensive than 2D simulations, and thus it is preferable to build models in 2D wherever possible. After the geometry has been built and the required differential equations included, boundary and initial conditions are applied. In a SICM simulation, boundary conditions typically refer to either a concentration or a flux at the interface between two domains, but also include applied potentials and surface charges. For example, the wall of a nanopipette would be designated as a 'zero flux' boundary as no solution should be permitted to pass through. The initial conditions are either an initial estimate in the case of a steady-state simulation, or the starting conditions for a time-dependent simulation. Time-dependent simulations are typically employed when the system is perturbed in some way, such as a change in the applied voltage. In order to provide accurate initial conditions for a time-dependent simulation, it is common to take the results of a steady-state simulation calculated before the perturbation is applied.

In this thesis, FEM simulations are used to provide a more complete understanding of the SICM response measured experimentally. In Chapter 2, FEM simulations are used both to determine the probe-substrate separation in SICM, and to correlate the observed changed in SECM current with the uptake rate constant at the surface. In Chapter 3, FEM simulations are used to extract quantitative values of the surface charge on both inert and cellular surfaces, by studying the relationship of the ionic current near a charged interface with the magnitude of that charge. Finally, in Chapter 4, FEM simulations are used to study the change in electric field strength around the nanopipette tip when the concentration of electrolyte in the probe and the bath are varied.

1.3.5 Multi-channel Probes: In addition to the single-channel applications described in Section 1.3.3, SICM can be integrated into a multi-channel probe, often adding greater functionality than can otherwise be achieved with a single barrel. The simplest multi-channel probe is the 'theta' pipette, containing two equally-sized open channels, each of which is filled with electrolytic solution and a QRCE (Figure 1.7a). This setup has been used for several applications, the earliest of which was the deposition of two different types of DNA from each of the two channels.[107] One barrel contained DNA labelled with the fluorescent red molecule alexa 647 while the other was labelled with rhodamine green. Controlling the bias between the two barrels allowed the selective deposition of the DNA at each pixel, and thus the printing of two-component images on a functionalised surface. This work is developed in Chapter 5 of this thesis, in which both the bias between the two barrels and the substrate bias are carefully tuned to optimise the deposition of Cu microstructures.

A theta pipette is also used in potentiometric SICM (P-SICM),[108–112] which allows the deconvolution, and thus simultaneous measurement, of both topography and conductance across a membrane. In P-SICM, electrodes are placed either side of a membrane in order to induce ion flux across it. One channel of the theta pipette is then used to track the topography of the substrate, while the other measures the potential across the membrane, which varies as a function of conductance. This setup has been applied to both model nanopores[108] and biological tight junctions.[110,111]

The final application of dual open-channel probes is in a technique known as scanning electrochemical cell microscopy (SECCM). In SECCM, there is no bath solution, with the probe forming a droplet contact upon approach to the surface, the morphology of which depends on the tip-substrate separation and the hydrophobicity of the substrate.[18,19] This confined electrochemical cell significantly reduces background noise relative to a typical SICM experiment, thus increasing the current sensitivity. SECCM has been used for the study of substrate reactivity,[20,113–115] localised dissolution,[21,116] and precise deposition of polymers onto a surface.[117,118]

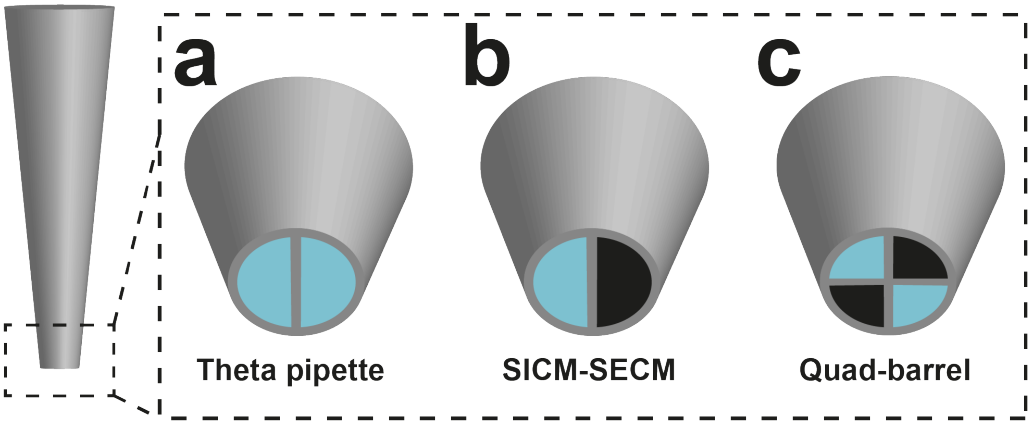

Figure 1.7. Multi-channelled nanopipette configurations. When both channels are filled with electrolyte (a), the probe can be used either in bulk solution or in a scanning droplet setup. (b) SICM-SECM, in which one barrel is open to solution while the other is a solid electrode. SICM-SECM can be extended to a quad-barrel setup (c), with two open channels and two solid electrodes.

The functionality of the theta pipette can be changed by the modification of one or both of the barrels. One way in which this has been done is to cover one barrel with a membrane patch containing a single ligand-gated ion channel, which can then be stimulated by varying the concentration of ligand molecules in the bulk solution.[119] However, the most common modification of a theta pipette is the deposition of carbon on the inside of one or both barrels, either via pyrolysis[120,121] or chemical vapour deposition (CVD).[122–124] While CVD produces probes with a more consistent geometry, it is both significantly more expensive than deposition via pyrolysis, and takes many times longer to fabricate a probe. One prominent application of carbon-filled probes is in SICM-SECM[38–41,120,125–127] (Figure 1.7b), in which one barrel is filled with carbon (SECM) and the other is left open to the bulk solution (SICM). The carbon is back-contacted with a Cu wire, allowing the potential at the end of the probe to be varied during a scanning experiment.[125,127] SICM-SECM has been used for amperometric measurements of electrocatalytic activity[125,127] and for potentiometric measurements of pH;[120] functionality that is added to in Chapter 2 of this thesis. The sensitivity of SICM-SECM has been improved by depositing electrocatalytically-active Pt at the end of the carbon nanoelectrode, though controlling the extent of the deposition has proved

challenging.[128] The two-barrel approach used in both SECCM and SICM-SECM has been extended into a four-barrel 'quad-probe' (Figure 1.7c), with two open channels that create a droplet on the surface, and two individually-addressable carbon nanoelectrodes.[129] This setup has been used to investigate the electrochemical activity of individual carbon nanotubes,[129] and to detect single molecules with femtoamp precision.[130] Chapter 2 of this thesis is concerned with the use of a multifunctional probe in a SICM-SECM configuration for the detection of molecular uptake on a subcellular scale.

1.4 Surface Charge

Surface charge is a phenomenon in which a surface has either a net positive or a net negative density of charged species such as electrons or ions. It is often considered in the study of colloids, in which the presence of an external charge on colloidal particles can increase repulsion between particles and thus improve the stability of the suspension as a whole.[131] However, it can also be manifest on extended surfaces such as glass or quartz,[98,101] or in living systems such as proteins and biological membranes.[132,133] The presence of charge on a surface can arise from several different physical phenomena; the adsorption of charged ions onto a surface, protonation or deprotonation of surface groups, and, in the case of a conducting surface, the application of an external voltage. The magnitude of charge on a surface is normalised to the area of the substrate to give a quantity known as the surface charge density, measured in units of C m^{-2}. These units make it possible to imagine surface charge as the number of elementary charges, e, per unit area. While this may be the case for fixed surface groups of which some fraction may be protonated/deprotonated in a given set of conditions (for example, variable pH), this approximation is less appropriate for non-fixed charges, such as those within a metal under an applied potential. In addition to the importance of surface charge in colloid chemistry, it can also play a crucial role in nanoscale devices such as solid-state nanopores,[104,134] as well as in crystalline systems.[135–139]

Surface charge is also important in many aspects of cellular function. Oligodendrocytes of the central nervous system were shown to down-regulate the production of negatively charged oligosaccharides of the glycocalyx when wrapping around neuronal axons. This reduction in negative charge was shown to be beneficial

to multi-cellular stacking, with weak, long distance attractive forces being allowed to dominate.[140] The adhesion of both *E. coli* and other bacteria have also been shown to have a strong dependence on charge interactions.[141,132] The variation of surface charge density and polarity is a common feature of studies that consider the uptake of NPs into living cells, with different surface functionalities providing different uptake rates and levels of cytotoxicity.[142–145] Charged polymers have been used to direct and control cellular growth and morphology,[146] and charged groups within the membrane of budding yeast cells have been used to guide division via the application of an external electric field.[147] In addition to cellular adhesion, uptake, and growth, surface charge has been shown to play a role in intercellular communication, notably in the cases of cancer cell exosome internalization[148] and T-cell activation.[133] Chapter 3 of this thesis explores the charge density across the surface of neuron-like PC12 cells using SICM.

1.4.1 Double Layer Theory: The presence of a charged interface under electrolyte solution causes a perturbation of the solution composition near the charged surface.[149] For example, a surface that presents a positive charge in a given set of conditions would induce a higher concentration of anions near the surface, and a depletion of cations (Figure 1.8a,b). The region near the surface in which the composition of the electrolyte is altered from bulk solution is termed the diffuse, or electrical double layer (EDL). The composition and size of the EDL are highly sensitive to the nature of the surface (e.g. conducting or insulating), the magnitude of the charge on the surface, and the concentration of electrolyte in the bath solution.[150] Much of the foundational work in the study of charged interfaces was motivated by the relationship between applied potential and surface charge at electrode surfaces.[151–153] While the applications in this thesis typically consider the charge presented at either insulators such as glass, or in more complex systems such as living cells, the basic principles described herein are transferable between the different experimental setups.

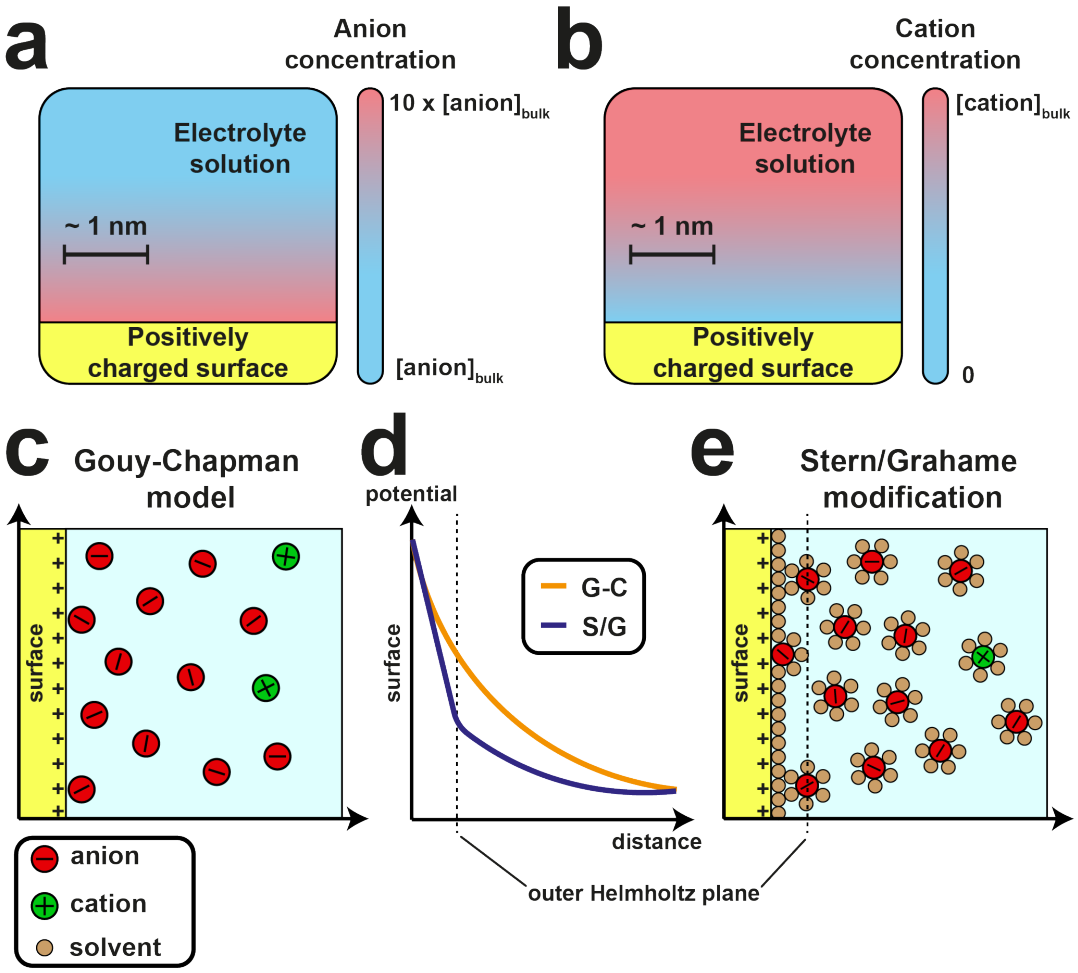

Figure 1.8. Structure of the electrical double layer (EDL). The general situation at the interface of a charged surface and an electroneutral solution is the perturbation of ionic concentrations from bulk concentration near the surface (a,b). For a positively-charged surface, there is an increase in anion concentration (a) and a decrease in cation concentration (b) adjacent to the surface. The Gouy-Chapman (GC) model of the EDL (c) does not consider the finite size of ions and is thus unsuitable at high electrolyte concentrations. Modifications of the GC model by Stern and Grahame account for phenomena such as specifically-adsorbed ions and a solvent layer at the surface (e). Plots of the electric potential that arise from the charge at the surface (d) differ between models depending on the treatment of the ions closest to the interface.

The first person to realise that the introduction of a charged surface into an electrolytic solution would cause a rearrangement of ions near that surface was Helmholtz, and he demonstrated the first notion of the EDL as a nanoscale dielectric. His initial model assumed a constant differential capacitance, meaning that the

charge stored by the EDL was linearly dependent on the applied potential, a notion disproved independently by Gouy and Chapman in the early 20th Century. The Gouy-Chapman (GC) model of the EDL introduced the idea of a diffuse layer of ions close to the interface in order to balance out the charge on the surface (Figure 1.8c). This diffuse region of counterions is at its highest concentration directly adjacent to the surface, while the concentration is lower at greater separation due to the reduction in strength of electrostatic forces. This leads to an exponential drop in the electric potential away from the surface (orange line, Figure 1.8d), the profile of which is dependent on many factors including the magnitude of the surface potential and the concentration of electrolyte species. For example, if the concentration of electrolyte is very low, the characteristic length of the EDL will be relatively long as the volume required to provide the counterions needed to balance a charge at the surface is larger than in a high concentration solution. In the GC model, the relationship between the surface charge density (σ_s) and the surface potential (ϕ_0) is given by the following:[154]

$$\sigma_s = (8RT\varepsilon\varepsilon_0 c\times 10^3)^{1/2} \sinh\left(\frac{z\phi_0 F}{2RT}\right) \qquad (1.1)$$

where R is the molar gas constant, T the temperature, ε the dielectric constant of the solvent (78.54 for water at 298 K), ε_0 the permittivity of free space, c the molar concentration of electrolyte, z the charge magnitude of the z:z electrolyte used, and F the Faraday constant. This model of the EDL is best applied in systems with low ionic strength and at low potentials.[149] At low ionic strength, the use of the dielectric constant of water is a reasonable approximation (for an aqueous solution), but this becomes far less accurate as the concentration is increased. At low surface potentials, the model predicts reasonable electrolyte concentrations near the interface, but the omission of the finite size of the ions in solution means that it can be unrealistic at high surface potentials, when the number of ions required to balance the charge at the surface is large. Despite these limitations, the GC model can be used to extract the Debye parameter (κ), the inverse of which is described as the characteristic length, or thickness, of the EDL via the following equation:[154]

$$\kappa = \left(\frac{2F^2 I \times 10^3}{RT\varepsilon\varepsilon_0}\right)^{1/2} \quad (1.2)$$

where I is the ionic strength of the electrolyte solution. As described above, κ is proportional to the square root of the ionic strength, and thus the thickness of the EDL will decrease as the ionic strength increases. Table 1 shows some values of double layer thickness, κ^{-1}, for several different 1:1 electrolyte concentrations at 298 K.

Table 1.1. Relationship between electrolyte concentration and double layer thickness for a 1:1 electrolyte at 298 K.[150]

c (mM)	κ^{-1} (nm)
0.1	30.4
1	9.62
10	3.04
100	0.96
1000	0.3

To accommodate for the breakdown of the GC model at high electrolyte concentrations and surface charges, Stern proposed a modification that incorporated many of the ideas of Helmholtz. He realised that ions have a finite size, that an ion could not approach closer than an ionic radius, and that they could thus not be treated as point charges. He proposed a compact layer directly adjacent to the electrode, now known as the Stern layer, comprised of solvated ions at the point of closest approach (Figure 1.8e). The plane passing through the middle of those solvated ions is termed the outer Helmholtz plane (OHP). As the thickness of the Stern layer is pre-determined by the electrolyte and solvent used, the exponential decay in electric potential seen in the GC model does not occur, and the drop in potential from the surface to the OHP is instead linear (blue line, Figure 1.8d). The diffuse portion of the EDL outside of the Stern layer is still treated with the GC model, and the electric potential at the OHP is significantly lower than at the surface. Grahame suggested the inclusion of a second plane (now known as the inner Helmholtz plane, IHP) to accommodate ions that had been specifically adsorbed to

the surface, as they would be able to approach closer than those that were fully solvated (Figure 1.8e). As the studies herein typically use low concentrations of electrolyte (≤ 0.1 M), and low surface charge magnitudes (≤ 100 mC m^{-2}), it was decided that the GC model was sufficiently accurate when constructing FEM simulations of the experimental systems. Full details of surface charge simulations are given in Chapters 3 and 4.

1.4.2 Techniques to Measure Surface Charge: The importance of surface charge to a diverse array of interfacial systems, detailed at the beginning of section 1.5, has led to the development of an equally diverse set of techniques used to measure that charge. No single technique is applicable to every system, with some being more suitable for the study of particulate (colloidal) systems, while others are best used on extended substrates. This section aims to summarise the techniques that have historically been used to measure surface charge, and motivate the opportunities for SICM as an alternative method for spatially resolved charge mapping on extended substrates. Studies of surface charge via electrocapillary phenomena at a dropping mercury electrode were essential to many of the foundational studies of surface charge, but are not included here as they have been reviewed extensively and are far removed from the applications for which SICM is used in this thesis.[150,153]

1.4.2.1 Zeta-potential Measurements: One of the most common ways to investigate surface charge in colloidal systems is to measure it indirectly using a concept known as the zeta (ζ) potential.[155,156] For a NP in solution, the ζ-potential is defined as the difference in electric potential between the 'slipping plane' of the NP and the bulk solution (Figure 1.9). When in solution, a charged NP will form an EDL of counterions, as described in section 1.4.1. The EDL can be separated into the compact Stern later, comprised of ions that are either adsorbed on the surface or at the point of closest approach, and the diffuse layer. When considering charged particles under an external electric field, the diffuse layer around a NP can be further subdivided into those ions that are sufficiently close to the NP that they keep their position as the NP moves through solution, and those that are distant from the NP such that the electrostatic forces are too weak to hold them next to the particle (Figure 1.9a). The boundary between these two regions is known as the slipping

plane, and it is at this point that the definition of the ζ-potential is taken (Figure 1.9b). When the surface of the NP is charged, that charge can be related to the surface potential, ϕ_0, by a relation such as that in equation 1.1. The presence of both the Stern layer and the diffuse layer lead to a decrease in the electric potential further from the surface of the NP, and as these layers are 'attached' to the NP it is not possible to measure the surface potential directly.

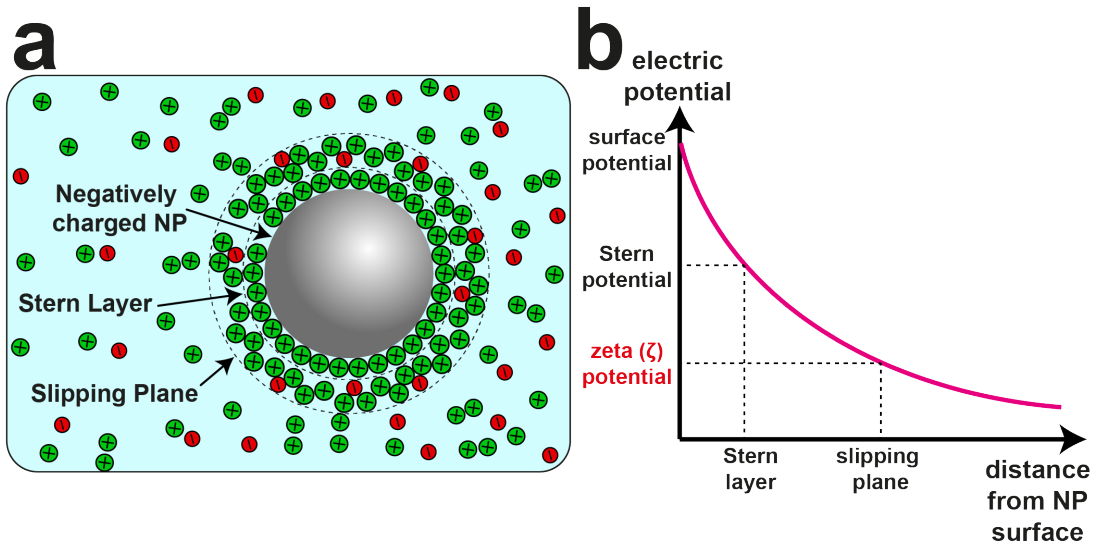

Figure 1.9. Defining the ζ-potential at a charged NP. (a) Schematic of a negatively charged NP, surrounded by a compact Stern layer of cations and a diffuse layer held within the slipping plane. (b) The ζ-potential of the NP is taken at the slipping plane, and is of a lower magnitude than the Stern and surface potentials.

As the ζ-potential cannot be directly measured, it has to be deduced by subjecting particles to an external electric field and tracking their movement in solution, known as their electrophoretic mobility. The theory that relates ζ-potential to electrophoretic mobility was developed by Smoluchowski in the early 20th Century and makes several assumptions such as the EDL thickness being significantly smaller that the particle radius. If this is not the case (as in very low electrolyte concentrations), then an alternative theory is used. ζ-potentials are measured in millivolts, and particles with a higher magnitude ζ-potential are more stable and less prone to aggregation.[157,158] The measurement of the ζ-potential of colloidal particles is now a routine part of their characterisation.

1.4.2.2 Electrostatic Force Microscopy: Electrostatic force microscopy (EFM) is one of several techniques that are capable of creating spatially resolved images of the charge on a surface.[159] In EFM, a cantilever analogous to that used in AFM is oscillated at some separation (at least tens of nanometres) from the surface. A potential difference of known magnitude is applied between the cantilever and the surface, and the work functions of both the probe and the substrate must be known to make an accurate measurement. As the probe is scanned over the surface, long-range electrostatic forces can affect both the resonant frequency and amplitude of the cantilever oscillation, and it is these variables that are the measurable quantities in an EFM. In order to probe electrostatic forces at a large separation from the surface, an EFM typically operates under vacuum or in a non-conductive solution. If the substrate and cantilever were under electrolyte solution, the formation of EDLs would hinder the required potential difference between the probe and surface. Despite this drawback, EFM has been used to investigate many systems, including graphene surfaces in a water environment,[160] the reduction of graphene oxide,[161] single triglycine sulfate crystals,[162] and proteins via both imaging[163] and approach curves.[164]

The interpretation of electrostatic forces in force microscopy remains a challenge,[165] particularly when imaging under electrolytic conditions.[166,167] In order to measure electrostatic forces, the probe itself must be charged. While this charge may be known at the beginning of an experiment, it is liable to change throughout the course of a scan, making the extraction of reliable charge data extremely challenging. Despite these difficulties, there have been multiple studies using AFM in a non-conventional mode to measure charge density on an extended substrate.[168–172] Despite the success of some of these new imaging modes, force microscopy remains unable to probe the surface charge density on living cells, as they require a high concentration of electrolyte to maintain realistic physiological conditions. Under this setup, the EDL is compressed to less than 10 angstroms and thus probing it directly with force microscopy would likely lead to the damage of the cell. It is in these biological systems that SICM has been shown to be able to resolve surface charge whilst maintaining the viability of the substrate cell.[173]

1.4.2.3 Additional Methods: A further scanning probe technique that has been used to investigate surface charge is Kelvin probe force microscopy (KPFM).[174–177] KPFM uses a conducting tip with an applied AC voltage to form a capacitor between the probe and the surface. When a direct current flows between the tip and the surface, the cantilever vibrates, and the magnitude of that oscillation is then translated into the local potential difference between the tip and the surface, and thus the surface potential. KPFM has largely been applied to either conducting or semiconducting materials,[177] with a handful of studies investigating biological substrates.[178,179] While KPFM has been used to successfully map surface potential on the nanoscale, it requires significant knowledge about the physical properties of the probe in order to correctly infer information about the surface,[177] and has thus not been as widely used as it may otherwise have been.

Surface plasmon resonance (SPR) is a technique in which a surface is irradiated in order to study the interaction of electrons at the interface.[180] As SPR is highly sensitive to the environment directly adjacent to the irradiated surface, it is possible to study interactions on the same length scale as the EDL. It has traditionally been used the study the adsorption of molecules onto a surface, but has also found application in the measurement of surface charge.[181] In the first study to use SPR for the investigation of surface charge, the charge on silica NPs was shown to influence the point of closest approach to a surface coated with a charged layer of the same parity.[181] Combining the experimental observations with a theoretical consideration of the system, it was possible to simultaneously study both the topography and charge of individual particles using SPR.[181] Further to that initial study, SPR has been used to detect small molecules in a surface charge based regime,[182] and to track the charge-dependent swelling of nanocrystalline films.[183] However, SPR still suffers from a topography-charge convolution that is common to many of the above techniques, which often means that one of the two factors needs to be either known or assumed before the experiment can begin. The deconvolution of charge and topography has been an important aspect of surface charge mapping with SICM,[60] and is discussed in more detail in Chapter 3.

1.4.3 Opportunities for SICM as a Charge Mapping Tool: The ability to use SICM as a tool for surface charge mapping is reliant on the phenomenon of ICR

outlined in section 1.3.4.2. Rectification of the ionic current through a nanopipette is determined by the effect of the charge on the nanopipette on the transport of ions through the pipette orifice.[100,101] While this effect may be negligible for large-radius nanopipettes (more than a few hundred nanometres), it becomes increasingly prominent as the size of the nanopipette is reduced. This dependence of the ionic current on the presence of a charged surface (usually just the glass or quartz of the nanopipette itself), is what allows SICM to probe the charge of extended substrates. If the nanopipette is brought close enough to a charged interface, the transport of ions into and out of the probe will be determined not only by the charge on the nanopipette, but also by the charge on the substrate, as the two EDLs will govern the flux of ions through the nanopipette orifice. The smaller the probe-substrate separation, the larger the contribution of the substrate charge. This phenomenon is called surface-induced rectification (SIR),[60,184–186] and is depicted in Figure 1.10.

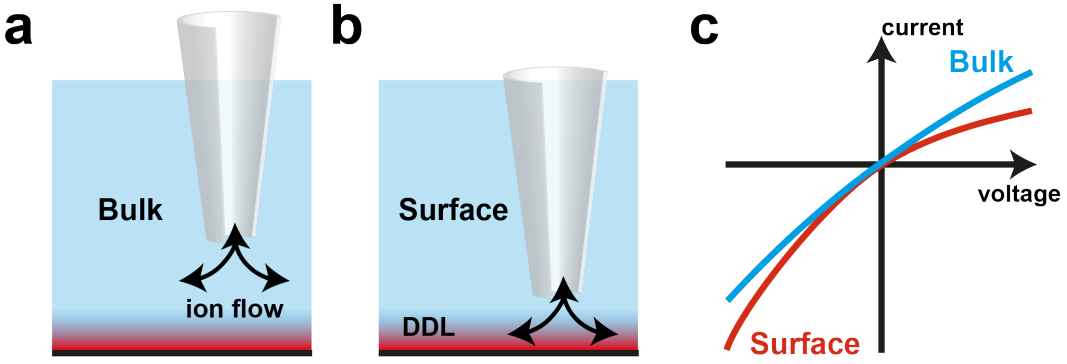

Figure 1.10. Surface induced rectification of nanopipette current. When in bulk solution (a), the nanopipette current is affected only by ICR (blue line in c). When close to a surface (b), the charge of that surface can change the profile of the rectification (red line in c).

The relationship between charge and SIR was first demonstrated via approach curves to surfaces of positive, neutral and negative charge.[59,185] It is widely assumed that the ionic current will always decrease when the nanopipette approaches a surface, but this was shown to be untrue for some combinations of applied probe bias and substrate surface charge, in which the current actually increased at low

probe-substrate separations. This discovery throws into jeopardy the accuracy of the topographical information for which SICM is most regularly used. It is typical in an SICM experiment to set a feedback threshold (e.g. 1% drop from the bulk current) that is then used for every approach in a scan-hopping regime. However, heterogeneities in the substrate surface charge could mean that a 1% reduction from the bulk current could occur at a probe-substrate separation of 10 nm or 100 nm and it would not be possible to tell which. This variability in the point of closest approach as a function of substrate surface charge reduces the reliability of the topographical information collected.

As SIR has been shown to be more prominent when a larger driving potential is applied between the two QRCEs,[59,60] efforts have been made to devise potential-control regimes that will allow the extraction of accurate topography and surface charge data. Some of the initial work used a physical oscillation of the nanopipette for topographical feedback (i.e. DM-SICM), though this still requires the application of a bias between the two electrodes and is thus not entirely reliable.[59] The development of BM-SICM allows the application of zero net bias by oscillating the potential in a harmonic profile about 0 V.[58] This feedback type was then used for the approach during a scan-hopping surface charge map, allowing the extraction of reliable topographical data.[60] The potential between the two electrodes was then swept in a CV to extract surface charge data at non-zero net potential difference.[60] The ability to use a single-channel nanopipette for multifunctional imaging significantly increases the power of SICM, and has potential applications in many fields from biology to crystallography and beyond. Chapter 3 of this thesis improves upon the scanning regime described above, while Chapter 4 considers the effect of a different feedback type on the ability of SICM to extract interfacial charge information.

1.5 Cellular Uptake

All living cells are surrounded by a cellular membrane; a lipid bilayer containing a variety of other molecules such as carbohydrates, cholesterol, and membrane-bound proteins. The cell membrane, and the proteins therein, govern the transport of molecules into and out of the cell, with some small molecules such as water able to diffuse across the membrane easily, while charged ions such as K^+ and Na^+ have to

be transported via proteins known as ion channels. Molecules that cross the cell membrane play a role in almost every function of the cell, from the O_2 used for cellular respiration to signalling proteins that facilitate intercellular communication. Despite the importance of cellular uptake in areas of research such as drug design, few techniques allow the quantitative measurement of uptake rates, with research focusing on either fluorescence assays[187,188] or 'post-mortem' techniques such as mass spectrometry.[189,190] This section aims to motivate Chapter 2 of this thesis, by discussing the potential of SEPMs as a tool to map cellular uptake rates.

1.5.1 Opportunities for Scanning Electrochemical Probe Microscopy: While the above techniques have successfully been used to study cellular uptake on a supercellular scale, very few are capable of the investigation of single cells or measurements on an even smaller scale. With microscale and nanoscale probes that can be scanned over a surface, SPMs offer an alternative route to the study of cellular uptake. However, as the probe will always be located in the extracellular domain, it is necessary to measure properties other than substrate topography in order to truly study the uptake process at the cell surface. While techniques such as STM and AFM are capable of resolving topography at an atomic level, they typically require a conducting or semiconducting substrate to map some other functionality, and are not optimised for use in a cellular environment. On the other hand, many SEPMs such as SECM and SICM are regularly used to image cellular samples,[32,73,56] and are thus more suited to the study of molecular uptake at the cell surface.

Several early studies used SECM to investigate the respiration of single cells, by studying the oxygen reduction reaction (ORR) at a Pt UME.[55,191,192] As the probe passes over the cell, the ORR current decreases as the cell is consuming O_2 and thus the local concentration is lower. Cells were then stressed with KCN,[191] ethyl alcohol or Antimycin A, and the decrease in ORR current corresponded to the reduction in respiratory activity as measured by fluorescence microscopy.[55] SECM has been used to simultaneously study the uptake and efflux of menadione and its glutathione complex into and out of yeast cells,[193] combining experimental results with numerical simulations to suggest that the uptake of menadione was the rate-limiting step in its conjugation. Other studies have used an ion-selective electrode as an

SECM probe to study Ag^+ uptake,[194] and monitored membrane permeability with a UME following exposure to metals such as Cr^{35} and Cd.[195–197]

While the resolution of SECM uptake studies is significantly higher than the majority of techniques used to study uptake, difficulties in the reproducible manufacturing of nanoscale SECM probes prevent highly resolved mapping over a cellular surface. Furthermore, despite the use of multiple mediators and complex potential-control functions,[198–200] there is a significant convolution between topographical and functional effects on the SECM response that make the interpretation of data relating to cellular uptake very challenging. In Chapter 2 of this thesis, both of these problems are addressed by the construction of nanoscale dual-channel SICM-SECM probes in which one channel monitors the cellular topography while the other measures the rate of uptake. In this regime, the rate of uptake between different subcellular regions can be differentiated.

1.6 References

(1) Hansma, P. K.; Drake, B.; Marti, O.; Gould, S. A.; Prater, C. B. *Science*. **1989**, *243*, 641–643.

(2) Page, A.; Kang, M.; Armitstead, A.; Perry, D.; Unwin, P. R. *Anal. Chem.* **2017**, *89* (5), 3021–3028.

(3) Page, A.; Perry, D.; Young, P.; Mitchell, D. A.; Frenguelli, B. G.; Unwin, P. R. *Anal. Chem.* **2016**, *88* (22), 10854–10859.

(4) Momotenko, D.; Page, A.; Adobes-Vidal, M.; Unwin, P. R. *ACS Nano* **2016**, *10* (9), 8871–8878.

(5) Meyer, E.; Hug, H. J.; Bennewitz, R. *Scanning probe microscopy: the lab on a tip*; Springer Berlin Heidelberg, 2013.

(6) Binnig, G.; Rohrer, H. *Surf. Sci.* **1983**, *126* (1–3), 236–244.

(7) Hansma, P. K.; Tersoff, J. *J. Appl. Phys.* **1987**, *61* (2), R1–R23.

(8) Binnig, G.; Quate, C. F. *Phys. Rev. Lett.* **1986**, *56* (9), 930–933.

(9) Rugar, D.; Hansma, P. *Phys. Today* **1990**, *43* (10), 23–30.

(10) Butt, H.-J.; Cappella, B.; Kappl, M. *Surf. Sci. Rep.* **2005**, *59* (1–6), 1–152.

(11) Willott, J. D.; Murdoch, T. J.; Webber, G. B.; Wanless, E. J. *Macromolecules* **2016**, *49* (6), 2327–2338.

(12) Froning, J. P.; Lazar, P.; Pykal, M.; Li, Q.; Dong, M.; Zbořil, R.; Otyepka, M.

Nanoscale **2017**, *9* (1), 119–127.

(13) Ido, S.; Kimiya, H.; Kobayashi, K.; Kominami, H.; Matsushige, K.; Yamada, H. *Nat. Mater.* **2014**, *13* (3), 264–270.

(14) Zhou, J.; Liang, D.; Contera, S. *Nanoscale* **2015**, *7* (40), 17102–17108.

(15) Shi, S.; Chen, X.; Liu, X.; Wu, X.; Liu, F.; Zhang, Z.-G.; Li, Y.; Russell, T. P.; Wang, D. *ACS Appl. Mater. Interfaces* **2017**, *9* (29), 24451–24455.

(16) Chen, C. C.; Zhou, Y.; Baker, L. A. *Annu. Rev. Anal. Chem.* **2012**, *5* (1), 207–228.

(17) Page, A.; Perry, D.; Unwin, P. R. *Proc. R. Soc. A* **2017**, *473*, 20160889.

(18) Snowden, M. E.; Güell, A. G.; Lai, S. C. S.; McKelvey, K.; Ebejer, N.; O'Connell, M. A.; Colburn, A. W.; Unwin, P. R. *Anal. Chem.* **2012**, *84* (5), 2483–2491.

(19) Ebejer, N.; Güell, A. G.; Lai, S. C. S.; McKelvey, K.; Snowden, M. E.; Unwin, P. R. *Annu. Rev. Anal. Chem.* **2013**, *6*, 329–351.

(20) Güell, A. G.; Ebejer, N.; Snowden, M. E.; Macpherson, J. V.; Unwin, P. R. *J. Am. Chem. Soc.* **2012**, *134* (17), 7258–7261.

(21) Kinnear, S. L.; McKelvey, K.; Snowden, M. E.; Peruffo, M.; Colburn, A. W.; Unwin, P. R. *Langmuir* **2013**, *29*, 15565–15572.

(22) Bard, A. J.; Fan, F.-R. F.; Kwak, J.; Lev, O. *Anal. Chem.* **1989**, *61* (2), 132–138.

(23) Kwak, J.; Bard, A. J. *Anal. Chem.* **1989**, *61*, 1794–1799.

(24) Amemiya, S.; Bard, A. J.; Fan, F.-R. F.; Mirkin, M. V.; Unwin, P. R. *Annu. Rev. Anal. Chem.* **2008**, *1*, 95–131.

(25) Zoski, C. G. *J. Electrochem. Soc.* **2016**, *163* (4), H3088–H3100.

(26) Zoski, C. G. *Electroanalysis* **2002**, *14* (15–16), 1041–1051.

(27) Macpherson, J. V.; Unwin, P. R. *J. Phys. Chem.* **1995**, *99* (40), 14824–14831.

(28) Schulte, A.; Nebel, M.; Schuhmann, W. *Annu. Rev. Anal. Chem.* **2010**, *3*, 299–318.

(29) Kim, J.; Shen, M.; Nioradze, N.; Amemiya, S. *Anal. Chem.* **2012**, *84* (8), 3489–3492.

(30) Sun, T.; Yu, Y.; Zacher, B. J.; Mirkin, M. V. *Angew. Chem., Int. Ed.* **2014**, *53* (51), 14120–14123.

(31) Takahashi, Y.; Miyamoto, T.; Shiku, H.; Ino, K.; Yasukawa, T.; Asano, R.;

Kumagai, I.; Matsue, T. *Phys. Chem. Chem. Phys.* **2011**, *13* (37), 16569–16573.

(32) Bergner, S.; Vatsyayan, P.; Matysik, F. *Anal. Chim. Acta* **2013**, *775*, 1–13.

(33) Li, M. S. M.; Filice, F. P.; Ding, Z. *J. Electroanal. Chem.* **2016**, *779*, 176–186.

(34) Bondarenko, A.; Lin, T.-E.; Stupar, P.; Lesch, A.; Cortes-Salazar, F.; Girault, H. H.; Pick, H. M. *Anal. Chem.* **2016**, *88* (23), 11436–11443.

(35) Henderson, J. D.; Filice, F. P.; Li, M. S. M.; Ding, Z. *ChemElectroChem* **2017**, *4* (4), 856–863.

(36) Bae, J. H.; Yu, Y.; Mirkin, M. V. *J. Phys. Chem. C* **2016**, *120* (37), 20651–20658.

(37) Izquierdo, J.; Nagy, L.; Varga, Á.; Bitter, I.; Nagy, G.; Souto, R. M. *Electrochim. Acta* **2012**, *59*, 398–403.

(38) Takahashi, Y.; Shevchuk, A. I.; Novak, P.; Murakami, Y.; Shiku, H.; Korchev, Y. E.; Matsue, T. *J. Am. Chem. Soc.* **2010**, *132* (29), 10118–10126.

(39) Comstock, D. J.; Elam, J. W.; Pellin, M. J.; Hersam, M. C. *Anal. Chem.* **2010**, *82* (4), 1270–1276.

(40) Takahashi, Y.; Shevchuk, A. I.; Novak, P.; Zhang, Y.; Ebejer, N.; Macpherson, J. V.; Unwin, P. R.; Pollard, A. J.; Roy, D.; Clifford, C. A.; Shiku, H.; Matsue, T.; Klenerman, D.; Korchev, Y. E. *Angew. Chem., Int. Ed.* **2011**, *50* (41), 9638–9642.

(41) Morris, C. A.; Chen, C.-C.; Baker, L. A. *Analyst* **2012**, *137* (13), 2933–2938.

(42) Macpherson, J. V.; Unwin, P. R. *Anal. Chem.* **2000**, *72* (2), 276–285.

(43) Kranz, C.; Friedbacher, G.; Mizaikofft, B.; Lugstein, A.; Smoliner, J.; Bertagnolli, E. *Anal. Chem.* **2001**, *73* (11), 2491–2500.

(44) Kueng, A.; Kranz, C.; Lugstein, A.; Bertagnolli, E.; Mizaikoff, B. *Angew. Chem., Int. Ed.* **2003**, *42* (28), 3238–3240.

(45) Nellist, M. R.; Chen, Y.; Mark, A.; Gödrich, S.; Stelling, C.; Jiang, J.; Poddar, R.; Li, C.; Kumar, R.; Papastavrou, G.; Retsch, M.; Brunschwig, B. S.; Huang, Z.; Xiang, C.; Boettcher, S. W. *Nanotechnology* **2017**, *28* (9), 95711.

(46) Meier, J.; Friedrich, K. A.; Stimming, U. *Faraday Discuss.* **2002**, *121*, 365–372.

(47) Sklyar, O.; Treutler, T. H.; Vlachopoulos, N.; Wittstock, G. *Surf. Sci.* **2005**,

597 (1–3), 181–195.

(48) Nioradze, N.; Chen, R.; Kim, J.; Shen, M.; Santhosh, P.; Amemiya, S. *Anal. Chem.* **2013**, *85* (13), 6198–6202.

(49) Laforge, F. O.; Velmurugan, J.; Wang, Y.; Mirkin, M. V. *Anal. Chem.* **2009**, *81* (8), 3143–3150.

(50) Yu, Y.; Sun, T.; Mirkin, M. V. *Anal. Chem.* **2015**, *87* (14), 7446–7453.

(51) Kim, J.; Renault, C.; Nioradze, N.; Arroyo-Currás, N.; Leonard, K. C.; Bard, A. J. *J. Am. Chem. Soc.* **2016**, *138* (27), 8560–8568.

(52) Chen, R.; Hu, K.; Yu, Y.; Mirkin, M. V.; Amemiya, S. *J. Electrochem. Soc.* **2016**, *163* (4), H3032–H3037.

(53) Zoski, C. G. *Curr. Opin. Electrochem.* **2017**, *1* (1), 46–52.

(54) Kim, J.; Renault, C.; Nioradze, N.; Arroyo-Curras, N.; Leonard, K. C.; Bard, A. J. *Anal. Chem.* **2016**, *88* (20), 10284–10289.

(55) Kaya, T.; Torisawa, Y. S.; Oyamatsu, D.; Nishizawa, M.; Matsue, T. *Biosens. Bioelectron.* **2003**, *18* (11), 1379–1383.

(56) Korchev, Y. E.; Gorelik, J.; Lab, M. J.; Sviderskaya, E. V; Johnston, C. L.; Coombes, C. R.; Vodyanoy, I.; Edwards, C. R. *Biophys. J.* **2000**, *78* (1), 451–457.

(57) Gorelik, J.; Yang, L. Q.; Zhang, Y.; Lab, M.; Korchev, Y.; Harding, S. E. *Cardiovasc. Res.* **2006**, *72* (3), 422–429.

(58) McKelvey, K.; Perry, D.; Byers, J. C.; Colburn, A. W.; Unwin, P. R. *Anal. Chem.* **2014**, *86* (7), 3639–3646.

(59) McKelvey, K.; Kinnear, S. L.; Perry, D.; Momotenko, D.; Unwin, P. R. *J. Am. Chem. Soc.* **2014**, *136* (39), 13735–13744.

(60) Perry, D.; Al Botros, R.; Momotenko, D.; Kinnear, S. L.; Unwin, P. R. *ACS Nano* **2015**, *9* (7), 7266–7276.

(61) Rheinlaender, J.; Geisse, N. A.; Proksch, R.; Schäffer, T. E. *Langmuir* **2011**, *27* (2), 697–704.

(62) Shevchuk, A. I.; Frolenkov, G. I.; Sanchez, D.; James, P. S.; Freedman, N.; Lab, M. J.; Jones, R.; Klenerman, D.; Korchev, Y. E. *Angew. Chem., Int. Ed.* **2006**, *45* (14), 2212–2216.

(63) Li, C.; Johnson, N.; Ostanin, V.; Shevchuk, A.; Ying, L.; Korchev, Y.; Klenerman, D. *Prog. Nat. Sci.* **2008**, *18* (6), 671–677.

(64) Gorelik, J.; Shevchuk, A. I.; Frolenkov, G. I.; Diakonov, I. A.; Lab, M. J.; Kros, C. J.; Richardson, G. P.; Vodyanoy, I.; Edwards, C. R.; Klenerman, D.; Korchev, Y. E. *Proc. Natl. Acad. Sci. U. S. A.* **2003**, *100* (10), 5819–5822.

(65) Klenerman, D.; Korchev, Y. E.; Davis, S. J. *Curr. Opin. Chem. Biol.* **2011**, *15* (5), 696–703.

(66) Rheinlaender, J.; Schäffer, T. E. *Soft Matter* **2013**, *9* (12), 3230.

(67) Happel, P.; Hoffmann, G.; Mann, S. A.; Dietzel, I. D. *J. Microsc.* **2003**, *212* (2), 144–151.

(68) Shin, W.; Gillis, K. D. *Biophys. J.* **2006**, *91* (6), L63–L65.

(69) Pellegrino, M.; Orsini, P.; De Gregorio, F. *Neurosci. Res.* **2009**, *64* (3), 290–296.

(70) Yang, X.; Liu, X.; Zhang, X.; Lu, H.; Zhang, J.; Zhang, Y. *Ultramicroscopy* **2011**, *111* (8), 1417–1422.

(71) Miragoli, M.; Moshkov, A.; Novak, P.; Shevchuk, A.; Nikolaev, V. O.; El-Hamamsy, I.; Potter, C. M. F.; Wright, P.; Kadir, S. H. S. A.; Lyon, A. R.; Mitchell, J. a; Chester, A. H.; Klenerman, D.; Lab, M. J.; Korchev, Y. E.; Harding, S. E.; Gorelik, J. *J. R. Soc. Interface* **2011**, *8* (60), 913–925.

(72) Zhang, S.; Cho, S.-J.; Busuttil, K.; Wang, C.; Besenbacher, F.; Dong, M. *Nanoscale* **2012**, *4* (10), 3105.

(73) Korchev, Y. E.; Bashford, C. L.; Milovanovic, M.; Vodyanoy, I.; Lab, M. J. *Biophys. J.* **1997**, *73* (2), 653–658.

(74) Korchev, Y. E.; Milovanovic, M.; Bashford, C. L.; Bennett, D. C.; Sviderskaya, E. V; Vodyanoy, I.; Lab, M. J. *J. Microsc.* **1997**, *188* (1), 17–23.

(75) Novak, P.; Li, C.; Shevchuk, A. I.; Stepanyan, R.; Caldwell, M.; Hughes, S.; Smart, T. G.; Gorelik, J.; Ostanin, V. P.; Lab, M. J.; Moss, G. W. J.; Frolenkov, G. I.; Klenerman, D.; Korchev, Y. E. *Nat. Methods* **2009**, *6* (4), 279–281.

(76) Korchev, Y. E.; Negulyaev, Y. A.; Edwards, C. R.; Vodyanoy, I.; Lab, M. J. *Nat. Cell Biol.* **2000**, *2* (9), 616–619.

(77) Shi, W.; Friedman, A. K.; Baker, L. A. *Anal. Chem.* **2016**, *89* (1), 157–188.

(78) Chen, C. C.; Derylo, M. A.; Baker, L. A. *Anal. Chem.* **2009**, *81* (12), 4742–4751.

(79) Pastre, D.; Iwamoto, H.; Liu, J.; Szabo, G.; Shao, Z. *Ultramicroscopy* **2001**,

90 (1), 13–19.

(80) Chen, C. C.; Zhou, Y.; Baker, L. A. *ACS Nano* **2011**, *5* (10), 8404–8411.

(81) Ying, L.; Bruckbauer, A.; Rothery, A. M.; Korchev, Y. E.; Klenerman, D. *Anal. Chem.* **2002**, *74* (6), 1380–1385.

(82) Ivanov, A. P.; Actis, P.; Jönsson, P.; Klenerman, D.; Korchev, Y.; Edel, J. B. *ACS Nano* **2015**, *9* (4), 3587–3595.

(83) Bruckbauer, A.; Ying, L.; Rothery, A. M.; Zhou, D.; Shevchuk, A. I.; Abell, C.; Korchev, Y. E.; Klenerman, D. *J. Am. Chem. Soc.* **2002**, *124* (30), 8810–8811.

(84) Bruckbauer, A.; James, P.; Zhou, D.; Yoon, J. W.; Excell, D.; Korchev, Y.; Jones, R.; Klenerman, D. *Biophys. J.* **2007**, *93* (9), 3120–3131.

(85) Babakinejad, B.; Jönsson, P.; López Córdoba, A.; Actis, P.; Novak, P.; Takahashi, Y.; Shevchuk, A.; Anand, U.; Anand, P.; Drews, A.; Ferrer-Montiel, A.; Klenerman, D.; Korchev, Y. E. *Anal. Chem.* **2013**, *85* (19), 9333–9342.

(86) Schobesberger, S.; Jönsson, P.; Buzuk, A.; Korchev, Y.; Siggers, J.; Gorelik, J. *Biophys. J.* **2016**, *110* (1), 141–146.

(87) Actis, P.; Maalouf, M. M.; Kim, H. J.; Lohith, A.; Vilozny, B.; Seger, R. A.; Pourmand, N. *ACS Nano* **2014**, *8* (1), 546–553.

(88) Yuill, E. M.; Sa, N.; Ray, S. J.; Hieftje, G. M.; Baker, L. A. *Anal. Chem.* **2013**, *85* (18), 8498–8502.

(89) Yuill, E. M.; Shi, W.; Poehlman, J.; Baker, L. A. *Anal. Chem.* **2015**, *87* (22), 11182–11186.

(90) Momotenko, D.; Byers, J. C.; McKelvey, K.; Kang, M.; Unwin, P. R. *ACS Nano* **2015**, *9* (9), 8942–8952.

(91) Momotenko, D.; McKelvey, K.; Kang, M.; Meloni, G. N.; Unwin, P. R. *Anal. Chem.* **2016**, *88* (5), 2838–2846.

(92) Perry, D.; Momotenko, D.; Lazenby, R. A.; Kang, M.; Unwin, P. R. *Anal. Chem.* **2016**, *88* (10), 5523–5530.

(93) Edwards, M. A.; Williams, C. G.; Whitworth, A. L.; Unwin, P. R. *Anal. Chem.* **2009**, *81* (11), 4482–4492.

(94) Rheinlaender, J.; Schäffer, T. E. *J. Appl. Phys.* **2009**, *105*, 94905.

(95) Weber, A. E.; Baker, L. A. *J. Electrochem. Soc.* **2014**, *161* (14), H924–H929.

(96) Takahashi, Y.; Ito, K.; Wang, X.; Matsumae, Y.; Komaki, H.; Kumatani, A.; Ino, K.; Shiku, H.; Matsue, T. *Electrochemistry* **2014**, *82*, 331–334.

(97) Karhanek, M.; Kemp, J. T.; Pourmand, N.; Davis, R. W.; Webb, C. D. *Nano Lett*. **2005**, *5* (2), 403–407.

(98) Behrens, S. H.; Grier, D. G. *J. Chem. Phys*. **2001**, *115* (14), 6716–6721.

(99) Wei, C.; Bard, A. J.; Feldberg, S. W. *Anal. Chem*. **1997**, *69* (22), 4627–4633.

(100) Siwy, Z.; Heins, E.; Harrell, C. C.; Kohli, P.; Martin, C. R. *J. Am. Chem. Soc*. **2004**, *126* (35), 10850–10851.

(101) White, H. S.; Bund, A. *Langmuir* **2008**, *24* (5), 2212–2218.

(102) Momotenko, D.; Cortes-Salazar, F.; Josserand, J.; Liu, S.; Shao, Y.; Girault, H. H. *Phys. Chem. Chem. Phys*. **2011**, *13*, 5430–5440.

(103) Momotenko, D.; Girault, H. H. *J. Am. Chem. Soc*. **2011**, *133* (37), 14496–14499.

(104) Lan, W. J.; Holden, D. A.; White, H. S. *J. Am. Chem. Soc*. **2011**, *133* (34), 13300–13303.

(105) Yin, X.; Zhang, S.; Dong, Y.; Liu, S.; Gu, J.; Chen, Y.; Zhang, X.; Zhang, X.; Shao, Y. *Anal. Chem*. **2015**, *87* (17), 9070–9077.

(106) Rosentsvit, L.; Wang, W.; Schiffbauer, J.; Chang, H. C.; Yossifon, G. *J. Chem. Phys*. **2015**, *143* (22), 224706.

(107) Rodolfa, K. T.; Bruckbauer, A.; Zhou, D.; Korchev, Y. E.; Klenerman, D. *Angew. Chem., Int. Ed*. **2005**, *44* (42), 6854–6859.

(108) Chen, C. C.; Zhou, Y.; Morris, C. A.; Hou, J.; Baker, L. A. *Anal. Chem*. **2013**, *85*, 3621–3628.

(109) Zhou, L.; Zhou, Y.; Baker, L. A. *Electrochem. Soc. Interface* **2014**, *23* (2), 47–52.

(110) Zhou, Y.; Chen, C. C.; Weber, A. E.; Zhou, L.; Baker, L. A. *Tissue Barriers* **2014**, *30* (19), 5669–5675.

(111) Zhou, L.; Zeng, Y.; Baker, L. A.; Hou, J. *Tissue Barriers* **2015**, *3* (4), 1105907.

(112) Zhou, L.; Zhou, Y.; Shi, W.; Baker, L. A. *J. Phys. Chem. C* **2015**, *119*, 14392–14399.

(113) Chen, C.-H.; Meadows, K. E.; Cuharuc, A.; Lai, S. C. S.; Unwin, P. R. *Phys. Chem. Chem. Phys*. **2014**, *16*, 18545–18552.

(114) Güell, A. G.; Cuharuc, A. S.; Kim, Y. R.; Zhang, G.; Tan, S. Y.; Ebejer, N.; Unwin, P. R. *ACS Nano* **2015**, *9* (4), 3558–3571.

(115) Patten, H. V.; Lai, S. C. S.; Macpherson, J. V.; Unwin, P. R. *Anal. Chem.* **2012**, *84* (12), 5427–5432.

(116) Parker, A. S.; Al Botros, R.; Kinnear, S. L.; Snowden, M. E.; McKelvey, K.; Ashcroft, A. T.; Carvell, M.; Joiner, A.; Peruffo, M.; Philpotts, C.; Unwin, P. R. *J. Colloid Interface Sci.* **2016**, *476*, 94–102.

(117) McKelvey, K.; O'Connell, M. A.; Unwin, P. R. *Chem. Commun.* **2013**, *49* (29), 2986–2988.

(118) Oseland, E. E.; Ayres, Z. J.; Basile, A.; Haddleton, D. M.; Wilson, P.; Unwin, P. R. *Chem. Commun.* **2016**, *52*, 9929–9932.

(119) Shi, W.; Zeng, Y.; Zhou, L.; Xiao, Y.; Cummins, T. R.; Baker, L. A. *Faraday Discuss.* **2016**, *193*, 81–97.

(120) Nadappuram, B. P.; McKelvey, K.; Al Botros, R.; Colburn, A. W.; Unwin, P. R. *Anal. Chem.* **2013**, *85* (17), 8070–8074.

(121) McKelvey, K.; Nadappuram, B. P.; Actis, P.; Takahashi, Y.; Korchev, Y. E.; Matsue, T.; Robinson, C.; Unwin, P. R. *Anal. Chem.* **2013**, *85* (15), 7519–7526.

(122) Brennan, L. D.; Roland, T.; Morton, D. G.; Fellman, S. M.; Chung, S. Y.; Soltani, M.; Kevek, J. W.; McEuen, P. M.; Kemphues, K. J.; Wang, M. D. *PLoS One* **2013**, *8* (9), 1–13.

(123) Hu, K.; Wang, Y.; Cai, H.; Mirkin, M. V.; Gao, Y.; Friedman, G.; Gogotsi, Y. *Anal. Chem.* **2014**, *86* (18), 8897–8901.

(124) Arowosola, A.; Fujimoto, A.; Scheibel, O.; Schrlau, M. G. *J. Multidiscip. Eng. Sci. Technol.* **2015**, *2* (5), 896–901.

(125) O'Connell, M. A.; Wain, A. J. *Anal. Chem.* **2014**, *86* (24), 12100–12107.

(126) Thakar, R.; Weber, A. E.; Morris, C. A.; Baker, L. A. *Analyst* **2013**, *138* (20), 5973–5982.

(127) O'Connell, M. A.; Lewis, J. R.; Wain, A. J. *Chem. Commun.* **2015**, *51*, 10314–10317.

(128) Şen, M.; Takahashi, Y.; Matsumae, Y.; Horiguchi, Y.; Kumatani, A.; Ino, K.; Shiku, H.; Matsue, T. *Anal. Chem.* **2015**, *87* (6), 3484–3489.

(129) Nadappuram, P. B.; McKelvey, K.; Byers, J. C.; Güell, A. G.; Colburn, A.

W.; Lazenby, R. A.; Unwin, P. R. *Anal. Chem.* **2015**, *87* (7), 3566–3573.

(130) Byers, J. C.; Nadappuram, B. P.; Perry, D.; McKelvey, K.; Colburn, A. W.; Unwin, P. R. *Anal. Chem.* **2015**, *87*, 10450–10456.

(131) Verwey, E. J. W. *J. Phys. Colloid Chem.* **1947**, *51* (3), 631–636.

(132) Terada, A.; Okuyama, K.; Nishikawa, M.; Tsuneda, S.; Hosomi, M. *Biotechnol. Bioeng.* **2012**, *109* (7), 1745–1754.

(133) Shi, X.; Bi, Y.; Yang, W.; Guo, X.; Jiang, Y.; Wan, C.; Li, L.; Bai, Y.; Guo, J.; Wang, Y.; Chen, X.; Wu, B.; Sun, H.; Liu, W.; Wang, J.; Xu, C. *Nature* **2013**, *493* (7430), 111–115.

(134) Guo, W.; Tian, Y.; Jiang, L. *Acc. Chem. Res.* **2013**, *46* (12), 2834–2846.

(135) Lehovec, K. *J. Chem. Phys.* **1953**, *21* (7), 1123.

(136) Williams, R.; Willis, A. *J. Appl. Phys.* **1968**, *39* (8), 3731–3736.

(137) Sahin, O.; Nusret Bulutcu, A. *J. Cryst. Growth* **2002**, *241* (4), 471–480.

(138) Lin, N. H.; Shih, W. Y.; Lyster, E.; Cohen, Y. *J. Colloid Interface Sci.* **2011**, *356* (2), 790–797.

(139) Hellevang, H.; Miri, R.; Haile, B. G. *Cryst. Growth Des.* **2014**, *14* (12), 6451–6458.

(140) Bakhti, M.; Snaidero, N.; Schneider, D.; Aggarwal, S.; Möbius, W.; Janshoff, A.; Eckhardt, M.; Nave, K.-A.; Simons, M. *Proc. Natl. Acad. Sci. U. S. A.* **2013**, *110* (8), 3143–3148.

(141) Busscher, H. J.; van der Mei, H. C. *PLoS Pathog.* **2012**, *8* (1), 1–3.

(142) Rivera-Gil, P.; Jimenez De Aberasturi, D.; Wulf, V.; Pelaz, B.; Del Pino, P.; Zhao, Y.; De La Fuente, J. M.; Ruiz De Larramendi, I.; Rojo, T.; Liang, X. J.; Parak, W. J. *Acc. Chem. Res.* **2013**, *46* (3), 743–749.

(143) Tedja, R.; Lim, M.; Amal, R.; Marquis, C. *ACS Nano* **2012**, *6* (5), 4083–4093.

(144) Kim, S. T.; Saha, K.; Kim, C.; Rotello, V. M. *Acc. Chem. Res.* **2013**, *46* (3), 681–691.

(145) Chung, T. H.; Wu, S. H.; Yao, M.; Lu, C. W.; Lin, Y. S.; Hung, Y.; Mou, C. Y.; Chen, Y. C.; Huang, D. M. *Biomaterials* **2007**, *28* (19), 2959–2966.

(146) Wong, J. Y.; Langer, R.; Ingber, D. E. *Proc. Natl. Acad. Sci. U. S. A.* **1994**, *91* (8), 3201–3204.

(147) Haupt, A.; Campetelli, A.; Bonazzi, D.; Piel, M.; Chang, F.; Minc, N. *PLoS Biol.* **2014**, *12* (12), 1–13.

(148) Christianson, H. C.; Svensson, K. J.; van Kuppevelt, T. H.; Li, J.-P.; Belting, M. *Proc. Natl. Acad. Sci. U. S. A.* **2013**, *110* (43), 17380–17385.

(149) Parsons, R. *Chem. Rev* **1990**, *90*, 813–826.

(150) Bard, A. J.; Faulkner, L. R. *Electrochemical Methods: Fundamentals and Application*; Wiley, 1980.

(151) Grahame, D. C. *J. Am. Chem. Soc.* **1941**, *63* (5), 1207–1215.

(152) Grahame, D. C. *J. Am. Chem. Soc.* **1946**, *68* (2), 301–310.

(153) Grahame, D. C. *Chem. Rev.* **1947**, *41* (3), 441–501.

(154) Stumm, W.; Morgan, J. J. *Aquatic chemistry: chemical equilibria and rates in natural waters*; John Wiley & Sons, 1996.

(155) Sprycha, R. *J. Colloid Interface Sci.* **1989**, *127* (1), 1–11.

(156) Arjmandi, N.; Van Roy, W.; Lagae, L.; Borghs, G. *Anal. Chem.* **2012**, *84* (20), 8490–8496.

(157) Freitas, C.; Muller, R. H. *Int. J. Pharm.* **1998**, *168* (2), 221–229.

(158) Vallar, S.; Houivet, D.; El Fallah, J.; Kervadec, D.; Haussonne, J. M. *J. Eur. Ceram. Soc.* **1999**, *19*, 1017–1021.

(159) Hormeño, S.; Penedo, M.; Manzano, C. V; Sadewasser, S.; Carl, P.; Glatzel, T.; Palacios-lidón, E.; Colchero, J.; Girard, P. *Nanotechnology* **2001**, *12* (4), 485–490.

(160) Moser, J.; Verdaguer, A.; Jiménez, D.; Barreiro, A.; Bachtold, A.; Moser, J.; Verdaguer, A.; Jiménez, D.; Barreiro, A.; Bachtold, A. *Appl. Phys. Lett.* **2008**, *92*, 123507.

(161) Kulkarni, D. D.; Kim, S.; Chyasnavichyus, M.; Hu, K.; Fedorov, A. G.; Tsukruk, V. V. *J. Am. Chem. Soc.* **2014**, *136*, 6546–6549.

(162) Hong, J. W.; Noh, K. H.; Park, S. *Phys. Rev. B* **1998**, *58* (8), 5078–5084.

(163) Malvankar, N. S.; Yalcin, S. E.; Tuominen, M. T.; Lovley, D. R. *Nat. Nanotechnol.* **2014**, *9* (12), 1012–1017.

(164) Xu, S.; Arnsdorf, M. F. *Proc. Natl. Acad. Sci. U. S. A.* **1995**, *92*, 10384–10388.

(165) Butt, H. *Biophys. J.* **1991**, *60*, 777–785.

(166) Sotres, J.; Baró, A. M. *Appl. Phys. Lett.* **2008**, *93*, 103903.

(167) Sotres, J.; Baro, A. M. *Biophys. J.* **2010**, *98*, 1995–2004.

(168) Miyatani, T.; Okamoto, S.; Rosa, A.; Marti, O.; Fujihira, M. *Appl. Phys. A*

Mater. Sci. Process. **1998**, *352*, 349–352.

(169) Heinz, W. F.; Hoh, J. H. *Biophys. J.* **1999**, *76* (1), 528–538.

(170) Heinz, W. F.; Hoh, J. H. *Trends Biotechnol.* **1999**, *17* (4), 143–150.

(171) Zimmerman, B.; Chow, J.; Abbott, A. G.; Ellison, M. S.; Kennedy, M. S.; Dean, D. *J. Eng. Fiber. Fabr.* **2011**, *6* (2), 61–66.

(172) Almonte, L.; Lopez-Elvira, E.; Baró, A. M. *ChemPhysChem* **2014**, *15* (13), 2768–2773.

(173) Perry, D.; Paulose Nadappuram, B.; Momotenko, D.; Voyias, P. D.; Page, A.; Tripathi, G.; Frenguelli, B. G.; Unwin, P. R. *J. Am. Chem. Soc.* **2016**, *138* (9), 3152–3160.

(174) Nonnenmacher, M.; Boyle, M. P. O.; Wickramasinghe, H. K. *Appl. Phys. Lett.* **1991**, *58*, 2921–2923.

(175) Jacobs, H. O.; Leuchtmann, P.; Homan, O. J.; Stemmer, A. *J. Appl. Phys.* **1998**, *84* (3), 1168–1173.

(176) Fujihira, M. *Annu. Rev. Mater. Sci.* **1999**, *29* (1), 353–380.

(177) Melitz, W.; Shen, J.; Kummel, A. C.; Lee, S. *Surf. Sci. Rep.* **2011**, *66* (1), 1–27.

(178) Clack, N. G.; Salaita, K.; Groves, J. T. *Nat. Biotechnol.* **2008**, *26* (7), 825–830.

(179) Finot, E.; Leonenko, Y.; Moores, B.; Eng, L.; Amrein, M.; Leonenko, Z. *Langmuir* **2010**, *26* (3), 1929–1935.

(180) Pattnaik, P. *Appl. Biochem. Biotechnol.* **2005**, *126* (2), 79–92.

(181) Shan, X. N.; Huang, X. P.; Foley, K. J.; Zhang, P. M.; Chen, K. P.; Wang, S. P.; Tao, N. J. *Anal. Chem.* **2010**, *82* (1), 234–240.

(182) MacGriff, C.; Wang, S.; Wiktor, P.; Wang, W.; Shan, X.; Tao, N. *Anal. Chem.* **2013**, *85* (14), 6682–6687.

(183) Reid, M. S.; Kedzior, S. A.; Villalobos, M.; Cranston, E. D. *Langmuir* **2017**, *33* (30), 7403–7411.

(184) Sa, N.; Baker, L. A. *J. Am. Chem. Soc.* **2011**, *133* (27), 10398–10401.

(185) Sa, N.; Lan, W. J.; Shi, W.; Baker, L. A. *ACS Nano* **2013**, *7* (12), 11272–11282.

(186) Clarke, R. W.; Zhukov, A.; Richards, O.; Johnson, N.; Ostanin, V.; Klenerman, D. *J. Am. Chem. Soc.* **2013**, *135* (1), 322–329.

(187) Wang, T.; Bai, J.; Jiang, X.; Nienhaus, G. U. *ACS Nano* **2012**, *6* (2), 1251–1259.

(188) Rezgui, R.; Blumer, K.; Yeoh-Tan, G.; Trexler, A. J.; Magzoub, M. *Biochim. Biophys. Acta, Biomembr.* **2016**, *1858* (7), 1499–1506.

(189) Tsang, C. N.; Ho, K. S.; Sun, H.; Chan, W. T. *J. Am. Chem. Soc.* **2011**, *133* (19), 7355–7357.

(190) Passarelli, M. K.; Newman, C. F.; Marshall, P. S.; West, A.; Gilmore, I. S.; Bunch, J.; Alexander, M. R.; Dollery, C. T. *Anal. Chem.* **2015**, *87* (13), 6696–6702.

(191) Yasukawa, T.; Kondo, Y.; Uchida, I.; Matsue, T. *Chem. Lett.* **1998**, *8*, 767–768.

(192) Kaya, T.; Numai, D.; Nagamine, K.; Aoyagi, S.; Shiku, H.; Matsue, T. *Analyst* **2004**, *129* (6), 529–534.

(193) Mauzeroll, J.; Bard, A. J. *Proc. Natl. Acad. Sci. U. S. A.* **2004**, *101* (21), 7862–7867.

(194) Zhan, D.; Fan, F.-R. F.; Bard, A. J. *Proc. Natl. Acad. Sci. U. S. A.* **2008**, *105* (34), 12118–12122.

(195) Li, M. S. M.; Filice, F. P.; Henderson, J. D.; Ding, Z. *J. Phys. Chem. C* **2016**, *120* (11), 6094–6103.

(196) Henderson, J. D.; Filice, F. P.; Li, M. S. M.; Ding, Z. *J. Inorg. Biochem.* **2016**, *158*, 92–98.

(197) Filice, F. P.; Li, M. S. M.; Ding, Z. *Anal. Chim. Acta* **2016**, *908*, 85–94.

(198) Takahashi, Y.; Shevchuk, A. I.; Novak, P.; Babakinejad, B.; Macpherson, J.; Unwin, P. R.; Shiku, H.; Gorelik, J.; Klenerman, D.; Korchev, Y. E.; Matsue, T. *Proc. Natl. Acad. Sci. U. S. A.* **2012**, *109*, 11540–11545.

(199) Nebel, M.; Grützke, S.; Diab, N.; Schulte, A.; Schuhmann, W. *Angew. Chem., Int. Ed.* **2013**, *52* (24), 6335–6338.

(200) Soldà, A.; Valenti, G.; Marcaccio, M.; Giorgio, M.; Pelicci, P. G.; Paolucci, F.; Rapino, S. *ACS Sensors* **2017**, DOI: acssensors.7b00324.

2 Quantitative Visualization of Molecular Delivery and Uptake at Living Cells with Self-Referencing Scanning Ion Conductance Microscopy-Scanning Electrochemical Microscopy

In this chapter, the multifunctional abilities of SICM are explored when integrated into a dual-barrel probe with a solid SECM electrode. The SICM channel predominantly functions as a means for topographical feedback, but is also a reservoir of redox-active molecules that are reduced at the adjacent SECM channel. The current measured at the SECM electrode is a sensor of the local concentration of redox molecules, and this current is monitored upon approach to a surface, with the change in SECM current corresponding to a certain rate of uptake at the surface. This regime is used to map the uptake of hexaammineruthenium(III) into *Zea mays* root hair cells, whilst simultaneously measuring the sample topography. The sensitivity of the SICM-SECM setup is sufficient to resolve sub-cellular differences in molecular uptake, and these differences are then quantified using three-dimensional FEM simulations.

This chapter was published as an article in *Analytical Chemistry*. All experiments and simulations were carried out by the author, with advice from Minkyung Kang and Dr. David Perry. Minkyung Kang performed all of the electron microscopy in this study, and Alexander Armitstead carried out some preliminary work not included herein. The manuscript was written by the author.

Quantitative Visualization of Molecular Delivery and Uptake at Living Cells with Self-Referencing Scanning Ion Conductance Microscopy-Scanning Electrochemical Microscopy

Ashley Page,[1,2] Minkyung Kang,[1] Alexander Armitstead,[1] David Perry[1,2] and Patrick R. Unwin[1,].*

[1]Department of Chemistry and [2]MOAC Doctoral Training Centre, University of Warwick, Coventry, CV4 7AL, United Kingdom

*corresponding author

p.r.unwin@warwick.ac.uk

2.1 Abstract

A multifunctional dual-channel scanning probe nanopipette that enables simultaneous scanning ion conductance microscopy (SICM) and scanning electrochemical microscopy (SECM) measurements is demonstrated to have powerful new capabilities for spatially mapping the uptake of molecules of interest at living cells. One barrel of the probe is filled with electrolyte and the molecules of interest and is open to the bulk solution for both topographical feedback and local delivery to a target interface, while a solid carbon electrode in the other barrel measures the local concentration and flux of the delivered molecules. This setup allows differentiation in molecular uptake rate across several regions of single cells with individual measurements at nanoscale resolution. Further, operating in a 'hopping mode', where the probe is translated towards the interface (cell) at each point allows self-referencing to be employed, in which the carbon electrode response is calibrated at each and every pixel for comparison to the bulk measurement. This is particularly important for measurements in living systems where an electrode response may change over time. Finite element method (FEM) modeling places the technique on a quantitative footing to allow the response of the carbon electrode and local delivery rates to be quantified. The technique is extremely versatile, with the local delivery of molecules highly tuneable via control of the SICM bias to promote or restrict migration from the pipette orifice. It is expected to have myriad applications from drug delivery to screening catalysts.

2.2 Introduction

All living cells, irrespective of whether they are plant, animal or bacterial, are continuously exchanging molecules with their extracellular environment. These molecules can range from the small diatomic oxygen (O_2) used in cellular respiration,[1–3] to cytokines,[4] signalling proteins used for intercellular communication that can be 20 kDa or larger in size. The passage of any species from the extracellular to the intracellular domain or vice-versa is dependent on a host of factors, including molecule size and charge,[5,6] physiological conditions and environment,[7] relative concentrations inside and outside of the cell[8] and the presence of suitable membrane proteins if assisted transport is necessary.[9,10] The dependence of uptake on such a wide variety of factors, and the fact that uptake is a complex process involving mass transport (diffusion) and interfacial (membrane) processes, imposes critical requirements on analytical techniques if key details on uptake are to be revealed. Although cell uptake measurements are an essential aspect of new drug development, current methods often use bulk cytotoxicity assays and, at best, whole single cell measurements to ascertain the efficacy of a drug.[11–14]

Scanning electrochemical probe microscopies (SEPMs) have great potential to increase the precision of cellular uptake measurements, particularly as the production of functional nanoscale probes is becoming easier.[15] Hitherto, scanning electrochemical microscopy (SECM)[16] and scanning ion conductance microscopy (SICM)[17] have been the main SEPMs used for cell imaging. SICM has mainly being used for high resolution topographical imaging,[18,19] while SECM has found considerable application for imaging a variety of processes at living cells.[20,21] However, measurements of cell permeability with SECM are somewhat scarce[22,23] and challenging, because existing detection schemes, such as the induced transfer mode,[24] require careful deconvolution of topography and induced transfer (interfacial kinetics). Furthermore, this mode involves the ‘extraction’ of analyte by diffusion from within a cell or tissue, which may not give an accurate measurement of permeability if the analyte is consumed or irreversibly bound inside the cell.

Here, we report a new method combining SICM and SECM probes to determine the topography of a substrate, and cell permeability (molecular uptake) simultaneously and in real time. While integrated electrodes have previously been

used to monitor the efflux from micropipettes,[25,26] they have not been used to monitor uptake at cells and our work greatly develops the capability of SICM-SECM,[27–30] which has recently been applied to model substrates[27,28,31] and electrocatalysis at nanoparticles.[29,32]

The approach makes use of SICM-SECM as a multifunctional tool to spatially resolve the uptake of a molecule of interest to a single cell (SECM channel), whilst reliably positioning the probe at a defined distance from the interface for delivery and topography mapping (SICM channel). The analyte of interest is delivered to the cell in a defined and local manner. This is advantageous compared to the analyte being in bulk solution, because: (i) it allows the detection of *uptake*; (ii) the cell is only dosed transiently with the analyte, which *reduces potential toxicity issues*; and (iii) the response of the SECM and SICM channels can be calibrated *at each and every pixel*. Furthermore, the migration and thus delivery of molecules can be controlled by the polarity and magnitude of the applied SICM bias. As a proof of concept the uptake of the well-characterized redox mediator hexaammineruthenium(III), $[Ru(NH_3)_6]^{3+}$, into *Zea mays* root hair cells has been studied. The technique is comfortably able to differentiate between uptake over the cell and the lack of uptake over glass, and is further able to distinguish heterogeneities in uptake rates across different regions of cells. Interestingly, the rates correlate qualitatively to earlier measurements of membrane surface charge.[33] This sub-cellular resolution is a significant improvement on previous uptake assays and provides a roadmap to further refine the spatial and kinetic resolution. An important aspect of the method is that the probe response can be predicted with finite element modeling (FEM) to provide a robust platform on which the cellular uptake of any electroactive molecule of interest could potentially be studied at the nanoscale, and the method could be applied to many other types of interfaces in addition to cells.

2.3 Materials and Methods

2.3.1 Solutions: Milli-Q reagent grade water (resistivity ca. 18.2 MΩ cm at 25 °C) was used for all solutions. 10 mM KCl (Sigma-Aldrich, pH 6.5) was prepared and used for the bulk solution in all experiments. A solution of 10 mM

hexaammineruthenium(III) chloride (Sigma-Aldrich) and 10 mM KCl was prepared and used in the SICM barrel for all experiments.

2.3.2 Substrate Preparation: *Zea mays* seeds (Avenir, Syngenta) were germinated between two layers of damp paper towel at 25 °C for 4 days. This provided a root of approximately 20 mm length with a dense layer of root hair cells. The corn roots were then attached to a glass-bottomed Petri dish (3512, WillcoWells) using SPM adhesive tabs (Agar Scientific) away from the area being imaged.

2.3.3 Probe Fabrication: The fabrication of the nanoprobes used for SICM-SECM uptake mapping involved a multi-stage process. First, a dual-barrel quartz 'theta' capillary (o.d. 1.2 mm, i.d. 0.9 mm, Friedrich and Dimmock) was pulled to a sharp point of ~150 nm total diameter using a laser puller (P-2000, Sutter Instruments). One of the barrels was sealed with 'Blu-Tack' (Bostik) before butane was flowed down the other barrel in an argon atmosphere (Figure 2.1a). The probe was heated to pyrolytically deposit carbon within the barrel,[31,34] with the butane torch moved laterally, starting from beyond the end of the probe, over the tip and along the probe body. The burn time was typically 3 s at the tip and 10 s on the probe body to ensure that a thick layer of carbon was deposited.

An electrical connection to the SECM electrode was established by inserting a copper wire through the top end of the pipette barrel to make a back contact with the carbon layer. A transmission electron microscope (TEM, JEOL 2000FX) was used to investigate the carbon deposit (see inset micrographs, Figure 2.1a). The carbon deposit could be conformal to the end (left side image) or result in a recessed layer (right hand image). To avoid complications for an irregular SECM tip geometry, the overall probe diameter was increased to 500 nm using focused ion beam (FIB) milling (JEOL 4500) to ensure consistent probe geometry with a flush carbon electrode (Figure 2.1b), the response of which could be more accurately modeled. Ag/AgCl quasi-reference counter electrodes (QRCEs), comprising AgCl-coated Ag wire,[35,36] were used in the open barrel of the probe and in the bulk solution for SICM feedback (topographical imaging).

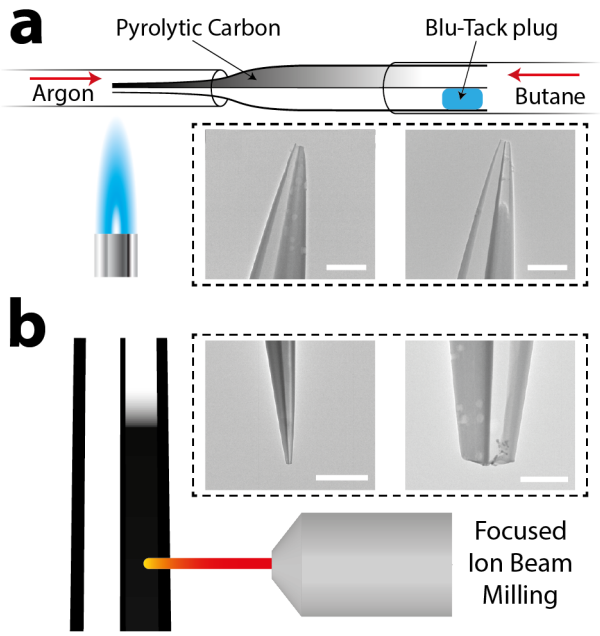

Figure 2.1. Fabrication of dual-barrel nanoprobes for use in SICM-SECM. (a) Carbon was deposited in one barrel of the probe via the pyrolysis of butane (SECM) while the other was kept open (SICM). Inset transmission electron microscopy (TEM) images show an example of both complete (left) and incomplete (right) carbon deposition. Scale bar in both micrographs is 500 nm. (b) The probe diameter was regulated using focused ion beam (FIB) milling. Inset TEM images show a probe with scale bars of 5 μm (left) and 500 nm (right) after FIB milling.

2.3.4 Instrumentation: The SICM-SECM setup was built on the stage of an inverted optical microscope (Axiovert 40 CFL, Zeiss) to facilitate the positioning of the nanoprobe relative to the substrate. Probe movement normal to the substrate was controlled using a piezoelectric positioning stage with a travel range of 38 μm (P-753-3CD, Physik Instrumente), while fine lateral movement of the substrate for XY positioning was achieved using a two-axis piezoelectric positioning system with a travel range of 300 μm (Nano-BioS300, Mad City Laboratories, Inc.). Instrumentation control and data collection was achieved using a custom-written LabVIEW (2013, National Instruments) program through an FPGA card (NI PCIe-7852R, National Instruments) and custom-built current amplifiers.

2.3.5 Simultaneous Topography and Uptake Mapping: To simultaneously image topography and uptake, the SICM-SECM probe was approached towards the surface at 2 μm s^{-1} (for small area scans) and 3 μm s^{-1} for larger scans (specified herein) until the ionic (SICM) current dropped by 1.5%, compared to the bulk value at each pixel. This was the feedback threshold used throughout. A hopping regime[28,37] was used to permit a quantifiable measurement to be taken at each pixel. The bias between the two QRCEs used for SICM feedback was 0.2 V with the positive bias applied at the QRCE in the SICM barrel. A bias of -0.4 V was applied to the carbon electrode with respect to the QRCE in bulk solution so as to reduce $[Ru(NH_3)_6]^{3+}$ to $[Ru(NH_3)_6]^{2+}$ at a transport-limited rate. The height of the substrate at each pixel was taken from the z-position at the point of closest approach based on the SICM response. The normalized SECM current response was calculated by dividing the faradaic reduction current value at the surface by that in bulk at the same pixel. The use of self-referencing data collection was extremely powerful, allowing the response of the probe to be recalibrated at every point in the scan.

2.3.6 Finite Element Model (FEM) Simulations: 3D FEM simulations were performed in COMSOL Multiphysics (v5.2) using the transport of diluted species and electrostatics modules. The dimensions of the probe for the simulation were taken from TEM micrographs.[38] The pipette was simulated as a double-barrel eccentric extruded cone with a total semi-major axis of 250 nm at the end of the pipette, and a semi-major axis of 160 nm for each of the two barrels. The height of the pipette simulated was 5 μm with an inner cone angle of 4.9°. A series of steady-state simulations were carried out at different probe-substrate separations, with a bias of +0.2 V in the pipette with respect to bulk, from which a working distance of 120 nm was determined from the drop in ionic current to the experimental feedback threshold. This separation was then used for further steady-state simulations with the probe positioned over surfaces with different uptake kinetics at the substrate boundary (first order heterogeneous rate constants, k, ranging from 1×10^{-5} to 1000 cm s^{-1}, see equation 2.1).

$$flux = -k[\mathrm{Ru(NH3)_6}]^{3+} \qquad (2.1)$$

A $[Ru(NH_3)_6]^{3+}$ concentration of 0 mM was applied to the boundary of the SECM electrode (diffusion-limited detection by reduction). Further details of all simulations, including the system of differential equations solved and all boundary conditions can be found in the Supporting Information, section 2.6.1.

2.4 Results and Discussion

2.4.1 Operational Principle: The use of a dual-barrel nanoprobe for the quantitative detection of cellular uptake is conditional on an intimate understanding of two well established scanning probe techniques: SICM and SECM. As highlighted in the Introduction, SICM utilizes the ionic current between two Ag/AgCl QRCEs, one in the probe and one in the bulk solution, as a feedback signal.[39] This current is dependent on the resistance in the system, which in bulk solution is determined almost exclusively by the aperture of the nanopipette, as the most resistive component.[40] However, as the probe approaches a surface (closer than one probe diameter) the system resistance increases as ion migration between the pipette and bulk solution is hindered by the surface. The corresponding decrease in current can therefore be used to set, and determine, the probe-substrate separation, and hence measure the topography of the substrate with a resolution on the same scale as the probe opening.[40] Note that for the probe sizes, distances, and electrolyte concentrations used herein the SICM current is immune to rectification effects.[41–43] SECM uses a solid micro- or nanoelectrode to probe the local concentration (or flux) of an electroactive species of interest. A potential is applied to the electrode to either oxidize or reduce the desired molecule, with the resulting faradaic current used to obtain flux information.

One QRCE was in the open (electrolyte-filled) barrel of the probe while another was in bulk, with a potential, V_1, applied between the two. The carbon electrode was connected to an offset electrometer that allowed the variation of the applied potential, V_2 - V_1, without affecting the bias used for SICM (Figure 2.2a). Both the bulk solution and the electrolyte channel of the probe contained 10 mM KCl. The molecule of interest (henceforth known as the 'analyte'), was hexaammineruthenium(III) ($[Ru(NH_3)_6]^{3+}$) as the chloride salt at a concentration of 10 mM, which was only in the electrolyte-filled barrel of the nanopipette. There was thus a concentration gradient of this species established around the tip of the probe

and the transport of analyte from the open channel to the face of the carbon electrode determined the SECM current signal observed. It is worth noting that while there are interdependent electrochemical and transport processes at the two channels, this interdependence is also treated in the simulations, with all simulations carried out with both the SICM and SECM channels 'on' and both V_1 and V_2 held constant throughout.

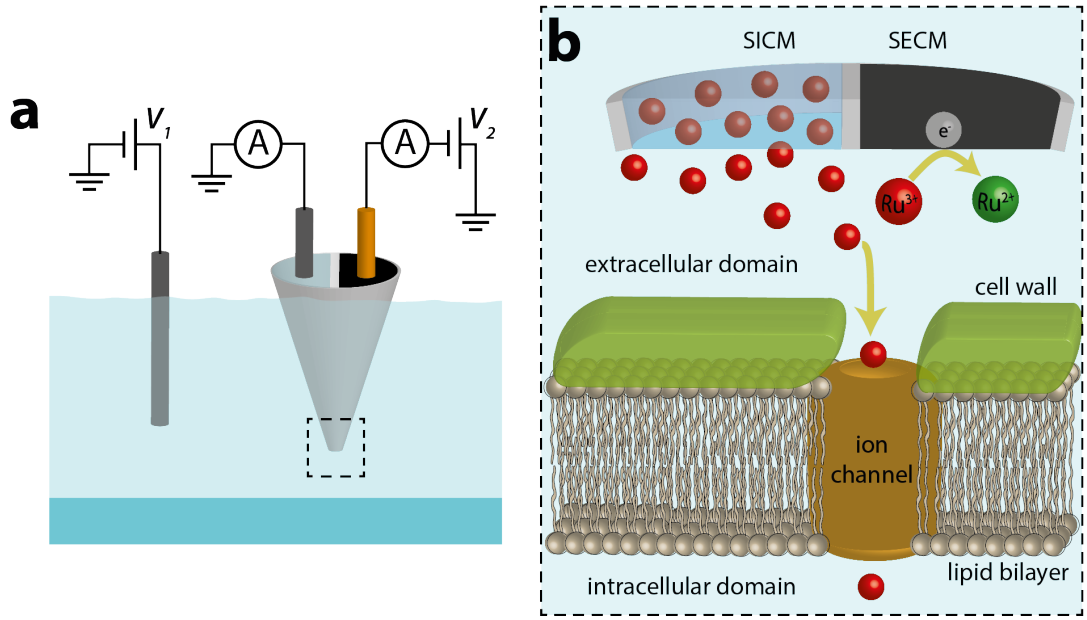

Figure 2.2. SICM-SECM experimental setup for the investigation of cellular uptake. (a) The current flowing between two Ag/AgCl QRCEs, one in bulk and one in the open channel of the probe, with an applied bias, V_1, used for topographical feedback in an SICM configuration. The carbon electrode used to measure the local concentration of the species is at a bias V_2 - V_1. (b) Schematic showing the diffusion-migration of $[Ru(NH_3)_6]^{3+}$ from the SICM barrel into the near cell region. The current due to the reduction of $[Ru(NH_3)_6]^{3+}$ at the SECM channel is monitored on approach of the probe to the surface and compared to the steady-state bulk current response to quantify uptake rates. It should be noted that transport via an ion channel is just one of many possible membrane transport mechanisms and is depicted herein for illustrative purposes.

Figure 2.2b is a schematic of an SICM-SECM probe near to a root hair cell. As $[Ru(NH_3)_6]^{3+}$ molecules are taken across the membrane it can be seen that, for a fixed probe-substrate separation, the SECM signal would be lower at this substrate than at a completely solid (impermeable) surface, where $[Ru(NH_3)_6]^{3+}$ would be partly trapped (hindered diffusion/migration) between the electrode and the surface. A specific normalized SECM current value (the ratio of the SECM current at the point of closest approach and the SECM current in bulk) thus corresponds to a specific level of uptake at the interface, as discussed in the next section.

2.4.2 FEM Simulations: FEM simulations of an SICM-SECM nanopipette (see Supporting Information, section 2.6.1 for full details) approaching a surface of zero uptake allowed the determination of a probe-substrate separation of 120 nm based on the 1.5% decrease of SICM current as the threshold used for the studies herein (Figure 2.3a). Further simulations were carried out with the probe at 120 nm above surfaces with varying analyte uptake rates, ranging from no uptake to a rate constant, k, of 1000 cm s^{-1} (see equation 2.1 above). Normalizing the steady-state SECM current values from these simulations to the value with the probe in bulk solution, 10 μm away from the surface, generated a calibration curve of normalized SECM current versus uptake rate constant for the quantitative estimation of uptake kinetics to a given surface (Figure 2.3b). It can be seen that this technique has a wide dynamic window, and is sensitive to rate constants from about 0.01 cm s^{-1} to 10 cm s^{-1}. This is a positive feature of the method. On the other hand, accurate measurements require that the SECM channel current can be determined with high precision, which is why self-referencing is important, as we show herein.

An investigation was carried out into whether or not the uptake rate constant at the surface would influence the SICM current signal, and thus the probe-substrate separation, the results of which are presented in section 2.6.2 of the Supporting Information. For the uptake rate constants observed in this study, and the tip-substrate separation used, the flux of $[Ru(NH_3)_6]^{3+}$ did not have a significant effect on the SICM current, with a small decrease predicted that was comparable to the noise of the SICM current measured experimentally. However, for a system where the uptake rate constant was higher (above 1 cm s^{-1}), the probe-substrate separation could be influenced by the uptake of the analyte. This issue could be countered by

employing an iterative approach in which both the separation and the uptake rate constant would be determined simultaneously over several rounds of simulations.

Experimentally the probe was retracted 15 μm and this tip-substrate separation and that used in the simulations (10 μm) are sufficient to represent bulk solution. The use of steady-state simulations is justified as the SECM response was the same at approach rates at least five times faster than those used experimentally, meaning that at any given point in the approach, the SECM current can be assumed to be at steady state. This is because the time to steady state at a nanoscale electrode is very short (see Supporting Information, section 2.6.3 for further justification of steady-state simulations). It should be noted that for all simulations of the SECM current, the SICM bias (+0.2 V at the QRCE in the probe) was applied, to imitate precisely the migration (as well as diffusion) of the $[Ru(NH_3)_6]^{3+}$ that occurs in the experiments.

Figure 2.3c shows the steady-state concentration profile of $[Ru(NH_3)_6]^{3+}$ with initial conditions mimicking those used experimentally, with the probe in bulk solution, and bias of +0.2 V vs. the bulk QRCE applied in SICM tip. The concentration at the nanopipette orifice is around 2 mM, one fifth of the bulk nanopipette concentration of 10 mM. This difference is noteworthy when using nanopipettes for local delivery, particularly drug delivery, as it is important to carefully dose the sample with a well-defined quantity (flux). A close-up of the end of the probe (Figure 2.3d) shows a departure from the expected hemispherical concentration profile at the end of the SICM barrel,[44] with the reduction of the $[Ru(NH_3)_6]^{3+}$ to $[Ru(NH_3)_6]^{2+}$ at the carbon electrode modifying the shape on the side closest to the solid amperometric sensor.

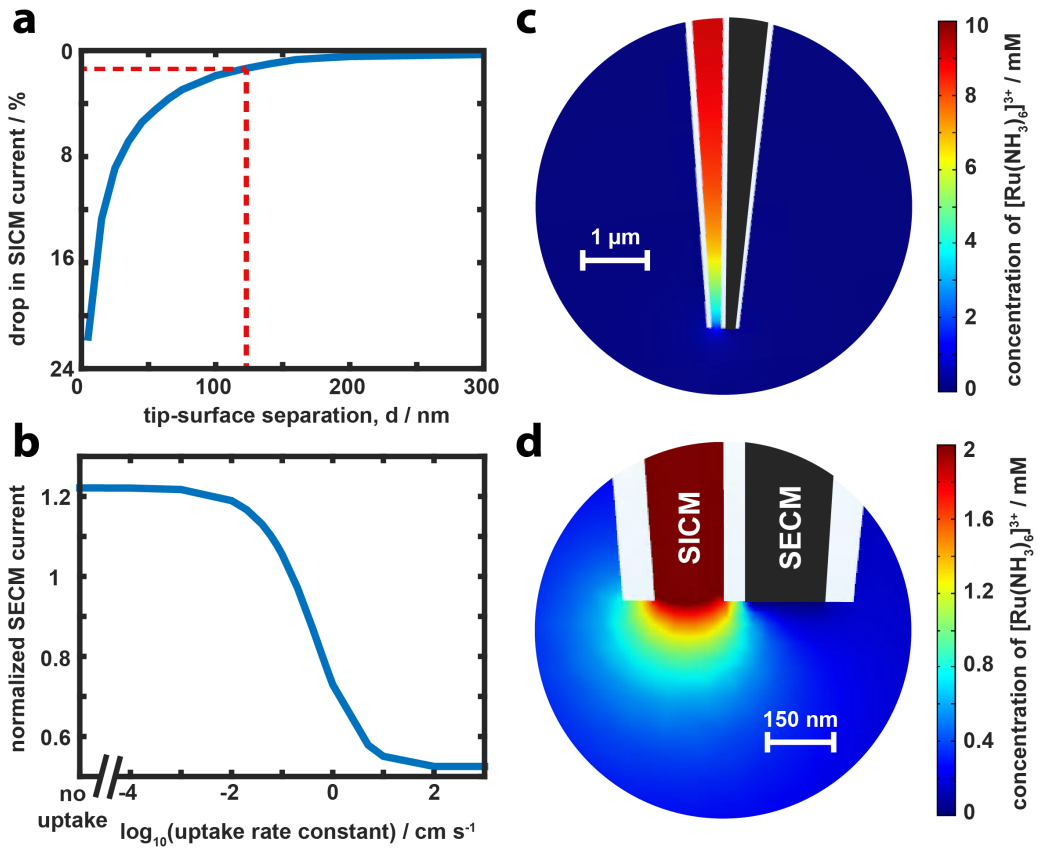

Figure 2.3. Finite element method (FEM) modeling of the SICM-SECM uptake system. (a) Simulated SICM approach curve (current vs. distance) to a surface of zero uptake with a probe of the same geometry as used experimentally, with electrochemistry switched on at the SECM channel. The current data are plotted as the percentage drop in ionic current from the bulk value (~850 pA). The experimental threshold (red line in (a)) was used to determine a working distance at which steady-state simulations (b) were carried out to calibrate the normalized SECM current as a function of the uptake rate constant at the surface. The normalized SECM current is the value at d = 120 nm divided by that with the probe in bulk solution (~10 pA). (c) and (d) show the concentration of $[Ru(NH_3)_6]^{3+}$ at steady state with initial concentrations of 10 mM in the SICM barrel and 0 mM in bulk.

2.4.3 Validation of SICM-SECM for Uptake Mapping: As a proof-of-concept system for spatially-resolved uptake mapping, a surface of reasonably high expected uptake (*Zea mays* root hair cells, see optical micrograph in Figure 2.4a) was imaged on a glass substrate (no expected uptake) in 10 mM KCl (pH 6.5). Figures 2.4b and

2.4c show a typical pair of simultaneously collected topography and normalized SECM current maps of a root hair cell on a glass substrate. The height of the cell varies from 7-10 μm, as it is not fully adhered to the surface,[33] and the steep drop off at the edges of the cell suggests a cylindrical morphology, consistent with previous work.[33]

The normalized SECM current map (Figure 2.4c) displays a very clear distinction between the behavior of the SECM channel over the root hair cell and the glass, with a pixel-perfect correlation with the topography map in Figure 2.4b, i.e. at every pixel the SECM response was consistent with the probe approaching the glass or cell (as indicated by topography). As mentioned above (Figure 2.3b), normalized SECM current values greater than 1 mean that the SECM current is higher close to the surface than in bulk. This is always observed over the glass substrate (typical value ~1.25) and is caused by the hindered diffusion/migration of ions away from the end of the probe. A value of normalized SECM current lower than 1.25 corresponds to uptake by the sample. The values across the cell are similar, with an average value of 0.91 ± 0.02, suggesting a high uptake rate constant of 0.31 ± 0.03 cm s^{-1} over the cell surface (Figure 2.3b). Individual approach curves of the SECM current taken from the scan in Figure 2.4c are shown in Figure 2.4d, to illustrate the consistency of the measurements in different areas of the cell and different areas of the glass, and the contrasting behaviour in the approach curve between the cell and glass substrate.

A scan of this size has an acquisition time of approximately 30 minutes. Figures 2.4e,f show the change in SICM and SECM currents, respectively, across the entire scan. The ionic current (SICM, Figure 2.4e) drifts from 835 pA to 810 pA, a change of less than 1 pA min^{-1}. This has a negligible effect on SICM topography imaging as a percentage feedback value, compared to bulk, is used. Proportionally, there is a more pronounced drift (deterioration) of the SECM current (Figure 2.4f) with time, from 10 pA to 6 pA. This makes the self-referencing method described above crucial to the reasonable interpretation of the SECM current data. It should be noted that the spikes both above and below the main trend in Figure 2.4f are approaches over glass and the root hair cell respectively; the bulk current is given by the red line.

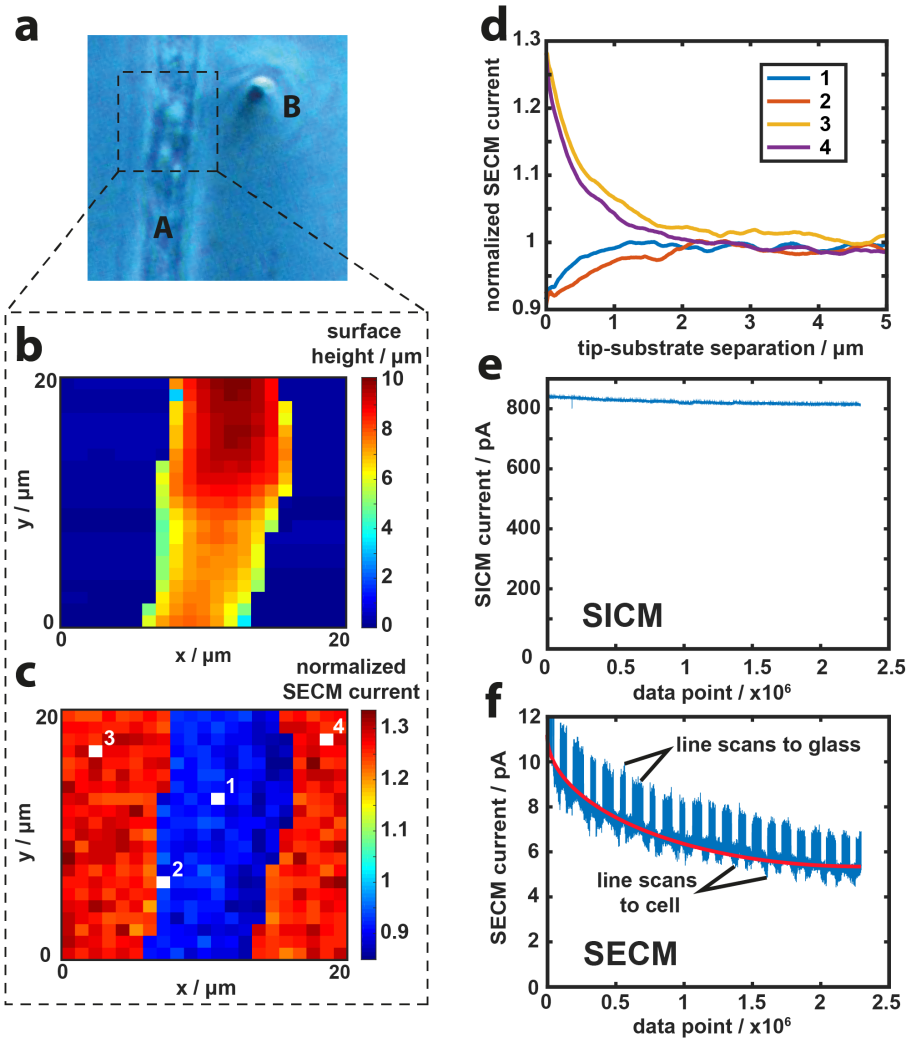

Figure 2.4. SICM-SECM topographical and $[Ru(NH_3)_6]^{3+}$ uptake mapping of a *Zea mays* root hair cell on a glass substrate. (a) Optical image of the scanned root hair cell (A) on a glass support with the end of the probe also visible (B); scan area denoted by the dashed rectangle. (b) Substrate topography extracted from the z-position at the point of closest approach. (c) Normalized SECM current map showing the difference in uptake between glass substrate (zero uptake) and the root hair cell. 'Normalized current' is the ratio of the $[Ru(NH_3)_6]^{3+}$ steady-state limiting reduction current at the point of closest approach to the reduction current in bulk. Individual experimental approach curves from the scan in (c) are shown in (d), at the four positions numbered. SICM (e) and SECM (f) currents across the entirety of the scan (400 separate approach curves) demonstrate minor current drift for SICM, but some effect for SECM, making the self-referencing approach essential. The red line in (f) shows the trend in bulk SECM current, ignoring the approaches to either the cell or the glass.

No interpolation has been applied to the data in Figures 2.4b,c and each pixel represents a quantified measurement of the interfacial uptake rate on the nanoscale. Furthermore, it should be noted that much of the scan time is spent in the probe retracting over a sufficient distance to map out topography of the root hair cell on the glass substrate. Many adherent mammalian cells are less than 1 μm in height and thus the scan could be acquired significantly faster in future experiments. Moreover, faster piezoelectric positioning systems would further reduce the scan time and increase pixel density.

2.4.4 Differentiation of Subcellular Uptake Heterogeneities: While the ability to distinguish between uptake and no uptake was an important validation of the method, the technique was also applied to differentiate between the uptake rates across a single cell. Figure 2.5a shows a single *Zea mays* root hair cell, curved in a hairpin shape (bend outside of the optical micrograph) such that the root hair body and root hair tip could be imaged concurrently. The topography from the scan area denoted by the dashed white box in Figure 2.5a is shown in Figure 2.5b. The two areas of the cell are at different heights above the glass substrate but both suggest the cylindrical shape seen in Figure 2.4.

The normalized SECM current map (Figure 2.5c, response over the background glass slide grayed out to emphasize contrast; see Supporting Information, section 2.6.4 for raw data) shows two clearly defined regions, labelled 'tip' and body' on Figure 2.5b, that have different normalized SECM current value ranges. The body of the cell generally has higher normalized SECM current values (mean = 0.956, standard deviation (s.d.) = 0.033) than at the cell tip (mean = 0.922, s.d. = 0.034), suggesting a faster uptake rate at the root hair tip than at the cell body. This difference between the two regions is emphasized when the data are displayed as a histogram (Figure 2.5d), where the bell-shaped spread of the normalized SECM current values at the tip is shifted from that of the body. The function of the root hair cell is to uptake nutrients that can then be distributed to the rest of the plant[45] and the higher level of uptake at the tip of the cell could potentially be a result either of a higher density of membrane transport proteins, or a generally looser membrane in this region. However, the higher uptake could also be caused by the charge density, arising as a result of charged proteins and lipids at the cell surface. Recent work with

SICM for charge mapping[33] has shown that the tip of a root hair cell carries a significant negative charge when compared to the cell body and this could play an important role in the uptake of the positively charged $[Ru(NH_3)_6]^{3+}$ analyte used.

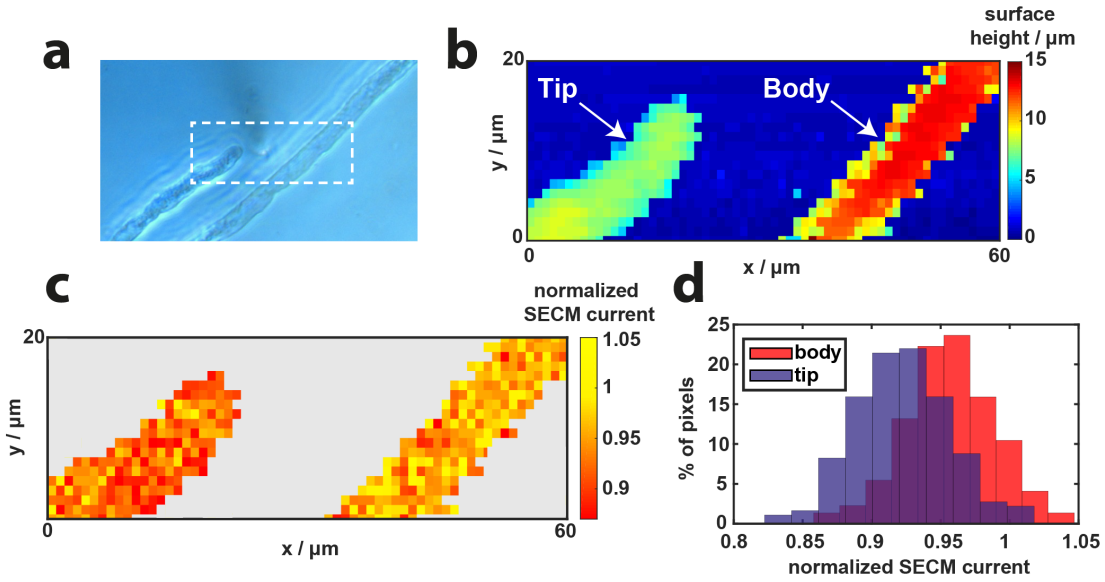

Figure 2.5. SICM-SECM topographical and $[Ru(NH_3)_6]^{3+}$ uptake mapping of two regions of a single *Zea mays* root hair cell. (a) Optical image of the scanned root hair cell; scan area denoted by the dashed rectangle. (b) Substrate topography extracted from the z-position at the point of closest approach from the SICM channel. (c) Normalized SECM current map showing a clear difference in uptake between the root hair cell body (higher current, lower uptake) and the root hair cell tip (lower current, higher uptake). 'Normalized current' is the ratio of the $[Ru(NH_3)_6]^{3+}$ reduction current at the point of closest approach to the same reduction current in bulk. (d) Histograms of the normalized SECM current across the two different regions of the root hair cell, 'tip' and 'body' (see (b)).

Despite the difference in overall uptake rates between the two regions, there is a spread of uptake values that can be attributed to several factors. First, heterogeneities in protein or charge lipid distribution on the cell surface would cause a distribution of uptake rates (normalized SECM current). A second reason is that the SECM currents measured during the experiment are rather small (~10 pA) and thus there will be a natural variation as a result of electrical noise. With these limitations in mind, it is possible to quantify the normalized SECM current values

measured at both the tip and the body using the simulated calibration curve (Figure 2.3b). The mean values stated above correspond to an uptake rate of 0.27 ± 0.05 cm s^{-1} for the cell tip and 0.22 ± 0.05 cm s^{-1} for the cell body. The ability to distinguish between two regions with similar uptake rates suggests this technique has great promise going forward.

2.5 Conclusions

We have demonstrated the use of dual-barrel SICM-SECM nanoprobes to simultaneously measure the topography and spatially-resolve the uptake rate of a molecule of interest delivered from the probe across an interface. As a proof of concept, the uptake of hexaammineruthenium(III) to *Zea mays* root hair cells was studied, highlighting heterogeneities in uptake rate across a single cell, with a slightly higher rate of analyte uptake at the cell tip than at the cell body based on the probe current response. These qualitative differences were then quantified using FEM simulations of the experimental setup to provide a powerful platform for mapping and quantifying the uptake rate of electroactive species across an interface. A key feature of the approach has been pixel-level self-referencing of both the SICM and SECM response at each point in a map to overcome any drift in the response of the two channels.

This new technique could aid the screening of drug molecules; for example, using this assay in tandem with cytotoxicity experiments to inform the user of the efficacy of the drug once it had crossed the cell membrane. The technique could also be used to study electrocatalysis and other materials reactivity problems. This work adds significant new functionality to the family of scanning electrochemical probe techniques and could be combined with laser-scanning confocal microscopy and other microscopies to investigate a wide range of processes, from biological (living) systems to materials and catalysis.

2.6 Supporting Information

2.6.1 FEM Simulations: FEM simulations were constructed and run in COMSOL 5.2 as outlined in the manuscript. A 3D axisymmetric domain of the nanopipette with dimensions extracted from TEM images was constructed, a schematic 2D slice of which is depicted in Figure 2.6 below, with boundary conditions in Table 2.2. All

boundaries that are not specifically labeled with conditions are set as no flux boundaries with [KCl] = 10 mM. No potential is applied at boundary B1 as the electric field from the probe does not appreciably intercept the surface and any electric boundary condition applied at B1 would necessarily be conjecture. No potential is applied at boundary B4 as the electric field from the electrode will have a negligible effect and was thus not included to reduce the complexity of the simulation. The system of differential equations solved was as follows. Ionic transport is reasonably assumed to follow the classical Nernst-Planck relationship, where the flux J_i of species i is given as:

$$J_i = -D_i \nabla c_i - z_i \frac{F}{RT} D_i c_i \nabla \phi \tag{2.2}$$

and the Poisson equation describes the electrical potential ϕ:

$$\nabla^2 \phi = -\frac{F}{\varepsilon \varepsilon_0} \sum_i z_i c_i \tag{2.3}$$

where c_i denotes the concentration of species i, while D_i, z_i, F, R, T, ε and ε_0 specify constants: diffusion coefficient of i, its charge number, the Faraday constant, gas constant, temperature, relative permittivity and vacuum permittivity, respectively.

The initial conditions in the SICM barrel were 10 mM KCl and 10 mM hexaammineruthenium(III) chloride while the initial conditions in bulk solution were 10 mM KCl. A concentration of 0 mM $[Ru(NH_3)_6]^{3+}$ was set as the boundary condition at the end of the SECM barrel (diffusion-limited detection) and the flux was monitored and converted into current. There was no treatment of $[Ru(NH_3)_6]^{2+}$; it is generated in small amounts and is not expected to affect the flux of $[Ru(NH_3)_6]^{3+}$ across the cell membrane. However, the generated species in SECM could sometimes affect the flux of other species, and for a system where this is the case this could readily be treated.

Simulations were first performed to find the point of closest approach from the SICM feedback with a tip potential of +0.2 V. The threshold value used experimentally was a drop in current of 1.5 % compared to the bulk value. Steady-state simulations were carried out at a variety of probe-substrate separations to build an approach curve, from which a separation of 120 nm was determined for this set

point (see Figure 2.3a). Having determined the working distance, a series of steady-state simulations were carried out at this probe-substrate separation with surfaces of differing uptake rate constant, k, ranging from 0 cm s^{-1} to 1000 cm s^{-1}. Throughout these simulations the SICM bias of +0.2 V was still applied to mimic the experimental setup.

Table 2.1. Diffusion coefficients of the species simulated.

Species	D_i, $\times 10^{-5}$ cm^2 s^{-1}
K^+	1.96
Cl^-	2.05
$[Ru(NH_3)_6]^{3+}$	0.96

Table 2.2. Boundary conditions for the FEM model with boundaries corresponding to Figure 2.6 below.

Boundary	Concentration/Flux	Potential
B1	$flux = -k[Ru(NH_3)_6]^{3+}$	No electric boundary condition applied
B2	[KCl] = 10 mM	V = 0 V
B3	[KCl] = 10 mM, $[Ru(NH_3)_6Cl_3]$ = 10 mM	V = + 0.2 V
B4	$[Ru(NH_3)_6]^{3+}$ = 0 mM	No electric boundary condition applied

Surface charge was not included in the simulations herein. While interesting phenomena have been demonstrated as a result of surface charge on a nanopipette/glass substrate,[42] these phenomena are shown to be manifest with significantly smaller probes, and at closer probe-substrate separations than those used herein. However, if future experiments required smaller probe-substrate separations then the effect of surface charge could be incorporated into the simulations. Relatedly, these simulations were carried out in the absence of electroosmotic flow (EOF), as such effects are expected to be negligible under the conditions of the experiments herein,[46] and the self-referencing technique would compensate for the additional flux. The effects of EOF may be different between

surface and bulk at very small probe-substrate separations and thus it would be possible to include EOF should this be necessary.[47]

The justification for carrying out steady-state as opposed to time-dependent simulations for the quantification of uptake rate is given in section 2.6.2 below, while the justification of the determination of the probe-substrate separation is discussed in section 2.6.3.

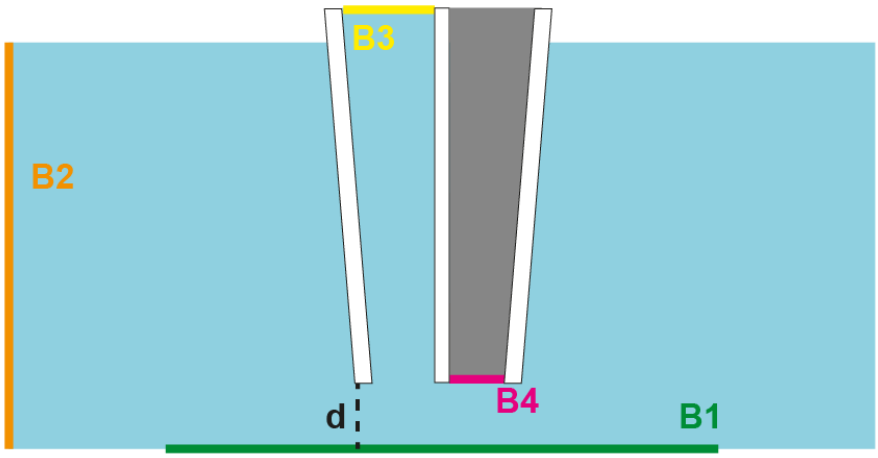

Figure 2.6. Schematic (not to scale) of a 2D slice from the 3D FEM simulation of a dual-channel nanopipette above a surface of variable uptake rate constant, *k*. Boundary conditions at B1-4 in Table 2.2 above.

2.6.2 Justification of Tip-Substrate Separation: The determination of the probe-substrate separation of 120 nm was reached via a simulated approach curve over a surface of no uptake. That separation distance was then used for the steady-state simulations to calibrate the normalized SECM current with a range of uptake rate constants. The SICM current from those steady-state simulations is considered here to determine the influence of uptake rate constant on the SICM approach feedback. Shown below (Figure 2.7) is the percentage difference in SICM current of the simulations over surfaces of various uptake rate constants (at a probe-separation of 120 nm) when compared to the simulation used to determine the separation distance (surface with an uptake rate constant of zero). It can be seen that for the uptake rate constants encountered in this study (~0.25 cm s^{-1}) the effect on the SICM current is about 0.5%, and similar to the noise level in the SICM current (see Figure 2.4e in the main text), thus justifying the method used. However, for interfaces with a higher

uptake rate constant the effect of the uptake on the SICM feedback would need to be considered. This would not be problematic, but would require analysis of the SICM and SECM data simultaneously (and iteratively) to determine both the approach distance and uptake rate.

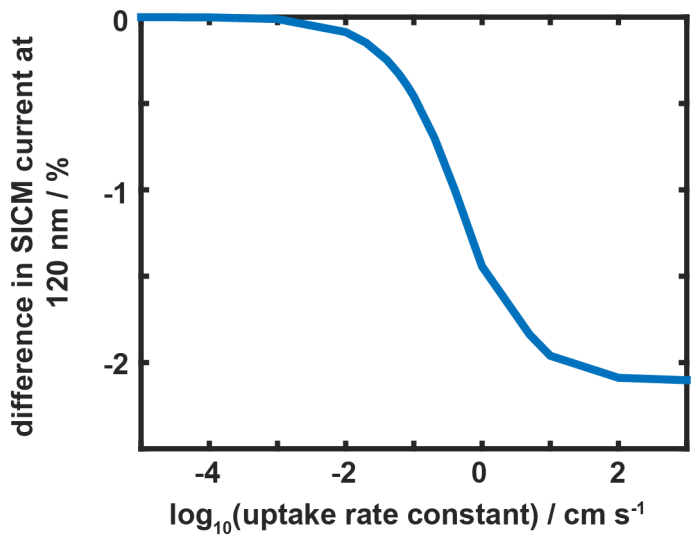

Figure 2.7. Difference in the simulated SICM current at a probe-substrate separation distance (*d*, see above) of 120 nm over substrates of differing uptake rates when compared to the SICM current at 120 nm over a surface with an uptake rate constant of 0 cm s^{-1}.

In order to further justify the probe-substrate separation distance used herein, we now consider the agreement of the theoretical approach curve with a typical experimental approach curve. Figure 2.8 shows the two approach curves in both the SICM channel (a, over a range of 500 nm) and the SECM channel (b, over a range of 1000 nm). Both sets of curves show a strong agreement across the entire range, thus fully validating the method presented herein. It should be noted in both figures that the probe-substrate separation is that taken from the model. Clearly, for an experimental approach the point of closest approach is some way from the surface and thus a shift of 120 nm was applied to the raw experimental data to more easily compare the full approach.

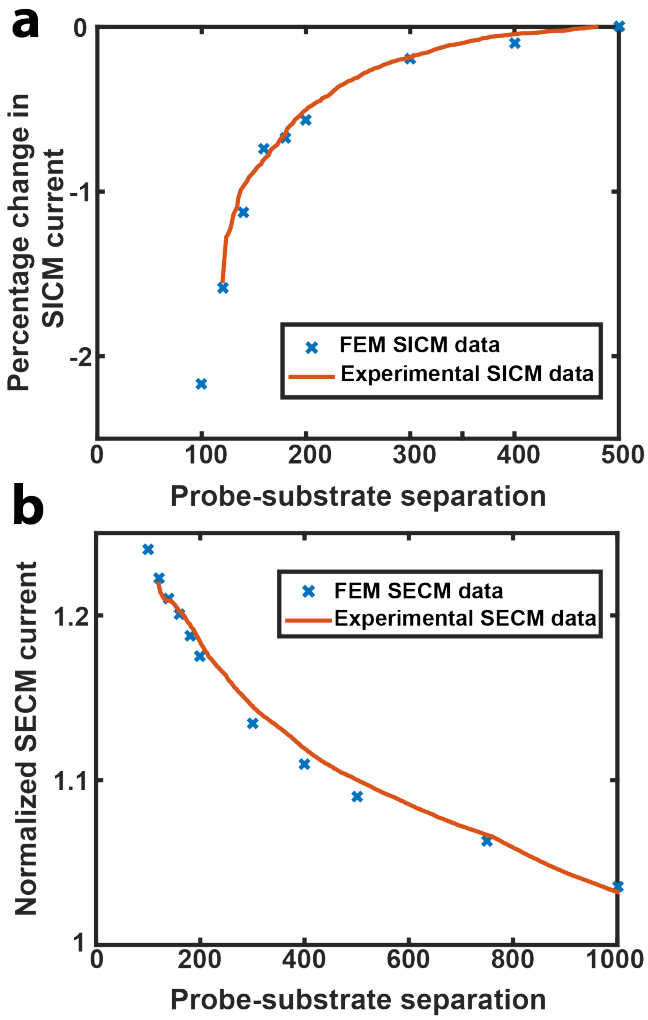

Figure 2.8. Comparison between approach curves in both the SICM (a) and SECM (b) channels from FEM simulations and from a typical experimental approach. In both figures the zero point is that taken from the simulations where the probe-substrate separation is known precisely. The experimental approach curves have been shifted by 120 nm from the point of closest approach.

2.6.3 Approach Data Justifying Steady-State Simulations: As the probe approaches the surface it only remains at the point of closest approach for a short period of time (~1 ms), the period of time during which the current reading used to calculate the normalized current at that pixel is collected. In order to ensure that the approach rate to the surface did not influence the response of the probe (and thus justifying the use of steady-state simulations for quantification) a series of approaches were performed at different approach rates to a cell surface, the results of which are shown in Table 2.3. It can be seen that the normalized SECM current at

the distance of closest approach does not change at approach velocities up to 10 µm s^{-1}, comfortably justifying an experimental approach rate of 2-3 µm s^{-1}. Above 10 µm s^{-1} it becomes questionable as to whether or not the system is at steady state as the normalized current values increase.

Table 2.3. Normalized SECM current values at the distance of closest approach from a series of approach curves to a *Zea mays* root hair cell at different approach rates. Each value given is the mean of three approaches and an error of one standard deviation is also given.

Approach Speed / µm s^{-1}	Normalized Current
0.5	0.91 ± 0.006
1	0.91 ± 0.008
2	0.90 ± 0.011
5	0.90 ± 0.009
10	0.91 ± 0.010
15	0.93 ± 0.011
20	0.94 ± 0.014

2.6.4 Raw Normalized SECM Current Data for Second Scan: The color bar on the normalized current map of Figure 2.5 was optimized to emphasize the difference between the two regions of the cell and, as such, the values for the glass substrate were grayed out. Presented here is the raw data of the entire scan.

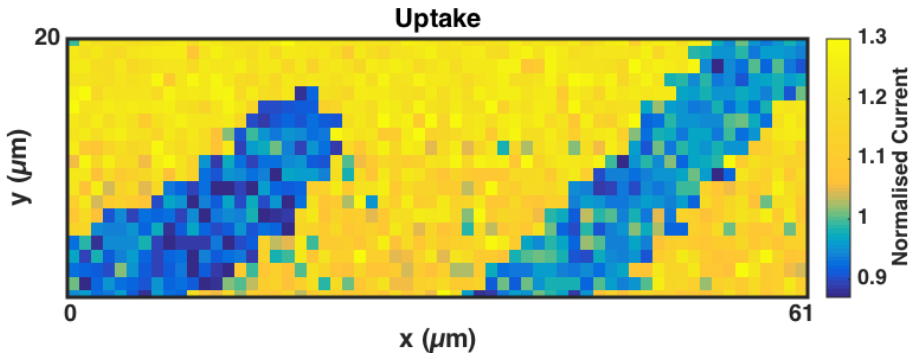

Figure 2.9. Raw normalized current image of the root hair cell scan presented in Figure 2.5.

2.7 References

(1) Alberts, B.; Johnson, A.; Lewis, J.; Morgan, D.; Raff, M.; Roberts, K.; Walter, P. *Molecular Biology of the Cell*; Garland Science, 2014.

(2) Lobritz, M. A.; Belenky, P.; Porter, C. B. M.; Gutierrez, A.; Yang, J. H.; Schwarz, E. G.; Dwyer, D. J.; Khalil, A. S.; Collins, J. J. *Proc. Natl. Acad. Sci. U. S. A.* **2015**, *112* (27), 8173–8180.

(3) Wikström, M.; Sharma, V.; Kaila, V. R. I.; Hosler, J. P.; Hummer, G. *Chem. Rev.* **2015**, *115* (5), 2196–2221.

(4) Hunter, C. A.; Jones, S. A. *Nat. Immunol.* **2015**, *16* (5), 448–457.

(5) Calatayud, M. P.; Sanz, B.; Raffa, V.; Riggio, C.; Ibarra, M. R.; Goya, G. F. *Biomaterials* **2014**, *35* (24), 6389–6399.

(6) Zhou, J.; Li, D.; Su, C.; Wen, H.; Du, Q.; Liang, D. *Phys. Chem. Chem. Phys.* **2015**, *17* (14), 8653–8659.

(7) Cho, E. C.; Zhang, Q.; Xia, Y. *Nat. Nanotechnol.* **2011**, *6* (6), 385–391.

(8) Hasegawa, P. M. *Environ. Exp. Bot.* **2013**, *92*, 19–31.

(9) Stein, W. D.; Litman, T. *Channels, carriers, and pumps: an introduction to membrane transport*; Elsevier, 2014.

(10) Grewer, C.; Gameiro, A.; Mager, T.; Fendler, K. *Annu. Rev. Biophys.* **2013**, *42*, 95–120.

(11) Passarelli, M. K.; Newman, C. F.; Marshall, P. S.; West, A.; Gilmore, I. S.; Bunch, J.; Alexander, M. R.; Dollery, C. T. *Anal. Chem.* **2015**, *87* (13), 6696–6702.

(12) Rezgui, R.; Blumer, K.; Yeoh-Tan, G.; Trexler, A. J.; Magzoub, M. *Biochim. Biophys. Acta, Biomembr.* **2016**, *1858* (7), 1499–1506.

(13) Wang, T.; Bai, J.; Jiang, X.; Nienhaus, G. U. *ACS Nano* **2012**, *6* (2), 1251–1259.

(14) Tsang, C. N.; Ho, K. S.; Sun, H.; Chan, W. T. *J. Am. Chem. Soc.* **2011**, *133* (19), 7355–7357.

(15) Kang, M.; Momotenko, D.; Page, A.; Perry, D.; Unwin, P. R. *Langmuir* **2016**, *32*, 7993–8008.

(16) Kwak, J.; Bard, A. J. *Anal. Chem.* **1989**, *61*, 1794–1799.

(17) Hansma, P. K.; Drake, B.; Marti, O.; Gould, S. A.; Prater, C. B. *Science* **1989**, *243*, 641–643.

(18) Shevchuk, A. I.; Frolenkov, G. I.; Sanchez, D.; James, P. S.; Freedman, N.; Lab, M. J.; Jones, R.; Klenerman, D.; Korchev, Y. E. *Angew. Chem., Int. Ed.* **2006**, *45* (14), 2212–2216.

(19) Happel, P.; Thatenhorst, D.; Dietzel, I. D. *Sensors* **2012**, *12* (11), 14983–15008.

(20) Bergner, S.; Vatsyayan, P.; Matysik, F. *Anal. Chim. Acta* **2013**, *775*, 1–13.

(21) Schulte, A.; Nebel, M.; Schuhmann, W. *Annu. Rev. Anal. Chem.* **2010**, *3*, 299–318.

(22) Filice, F. P.; Li, M. S. M.; Ding, Z. *Anal. Chim. Acta* **2016**, *908*, 85–94.

(23) Bondarenko, A.; Lin, T.-E.; Stupar, P.; Lesch, A.; Cortes-Salazar, F.; Girault, H. H.; Pick, H. M. *Anal. Chem.* **2016**, *88* (23), 11436–11443.

(24) Gonsalves, M.; Barker, A. L.; Macpherson, J. V; Unwin, P. R.; Hare, D. O.; Winlove, C. P. *Biophys. J.* **2000**, *78*, 1578–1588.

(25) Armstrong-James, M.; Millar, J.; Kruk, Z. L. *Nature* **1980**, *288*, 181–183.

(26) Herr, N. R.; Kile, B. M.; Carelli, R. M.; Wightman, R. M. *Anal. Chem.* **2008**, *80* (22), 8635–8641.

(27) Comstock, D. J.; Elam, J. W.; Pellin, M. J.; Hersam, M. C. *Anal. Chem.* **2010**, *82* (4), 1270–1276.

(28) Takahashi, Y.; Shevchuk, A. I.; Novak, P.; Murakami, Y.; Shiku, H.; Korchev, Y. E.; Matsue, T. *J. Am. Chem. Soc.* **2010**, *132* (29), 10118–10126.

(29) O'Connell, M. A.; Wain, A. J. *Anal. Chem.* **2014**, *86* (24), 12100–12107.

(30) Morris, C. A.; Chen, C.-C.; Baker, L. A. *Analyst* **2012**, *137* (13), 2933–2938.

(31) Takahashi, Y.; Shevchuk, A. I.; Novak, P.; Zhang, Y.; Ebejer, N.; Macpherson, J. V.; Unwin, P. R.; Pollard, A. J.; Roy, D.; Clifford, C. A.; Shiku, H.; Matsue, T.; Klenerman, D.; Korchev, Y. E. *Angew. Chem., Int. Ed.* **2011**, *50* (41), 9638–9642.

(32) O'Connell, M. A.; Lewis, J. R.; Wain, A. J. *Chem. Commun.* **2015**, *51* (51), 10314–10317.

(33) Perry, D.; Paulose Nadappuram, B.; Momotenko, D.; Voyias, P. D.; Page, A.; Tripathi, G.; Frenguelli, B. G.; Unwin, P. R. *J. Am. Chem. Soc.* **2016**, *138* (9), 3152–3160.

(34) Nadappuram, B. P.; McKelvey, K.; Al Botros, R.; Colburn, A. W.; Unwin, P. R. *Anal. Chem.* **2013**, *85* (17), 8070–8074.

(35) Ebejer, N.; Güell, A. G.; Lai, S. C. S.; McKelvey, K.; Snowden, M. E.; Unwin, P. R. *Annu. Rev. Anal. Chem.* **2013**, *6*, 329–351.

(36) Güell, A. G.; Cuharuc, A. S.; Kim, Y. R.; Zhang, G.; Tan, S. Y.; Ebejer, N.; Unwin, P. R. *ACS Nano* **2015**, *9* (4), 3558–3571.

(37) Takahashi, Y.; Murakami, Y.; Nagamine, K.; Shiku, H.; Aoyagi, S.; Yasukawa, T.; Kanzaki, M.; Matsue, T. *Phys. Chem. Chem. Phys.* **2010**, *12* (34), 10012–10017.

(38) Perry, D.; Momotenko, D.; Lazenby, R. A.; Kang, M.; Unwin, P. R. *Anal. Chem.* **2016**, *88* (10), 5523–5530.

(39) Chen, C.-C.; Zhou, Y.; Baker, L. A. *Annu. Rev. Anal. Chem.* **2012**, *5* (1), 207–228.

(40) Edwards, M. A.; Williams, C. G.; Whitworth, A. L.; Unwin, P. R. *Anal. Chem.* **2009**, *81* (11), 4482–4492.

(41) Sa, N.; Baker, L. A. *J. Am. Chem. Soc.* **2011**, *133* (27), 10398–10401.

(42) Sa, N.; Lan, W. J.; Shi, W.; Baker, L. A. *ACS Nano* **2013**, *7* (12), 11272–11282.

(43) Perry, D.; Al Botros, R.; Momotenko, D.; Kinnear, S. L.; Unwin, P. R. *ACS Nano* **2015**, *9* (7), 7266–7276.

(44) Chen, C.-C.; Baker, L. A. *Analyst* **2011**, *136* (1), 90–97.

(45) Foster, K. J.; Miklavcic, S. J. *Front. Plant Sci.* **2016**, *7*, 914.

(46) McKelvey, K.; Kinnear, S. L.; Perry, D.; Momotenko, D.; Unwin, P. R. *J. Am. Chem. Soc.* **2014**, *136* (39), 13735–13744.

(47) Luo, L.; Holden, D. A.; White, H. S. *ACS Nano* **2014**, *8* (3), 3023–3030.

3 Fast Nanoscale Surface Charge Mapping with Pulsed-Potential Scanning Ion Conductance Microscopy

As an alternative approach to the dual-channel probe used in Chapter 2, this chapter focuses on the development of the single-channel nanopipette as a multifunctional tool, in this case simultaneously mapping the substrate topography and surface charge. While this technique had been introduced previously, the potential-control regime used to extract charge data led to long scan times and low pixel acquisition rates. In this study, both the potential-control function (for charge mapping) and the feedback type (for topographical mapping) are optimised to improve the pixel acquisition rate by an order of magnitude over the previous regime. This advancement is demonstrated via the collection of high-resolution maps of both polymeric and cellular substrates, with FEM simulations in tandem to quantify the charge density on the surface.

This chapter was published as a technical note in *Analytical Chemistry*. Experiments were performed by the author together with Dr. David Perry, who also carried out the FEM simulations after they had been jointly discussed. Cell culturing was also performed together, with advice and training from Dr. Philip Young. The manuscript was written by the author.

Fast Nanoscale Surface Charge Mapping with Pulsed-Potential Scanning Ion Conductance Microscopy

Ashley Page,[1,2,†] David Perry,[1,2,†] Philip Young[3], Daniel Mitchell[4], Bruno G. Frenguelli[3] and Patrick R. Unwin[1,]*

[1]Department of Chemistry, [2]MOAC Doctoral Training Centre, [3]School of Life Sciences and [4]Warwick Medical School, University of Warwick, Coventry, CV4 7AL, United Kingdom.

†These authors contributed equally to this work

*corresponding author

p.r.unwin@warwick.ac.uk

3.1 Abstract

A vast range of interfacial systems exhibit charge heterogeneities on the nanoscale. These differences in local surface charge density are challenging to visualize, but recent work has shown the scanning ion conductance microscope (SICM) to be a very promising tool to spatially resolve and map surface charge and topography via a hopping potential sweep technique with a single nanopipette probe, with harmonic modulation of a bias applied between quasi-reference counter electrodes in the nanopipette and bulk solution, coupled with lock-in detection. Although powerful, this is a relatively slow process, with limitations on resolution and the size of the images that can be collected. Herein, we demonstrate a new scanning routine for mapping surface charge and topography with SICM, which increases the data acquisition rate by an order of magnitude, and with the potential for further gains. Furthermore, the method is simplified, eliminating the need for bias modulation lock-in detection, by utilizing a potential-pulse, chronoamperometric approach, with self-referencing calibration of the response at each pixel in the image. We demonstrate the application of this new method to both a model substrate and living PC12 cells under physiological (high ionic strength) conditions, where charge mapping is most challenging (small Debye length). This work contributes significantly to the emergence of SICM as a multifunctional technique for simultaneously probing interfacial structure and function with nanometer resolution.

3.2 Introduction

Scanning ion conductance microscopy (SICM) is a powerful technique for nanoscale non-contact imaging of surface topography[1–3] that finds particular application in the study of cellular systems,[4–8] where resolution has been extended to the individual protein level[9] and is comparable to atomic force microscopy (AFM).[10] SICM utilizes a nanopipette filled with electrolyte to probe an interface that is also bathed in electrolyte. A bias is applied between a quasi-reference counter electrode (QRCE) in the nanopipette and one in bulk solution to generate an ionic current. Changes in the ionic current as the nanopipette approaches the substrate can be used to sense, and provide information, about the interface.

Recent developments have taken SICM beyond topography and shown that the current response may be inherently sensitive to other interfacial properties, most notably surface charge heterogeneities[11–13] and surface reactions.[14] Local changes in ionic conductivity near an interface affect the SICM current and can thus be mapped and analyzed, for example, with finite element method (FEM) modeling.[15–17] All of these applications require careful consideration of the scanning routine used, particularly the applied potential bias, so that SICM provides unambiguous information on surface properties.

However, it has been shown that without careful experimental design, the topographical and surface charge data obtained with SICM can become convoluted, affecting the accuracy of these studies. To address this issue, surface charge mapping with SICM has been performed in a bias modulated (BM-) SICM[18] format that enables topography and surface charge to be resolved simultaneously without convolution.[12] In this regime the nanopipette is approached to the surface or interface of interest, with no net (time averaged) bias applied between the two QRCEs, just a small harmonic oscillation of the bias around 0 V. Importantly, this renders the SICM response relatively insensitive to surface charge, so that topography is mapped. Upon detection of the substrate (usually by a change of the current phase), the bias is then swept between two extreme values and the SICM response becomes sensitive to surface charge. The surface charge is elucidated by comparing the voltammogram near the surface to one performed in bulk at each and every pixel in a self-referencing regime.

In this contribution, we introduce a new regime that significantly advances SICM topography-charge mapping, increasing the pixel acquisition rate by an order of magnitude (with scope for further gains), thereby allowing for imaging with a much higher pixel density. The method eliminates the modulation of the bias and replaces this with a minimal fixed bias that permits faster approach speeds for topographical imaging, while a pulse in the bias at the point of closest approach, as opposed to a voltammogram, allows faster acquisition of surface charge information. Voltage-switching has proved useful in the related technique of scanning electrochemical microscopy (SECM), for topography and activity imaging with a single solid nanoelectrode probe, but requires the use of two redox mediators in solution which may be somewhat restrictive.[19] FEM simulations allow for the quantification of the experimental data and show no loss of accuracy when compared to the previous potential-scanning regime.[12] The increase in pixel density afforded by this new approach reveals previously unseen charge heterogeneities in two substrates: an interrupted polystyrene film in high electrolyte concentration; and a neuron-like PC12 cell imaged in cell culture media. Thus, the reliable increase of the scanning speed improves the viability of SICM as a multifunctional technique for surface charge mapping on the nanoscale, and offers new control functions that could be applied to other SICM methods.

3.3 Materials and Methods

3.3.1 Solutions: Milli-Q reagent grade water (resistivity ca. 18.2 MΩ cm at 25°C) was used for all solutions. 50 mM KCl (Sigma-Aldrich) was used for the SICM charge maps of the interrupted polystyrene film on glass. PC12 cells were cultured and imaged in RPMI 1640 media containing 15% horse serum, 2.5% foetal calf serum, 5 mM glutamine, 100 U/mL penicillin and 100 μg/mL streptomycin (all Sigma Aldrich).

3.3.2 Nanopipettes and Electrodes: Nanopipettes were pulled from borosilicate glass capillaries (o.d. 1.2 mm, i.d. 0.69 mm, Harvard Apparatus) using a laser puller (P-2000, Sutter Instruments; pulling parameters: Line 1: Heat 330, Fil 3, Vel 30, Del 220, Pul -; Line 2: Heat 330, Fil 3, Vel 40, Del 180, Pul 120). The inner radius of the probe was measured using a JEOL 2000FX transmission electron microscope (TEM)

to be 80 nm ± 15 nm (see Supporting Information, Table 3.1 for experimental geometries of the two probes used). Two Ag/AgCl electrodes were used, one in the nanopipette and a second in bulk solution.

3.3.3 Substrates: Glass-bottomed Petri dishes with detachable coverslips (3512, WillcoWells) were used for both substrates. In the case of the polystyrene, the glass bottom of the dish was dip-coated in a solution of polystyrene dissolved in chloroform (1 mg/mL) to ensure a heterogeneous substrate. The PC12 cells used were adherent to glass-bottomed petri dishes and so these were used as a support.

3.3.4 Cell Culturing Procedure: Adherent PC12 cells (ATCC-CRL-1721.1) were cultured in tissue culture flasks in the above-specified media until confluent, before trypsinization and transfer to Petri dishes. They were allowed 72 hours to adhere to the glass substrate before imaging in fresh media.

3.3.5 Instrumentation: The basic instrumentation setup has been described in detail previously.[12,20] Briefly, the lateral movement of the probe was controlled using a two-axis piezoelectric positioning system with a range of 300 μm (Nano-BioS300, Mad City Labs, Inc.), while movement normal to the substrate was controlled using a more precise piezoelectric positioning stage of range 38 μm (P-753-3CD, Physik Intrumente). The electrometer and current-voltage converter used were both made in-house, while user control of probe position, voltage output and data collection was via custom made programs in LabVIEW (2013, National Instruments) through an FPGA card (7852R, National Instruments).

3.3.6 Fast Charge Mapping SICM: All images presented herein were collected using a self-referencing scan hopping mode of SICM, with the regime for each pixel as follows (Figure 3.1a): (I) First, the probe was translated towards the surface at 6 μm/s with the QRCE in the probe biased at +20 mV vs. the QRCE in bulk. When the ionic current between the two electrodes had reduced by a chosen threshold value (giving a precise working distance, as calculated from FEM simulations, see below), the probe motion was halted before (II) a 50 ms pulse of the probe potential to -400 mV. After this pulse (III) the probe potential was returned to +20 mV and the probe

was retracted either 1 μm or 2 μm for the polystyrene or PC12 cell samples, respectively (retract distance dependent on the height variation of the substrate, but sufficient to represent bulk solution as it was always well over 5 times the dimensions of the nanopipette opening)[1] at 10 μm/s before (IV) a second 50 ms pulse in the bulk solution and (V) the probe was then moved to the next pixel. The current was monitored during the entire process at a rate of 2 kHz and the current-time (*I-t*) curve at the surface and the *I-t* curve in bulk were compared to extract surface charge information at each pixel.

3.3.7 FEM Simulations: A 2D axisymmetric model of the nanopipette in bulk solution and near a substrate was constructed in COMSOL Multiphysics (v. 5.2) with the Transport of Diluted Species and Electrostatics modules. A schematic of the simulation domain and boundary conditions is presented in Supporting Information (Figure 3.5). The dimensions of the nanopipettes were extracted from TEM images of nanopipettes.[21,22]

To obtain working distances for experimental SICM measurements, simulations were performed at varying probe-substrate separation with an applied probe bias of 20 mV (the experimental approach bias). Once the working distance, corresponding to the experimental feedback threshold was known, time-dependent simulations were performed at this separation distance with varying surface charge applied to the domain boundary below the nanopipette. Simulations were also performed with the nanopipette positioned in bulk solution and the near-surface values of the ionic current, with different applied surface charge, were normalized to those in bulk to elucidate surface charge from experimental maps. For all of these simulations the initial conditions used were obtained from steady-state simulations performed with the same conditions except the tip bias was 20 mV (the approach bias).

3.4 Results and Discussion

3.4.1 Scanning Regime for Interfacial Charge Mapping: Previous work on SICM showed that the charge at an interface, particularly in low ionic strength electrolyte concentrations (<10 mM aqueous solution), can have a significant effect on the current response during the approach of the nanopipette probe towards a substrate

surface.[11,12,23–25] This convolution of charge and topography becomes more significant as the potential difference between the two QRCEs is increased.[12] To overcome this problem, our previous work utilized a BM-SICM regime, which allowed topographical information to be extracted with no net bias and just a small harmonic perturbation, followed by the application of a linear scan of potential at each pixel to reveal the charge. However, the use of modulation-based SICM constrains the approach speed of the probe, depending on the time constant of the lock-in amplifier used and modulation frequency employed.[18] Herein, we make use of a direct current (DC) feedback mode to generate a feedback signal for essentially *charge-insensitive topographical mapping*.

In this setup, a small bias (+20 mV at the probe electrode with respect to the QRCE in bulk solution) is applied to produce the ionic current for DC feedback (topographical mapping). It was possible to apply such a small bias, which generated a reasonable current magnitude, because the experiments were carried out in physiologically-relevant media, which has high ionic strength, and will be most relevant for future work, e.g. for cell imaging. The choice of approach bias in these measurements is important and requires a theoretical consideration. The bias chosen will depend on the ionic strength of the imaging media and the size of the nanopipette, as well as the range of surface charges that are to be probed. The bias needs to be chosen such that it provides a robust feedback signal for tracking topography experimentally, but simulations (such as those reported herein) are also required to justify that under the imaging conditions, the surface charge of the substrate does not influence the nanopipette response. Upon approach to within a probe diameter of the substrate of interest, a decrease of the ionic current between the two QRCEs occurs[2] which is attributed to the increased access resistance near the nanopipette opening. This approach comfortably allows the mapping of topography at approach speeds of 5 μm/s and above (maximum not tested). The small applied bias, as discussed below, meant that there was little convolution of the topography and charge at the interface in relatively high electrolyte concentrations (≥50 mM), and the current response allowed for accurate topographical mapping (see below).

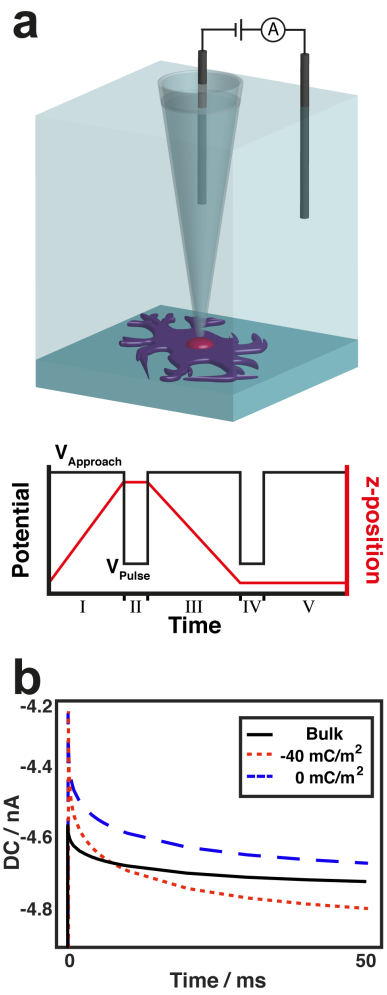

Figure 3.1. Setup for a high-speed charge mapping experiment. (a) Schematic of basic SICM set up used for charge mapping, with a trace of z-position and potential at each hop in the scan hopping regime: (I) probe approaches the surface at $V_{Approach}$ = +20 mV, (II) 50 ms pulse at V_{Pulse} = -400 mV before (III) probe is retracted at +20 mV and (IV) a second pulse to -400 mV in bulk solution. (V) Probe is moved in the x or y direction to the next point. (b) Simulated *I-t* curves of a probe in bulk (black line) and at a 15 nm separation from surfaces of neutral and negative charge (red and blue lines respectively).

As mentioned above, the extraction of interfacial charge information in previous work utilized the measurement of a cyclic voltammogram (CV) at both the surface and in bulk solution, considering the rectification of the current-voltage behavior as a result of the diffuse double layer (EDL) at the tip and surface.[12,23,25] Typically the CV was obtained by sweeping the potential between –400 and +400 mV at a scan rate of 1 V/s - a total of 3.2 s of CV time per pixel (1.6 s at the surface

and 1.6 s in bulk). Despite the wealth of information collected at each pixel in this regime (including potential-resolved current-space movies), surface charge was manifest in the current response mostly at large bias. In fact, in our previous work, the FEM simulations for the quantification of surface charge were only carried out at the extreme potentials of the CV, with an applied potential of -400 mV proving to be the most sensitive to variations in local interfacial charge.[12]

In this work, the time taken to collect interfacial charge information is significantly reduced by pulsing the probe bias from the approach potential (+20 mV) to -400 mV at the point of closest approach, and in bulk, in a self-referencing format (Figure 3.1a). To prove the potential pulse concept, current-time (*I-t*) transients were simulated in 50 mM KCl (Figure 3.1b). For the three simulated *I-t* curves shown, the initial conditions were obtained by first performing a steady-state simulation at the approach probe potential (+20 mV) before a subsequent time-dependent simulation with an applied bias of -400 mV, with different surface charges applied to the substrate. The simulations at 0 mC/m^2 and -40 mC/m^2 used a probe-substrate separation of 15 nm, which corresponded to the feedback threshold used during experiments, as obtained below. It is clear that the *I-t* response near the surface is different compared to the bulk solution, and that when the probe is near the surface, the charge has a significant influence on the response, validating the use of this new imaging methodology. In these conditions, a negatively charged surface caused an enhancement of the current while a neutral surface caused a diminution, when compared to the bulk response as explained in previous work.[12,25] Further simulations produced working curves of normalized current as a function of surface charge for each of the experimental conditions below. For the present work, 50 ms was taken as length of the experimental potential pulse, with the final few points of the surface *I-t* curve normalized with respect to the final few points of the bulk *I-t* curve at each pixel to produce spatially-resolved surface charge maps. The significant improvements to both the approach speed and interfacial charge collection time reduce the typical pixel acquisition rate for this technique from over 5 s to less than 0.5 s, markedly increasing the efficacy and potential applications of SICM for localized surface charge mapping. Clearly, however, there would be scope for further improvement in the experimental time in the future, since differences in

the *I-t* behavior are apparent on a few ms timescale (Figure 3.1b), and it should be possible to use piezoelectric positioners with a faster response than are used herein.

3.4.2 Validation of the Technique with a Polystyrene Film on Glass: The high-speed approach was first validated experimentally using an incomplete polystyrene film on a glass substrate, such that there were pinholes in the polystyrene layer, exposing the glass below to the solution. The topography from a typical scan, collected in 50 mM KCl with a DC feedback threshold (decrease in current from bulk to the point of closest approach) of 15 pA (~7%), is shown in Figure 3.2a, demonstrating a highly heterogeneous film that varies in thickness from a few tens of nm in some areas to a few hundreds of nm in others. Note that we applied an absolute change in the current, as the bulk current was found to be stable at 210 pA, but in situations where there was a change in the bulk current, a percentage change could easily be applied. Pinholes in the film in which the glass is exposed are of variable size, with some clearly visible and others not resolved as well, as they are the same size or smaller than the probe opening (~150 nm). The resolution of traditional SICM measurements and surface charge measurements is typically observed to be of a similar order of magnitude to the nanopipette dimensions (0.5 r – 1.5 r)[1] where r is the nanopipette opening radius and hence smaller nanopipettes would be required to resolve these features further.

The heterogeneities in the topography of the substrate are reproduced in the normalized current map (Figure 3.2b), obtained from the pulse procedure outlined above. Areas in which there is a large expanse of glass have normalized current values in the range 1.05-1.07 (yellow/white coloring) while areas of thick polystyrene have normalized current values below 1 (dark red/black coloring). Interestingly the intermediate areas of the scan largely have values between these two extremes (red coloring), which can be attributed to pinholes on a scale less than that of the probe diameter. This explanation of the intermediary values of normalized current in those areas of the scan where the film is very thin also explain the wide range of values seen in these regions. If we denote the area of the substrate that affects the current response during the potential pulse as the 'footprint' of the probe, then any value between the 'true glass' value of ~1.06 and the 'true polystyrene' value of ~0.99 could be obtained with differing percentages of glass and polystyrene

in the footprint. A scan collected from a different sample in which the polystyrene is more uniform is presented in the Supporting Information (Figure 3.6) for comparison, which instead mainly shows just two regions of different charge.

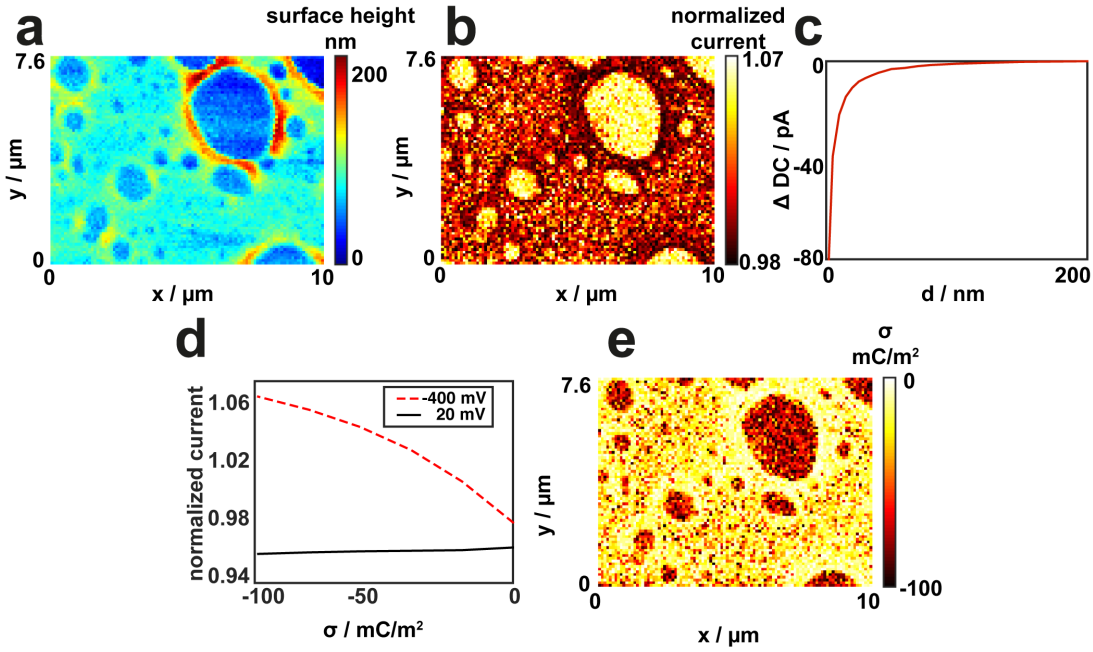

Figure 3.2. Simultaneous topography and quantified charge maps of an incomplete polystyrene film on a glass substrate. (a) Topography image recorded with a ~70 nm radius nanopipette in a hopping regime using DC feedback. (b) Normalized current (surface current divided by bulk current) map collected concurrently with the topography. (c) FEM simulation of the change in DC as the probe approaches the surface, showing dependence of probe-substrate separation on the feedback threshold chosen. (d) Simulated dependence of the normalized current on the charge at the surface, used to generate the quantified charge map in (e).

An approach curve was simulated using the same probe geometry and electrolyte conditions as the experiment (Figure 3.2c) in order to extract the probe-substrate separation when a feedback threshold of 15 pA is used. From the approach curve, this value was found to be 15 nm, a separation that was then used for the time-dependent simulations at surfaces of differing charge density (Figure 3.2d). Note, that further increases in the feedback threshold used could improve the sensitivity to charge heterogeneities. The red curve demonstrates a strong dependence of the normalized current on the surface charge density when the QRCE in the probe is

biased at -400 mV, while at +20 mV (black curve) there is almost no effect of the surface charge on the normalized current, legitimizing the use of this potential during the approach for topographical imaging. The combination of the normalized current map in Figure 3.2b with the calibration curve in Figure 3.2d produced the quantified charge map in Figure 3.2e. Areas in which the polystyrene film is complete have a charge density of 0 mC/m^2, the expected value given the neutrality of the polymer, while glass has a charge of about -60 mC/m^2, comfortably within the range of those values quoted in the literature.[25] Note, that the apparent surface charge in the glass regions is quite heterogeneous, most likely due to the heterogeneous distribution of the polymer film. For example, small patches of polystyrene are likely to be present within the predominantly glass regions. A typical scan collected using the bias modulation and CV approach in previous work is shown for comparison (Supporting Information, Figure 3.7). The range of current values is larger as a lower electrolyte concentration (10 mM) was used, but the local charges are similar. It should be noted that despite containing significantly fewer pixels it took more than twice as long to obtain that image than the main scan presented in Figure 3.2.

3.4.3 Surface Charge Mapping of Neuron-like PC12 Cells: Having validated the use of high-speed charge mapping with SICM on a model substrate, we then investigated whether the technique could also be used in higher ionic strength conditions (~150 mM, RPMI 1640 media, see Materials and Methods for composition) in which the width of the EDL would be significantly reduced.[26] Figure 3.3a shows an optical micrograph of a spontaneously differentiated neuron-like cell from the PC12 cell line, with the scan area, extending from the cell body along the length of a neurite, outlined by the dashed white square.

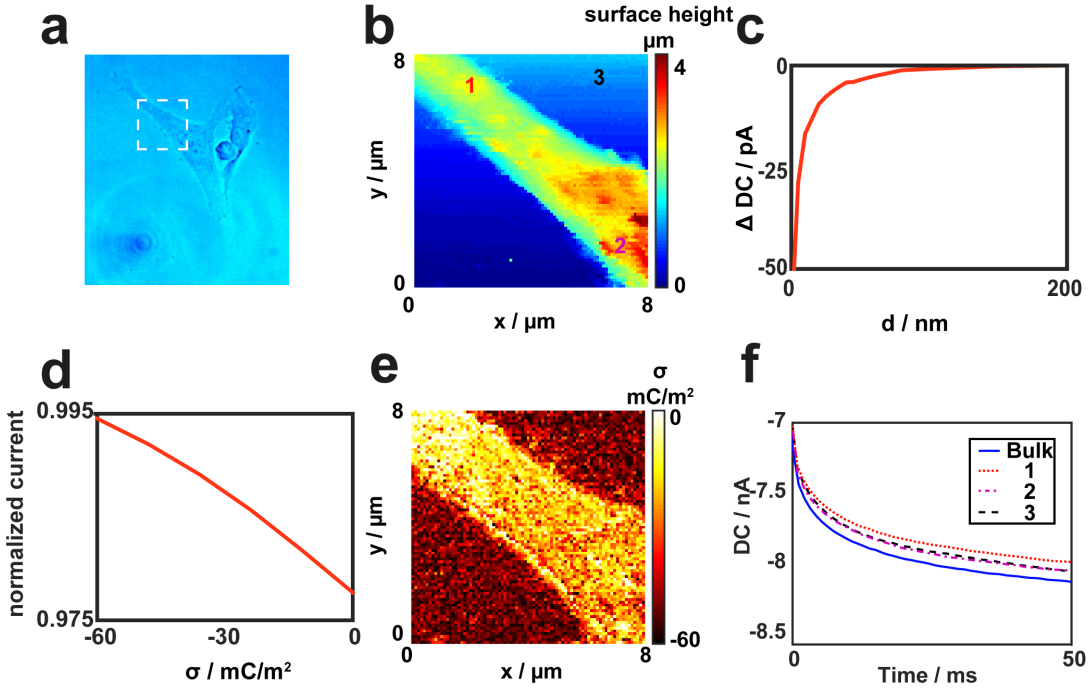

Figure 3.3. Simultaneous topography and charge maps of a PC12 neurite on a glass substrate. (a) Optical image of the scanned cell, the white square showing the scan area. (b) Topographical image of the neurite, collected concurrently with the quantified charge map (e). (c) FEM simulation of the change in DC as the probe approaches the surface at +20 mV, showing dependence of probe-substrate separation on the feedback threshold chosen. (d) Simulated dependence of the normalized current on the charge at the surface, used to generate the quantified charge map in (e). Experimental *I-t* curves at the points of the scan labeled in (b) are shown in (f), along with a bulk *I-t* curve for comparison.

The topographical data (Figure 3.3b), collected with a feedback threshold of 8 pA (~2%) and a working distance of 30 nm (see approach curve, Figure 3.3c), show that the region of the cell imaged varies in height by ~2 µm, with the thickest area at the cell body and the thinnest area towards the furthest extension of the neurite. Patches of increased height, several hundred nanometers in prominence, are seen along the length of the cell. The numbers on Figure 3.3b correspond to the experimental *I-t* curves in Figure 3.3f, and highlight differences in charge between regions of the neurite (1), the cell body (2) and the glass (3). All three of these curves are lower in magnitude than a typical experimental bulk *I-t* curve (shown in blue).

The compression of the range of possible normalized currents arises as a result of the decrease in double layer thickness, meaning the effect of charge density on ionic transport to the probe is diminished. Nonetheless, it is important to note that despite a range of only 1.5% in the normalized current across the entire scan (see Supporting Information, Figure 3.8) the technique is still sensitive enough to quantify the charge density (Figures 3.3d,e).

As would be expected, the glass carries a homogeneous negative charge (~-55 mC/m^2). While this value differs slightly from that obtained from the polystyrene scan above, the two are not directly comparable. As the surface charge of glass relies on the acid-base equilibrium of silanol groups (SiOH) at the interface, the termination of which is dependent on the pH of the solution used. The 50 mM KCl was ~pH 6.2 while the cell media was buffered to pH 7.2, a lesser proportion of the silanol groups would be protonated in the media and thus a higher charge density would be expected. However, a lower surface charge is apparent in Figure 3.2. These small differences in the data for glass between Figures 3.2e and 3.3e are likely attributable to small polystyrene features within the glass region, which cannot be resolved topographically, which would serve to reduce the total surface charge presented in the nanopipette footprint. Additionally, the surface charge of the glass in the PC12 study could be impacted by the presence of other molecules (nutrients, proteins, etc.) in the cell growth (imaging) media, which could adsorb on the glass and alter its surface properties. In contrast to the glass substrate, the charge density of the PC12 cell, though negative in polarity throughout, is highly heterogeneous. There is a gradient from the predominantly more negatively charged cell body (as highly charged as the glass in some areas, see Figure 3.3f *I-t* curve 2) to the end of the less highly charged neurite (Figure 3.3f, *I-t* curve 1), though patches of lower charge also appear along the length of the cell. These heterogeneities could arise as a result of protein or charged-lipid rafts in the cell membrane, and further correlative techniques could probe the cellular function of these charge differences.

3.5 Conclusions

The image quality of interfacial charge mapping using SICM has been greatly improved by using a new tip approach and potential control function which increases the pixel acquisition rate by an order of magnitude, compared to our recently

introduced format. The reduction in the time taken to acquire a single pixel of data was achieved via two separate improvements. First, the approach speed of the probe was increased by changing the type of feedback used when detecting the surface. Second, the time taken to extract charge information in a given hop was reduced to 100 ms when previously it was in excess of 3 s. The resulting increase in image quality allowed the visualization of previously unseen features on the nanoscale, including ~100 nm defects in an interrupted polystyrene film and rafts of different charge at the surface of a neuron-like PC12 cell. It should be noted that these studies present negative to neutral charges, but that the protocol would also be sensitive to positive surface charges, with enhanced sensitivity to such surface charges possible through tuning the pulse bias. It should be noted that these scans were collected using nanopipettes of ~80 nm radius and with a decrease in size of the probes used, the resolution, and thus the power, of this technique could be improved further still. It should be possible to decrease the pulse time to a couple of ms and increase the approach speed with better piezoelectric positioners.

This work contributes to the rise of SICM as a multifunctional technique, in this case allowing surface charge to be mapped with a resolution and image quality approaching that of the topographical mapping for which it is most commonly used.

3.6 Supporting Information

3.6.1 Dimensions of Nanopipettes: Nanopipettes used in SICM experiments, discussed in the manuscript were characterized using transmission electron micrograph (TEM) images to obtain accurate dimensions for the use in FEM simulations. The dimensions extracted for these tips are presented in Table 3.1 with a TEM micrograph of one of the nanopipettes displayed in Figure 3.4.

Table 3.1. Dimensions of nanopipettes used for polystyrene and PC12 scans.

Height (nm)	Polystyrene Experiments		PC12 Experiments	
	Inner Radius (nm)	Outer Radius (nm)	Inner Radius (nm)	Outer Radius (nm)
0	94	121	70	82
100	97	123	77	94
200	102	126	83	98
300	105	132	87	103
400	118	145	90	110
500	127	160	93	165
1000	193	210	153	192
5000	433	527	340	520
10000	643	845	610	840
50000	2191	2750	1910	2400
100000	2932	3400	2907	3250
150000	4726	5800	4630	5620

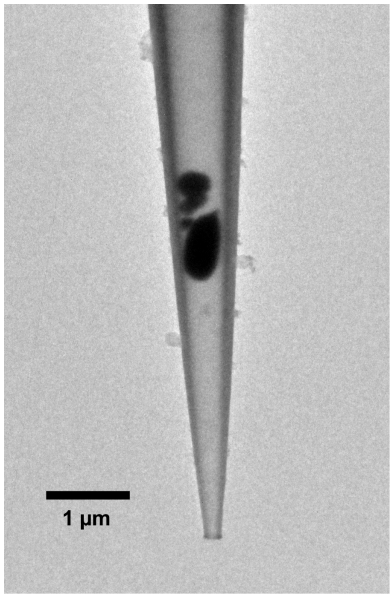

Figure 3.4. TEM image of the nanopipette used for the PC12 cell experiments presented in the manuscript.

3.6.2 FEM Simulations: FEM simulations were constructed and run in COMSOL 5.2 as outlined in the manuscript. A 2D axisymmetric domain of the nanopipette with dimensions extracted from TEM images was constructed. Simulations were either performed with 50 mM KCl in the nanopipette and bath solution or with a solution consisting of 103 mM NaCl, 23 mM $NaHCO_3$ and 5 mM KCl to mimic the main components of the RPMI 1640 media used as supporting electrolyte in PC12 cell experiments. The boundary conditions for all FEM simulations are displayed in Figure 3.5. The tip potential of either +20 mV or -400 mV was applied to the upper nanopipette boundary with the outer bath boundary held at ground. In each media, approach curves were run with an applied bias of +20 mV in order to calculate the working distance used experimentally for surface charge measurements. The charge applied to the nanopipette wall was -40 mC/m^2.

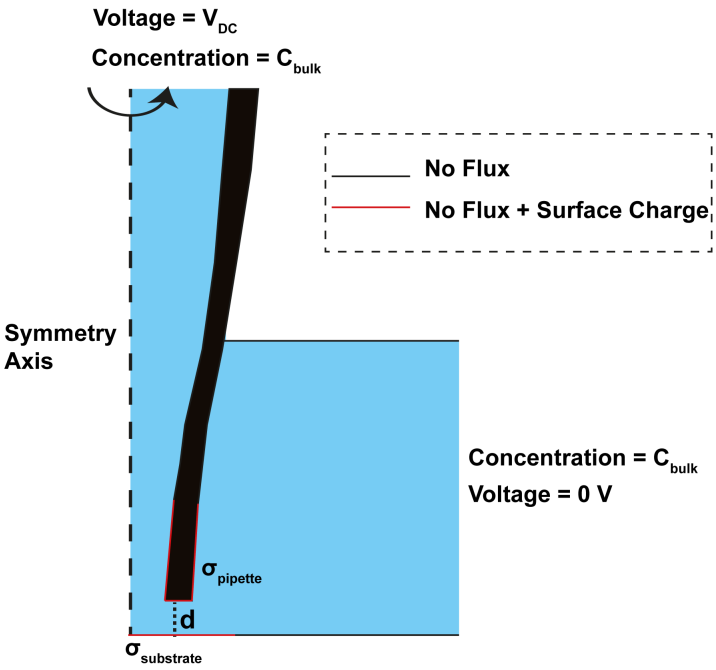

Figure 3.5. Schematic of 2D axisymmetric FEM simulation domain with applied boundary conditions depicted. Surface charge was applied to the lowest 10 μm of the inner and outer nanopipette walls. The surface charge on the boundary beneath the nanopipette was varied in order to calculate experimental surface charge values.

3.6.3 More Complete Polystyrene Scan: The SICM surface charge map of the polystyrene film presented in the manuscript suggested the presence of 3 regions, a

uniform polystyrene region with a surface charge of 0 mC/m^2, a negatively charged glass region and an in-between region which is attributed to glass pinholes smaller than the SICM nanopipette footprint giving a surface charge consisting of glass and polystyrene regions. A second scan of a more complete region of polystyrene was performed and is depicted in Figure 3.6 where instead just two distinctly charged regions are observed over the glass pinholes and the polystyrene.

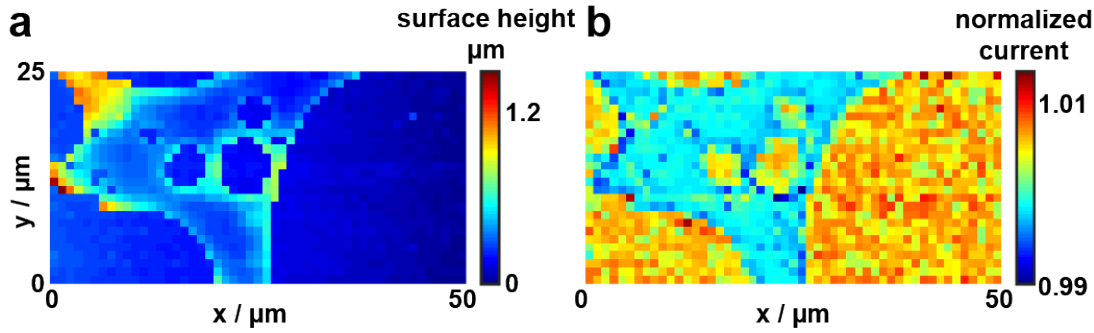

Figure 3.6. More complete polystyrene scan. SICM topographical image (a) and normalized current map (b) of a more uniform region of polystyrene film on a glass support suggesting a uniform surface charge across the polystyrene film.

3.6.4 Previous Polystyrene Scan Data: A typical image collected in the previous scanning regime of bias modulated approach feedback and cyclic voltammogram charge extraction. Presented here for comparison of pixel density and image quality.

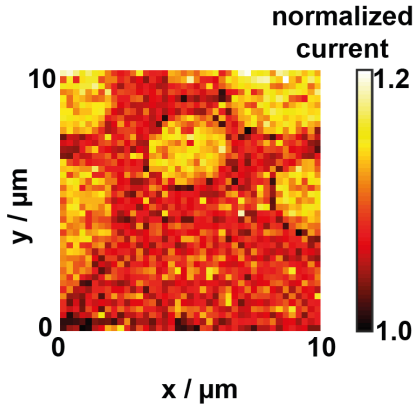

Figure 3.7. Surface charge map of a polystyrene film on a glass substrate collected using the previous bias modulation voltage scanning regime. Adapted with permission from reference 10. Copyright 2015 American Chemical Society.

3.6.5 Raw PC12 Scan Data: Figure 3.3 of the manuscript presents a surface charge map and *I-t* curves for a PC12 cell on a glass substrate. Figure 3.8 depicts the raw data used to obtain these surface charge values including the experimental map of normalized surface to bulk currents at the experimental working distance.

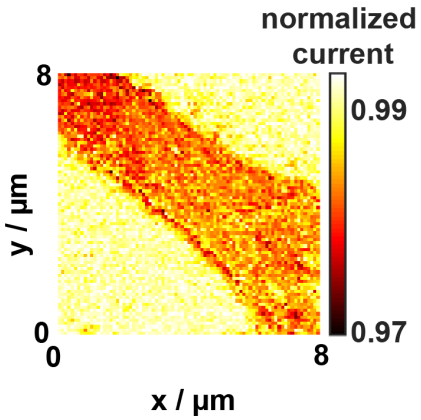

Figure 3.8. Normalized current map across the PC12 cell discussed in the manuscript, converted to estimated surface charge values presented in the map of Figure 3.3.

3.7 References

(1) Chen, C.-C.; Zhou, Y.; Baker, L. A. *Annu. Rev. Anal. Chem.* **2012**, *5* (1), 207–228.

(2) Hansma, P. K.; Drake, B.; Marti, O.; Gould, S. A.; Prater, C. B. *Science* **1989**, *243*, 641–643.

(3) Kranz, C. *Analyst* **2014**, *139* (2), 336–352.

(4) Korchev, Y. E.; Bashford, C. L.; Milovanovic, M.; Vodyanoy, I.; Lab, M. J. *Biophys. J.* **1997**, *73* (2), 653–658.

(5) Novak, P.; Li, C.; Shevchuk, A. I.; Stepanyan, R.; Caldwell, M.; Hughes, S.; Smart, T. G.; Gorelik, J.; Ostanin, V. P.; Lab, M. J.; Moss, G. W. J.; Frolenkov, G. I.; Klenerman, D.; Korchev, Y. E. *Nat. Methods* **2009**, *6* (4), 279–281.

(6) Takahashi, Y.; Murakami, Y.; Nagamine, K.; Shiku, H.; Aoyagi, S.; Yasukawa, T.; Kanzaki, M.; Matsue, T. *Phys. Chem. Chem. Phys.* **2010**, *12*

(34), 10012–10017.

(7) Happel, P.; Thatenhorst, D.; Dietzel, I. D. *Sensors* **2012**, *12* (11), 14983–15008.

(8) Nashimoto, Y.; Takahashi, Y.; Ida, H.; Matsumae, Y.; Ino, K.; Shiku, H.; Matsue, T. *Anal. Chem.* **2015**, *87* (5), 2542–2545.

(9) Shevchuk, A. I.; Frolenkov, G. I.; Sanchez, D.; James, P. S.; Freedman, N.; Lab, M. J.; Jones, R.; Klenerman, D.; Korchev, Y. E. *Angew. Chem., Int. Ed.* **2006**, *45* (14), 2212–2216.

(10) Rheinlaender, J.; Geisse, N. A.; Proksch, R.; Schäffer, T. E. *Langmuir* **2011**, *27* (2), 697–704.

(11) McKelvey, K.; Kinnear, S. L.; Perry, D.; Momotenko, D.; Unwin, P. R. *J. Am. Chem. Soc.* **2014**, *136* (39), 13735–13744.

(12) Perry, D.; Al Botros, R.; Momotenko, D.; Kinnear, S. L.; Unwin, P. R. *ACS Nano* **2015**, *9* (7), 7266–7276.

(13) Perry, D.; Paulose Nadappuram, B.; Momotenko, D.; Voyias, P. D.; Page, A.; Tripathi, G.; Frenguelli, B. G.; Unwin, P. R. *J. Am. Chem. Soc.* **2016**, *138* (9), 3152–3160.

(14) Momotenko, D.; McKelvey, K.; Kang, M.; Meloni, G. N.; Unwin, P. R. *Anal. Chem.* **2016**, *88* (5), 2838–2846.

(15) Korchev, Y. E.; Negulyaev, Y. A.; Edwards, C. R.; Vodyanoy, I.; Lab, M. J. *Nat. Cell Biol.* **2000**, *2* (9), 616–619.

(16) Zhou, Y.; Chen, C. C.; Baker, L. A. *Anal. Chem.* **2012**, *84* (6), 3003–3009.

(17) Novak, P.; Gorelik, J.; Vivekananda, U.; Shevchuk, A.; Ermolyuk, Y.; Bailey, R.; Bushby, A.; Moss, G. J.; Rusakov, D.; Klenerman, D.; Kullmann, D. M.; Volynski, K.; Korchev, Y. *Neuron* **2013**, *79* (6), 1067–1077.

(18) McKelvey, K.; Perry, D.; Byers, J. C.; Colburn, A. W.; Unwin, P. R. *Anal. Chem.* **2014**, *86* (7), 3639–3646.

(19) Takahashi, Y.; Shevchuk, A. I.; Novak, P.; Babakinejad, B.; Macpherson, J.; Unwin, P. R.; Shiku, H.; Gorelik, J.; Klenerman, D.; Korchev, Y. E.; Matsue, T. *Proc. Natl. Acad. Sci. U. S. A.* **2012**, *109*, 11540–11545.

(20) McKelvey, K. M. University of Warwick 2012.

(21) Perry, D.; Momotenko, D.; Lazenby, R. A.; Kang, M.; Unwin, P. R. *Anal. Chem.* **2016**, *88* (10), 5523–5530.

(22) Sa, N.; Baker, L. A. *J. Electrochem. Soc.* **2013**, *160* (6), H376–H381.

(23) Sa, N.; Baker, L. A. *J. Am. Chem. Soc.* **2011**, *133* (27), 10398–10401.

(24) Clarke, R. W.; Zhukov, A.; Richards, O.; Johnson, N.; Ostanin, V.; Klenerman, D. *J. Am. Chem. Soc.* **2013**, *135* (1), 322–329.

(25) Sa, N.; Lan, W. J.; Shi, W.; Baker, L. A. *ACS Nano* **2013**, *7* (12), 11272–11282.

(26) Stumm, W.; Morgan, J. J. *Aquatic chemistry: chemical equilibria and rates in natural waters*, Third Edit.; John Wiley & Sons, 1996.

4 Differential-Concentration Scanning Ion Conductance Microscopy

Building on the work in Chapter 3, this chapter also considers functionality beyond topography in a single-channel SICM setup, with the primary focus being the development of a highly sensitive feedback type. In the experiments herein, the electrolyte solution in the nanopipette and the bath are prepared at different concentrations (both high-probe/low-bath and low-probe/high-bath are explored), inducing a potential difference both between the two QRCEs (as they are in different solutions) and at the junction at the end of the nanopipette. This work shows that it is possible to separate these two potential differences, and that operating under a junction potential driven regime holds several advantages such as a reduced electric field at the end of the probe. This setup is then used for multifunctional imaging, and is shown to be as successful as conventional SICM for both the topography-charge mapping of living cells, and for the topography-reaction mapping of electrode substrates.

This chapter has been submitted as an article to *Analytical Chemistry*. Experiments were performed by the author and Dr. David Perry, who carried out the FEM simulations after they had been jointly discussed. Cell culturing was also performed together, while Baoping Chen prepared the devices used for electrode reaction mapping. The manuscript was prepared jointly by the author and Dr. Perry.

Differential-Concentration Scanning Ion Conductance Microscopy

David Perry,[1,†] Ashley Page,[1,2,†] Baoping Chen,[1] Bruno G. Frenguelli[3] and Patrick R. Unwin[1,]*

[1]Department of Chemistry, [2]MOAC Doctoral Training Centre, [3]School of Life Sciences, University of Warwick, Coventry, CV4 7AL, United Kingdom.

†These authors contributed equally to this work

*corresponding author

p.r.unwin@warwick.ac.uk

4.1 Abstract

Scanning ion conductance microscopy (SICM) is a nanopipette-based scanning probe microscopy technique that utilizes the ionic current flowing between an electrode inserted inside a nanopipette probe containing electrolyte solution, and a second electrode placed in a bulk electrolyte bath, to inform on a substrate of interest, usually to map the surface topography. SICM has recently been extended beyond topographical mapping to become a powerful tool for probing surface charge and interfacial reactivity. For most applications to date, the composition and concentration of the electrolyte inside and outside the nanopipette is identical, but it is shown herein that it can be very beneficial to lift this restriction. This study comprehensively analyzes the SICM setup where different electrolyte concentrations are used in the nanopipette probe and bulk solution. A concentration gradient at the end of the nanopipette, induced by changing the ionic strength in the tip compared to the bath, generates an ionic current with a greatly reduced electric field strength at the end of the pipette. This has benefits for live cell imaging (topographical and functional) since electric fields can perturb living cells from their natural state. This differential concentration mode of SICM (ΔC-SICM) enhances surface charge measurements of living cells (using a low electrolyte concentration in the tip) and provides a new way to carry out reaction mapping measurements using the tip for delivery and sensing the reaction rate. In both cases, experimental strategies are implemented where topographical measurements are made simultaneously. Comprehensive finite element method (FEM) modeling has been undertaken to both

analyze data quantitatively and to interpret and optimize experiments. An important outcome of the modeling is that electroosmotic flow has significantly more influence on the nanopipette response in the ΔC-SICM configuration than compared to standard SICM modes. The model presented is general and advances previous treatments of SICM, solving for the electric field, transport of species and electroosmotic flow simultaneously, and provides a framework for future use in quantitative studies with SICM.

4.2 Introduction

Scanning ion conductance microscopy (SICM) is a powerful non-contact imaging technique capable of high-resolution topographical measurements.[1,2] In particular, SICM has found wide application in visualizing living cells,[3–6] at probe distances (separations) of tens to hundreds of nanometers from the cell surface.[7,8] SICM experiments utilize a glass or quartz nanopipette filled with electrolyte solution as the scanning probe. A quasi-reference counter electrode (QRCE) is placed in the nanopipette and, typically, a bias is applied between the probe electrode and another electrode in bulk solution to drive an ionic current through the end of the nanopipette between the two electrodes.[2] As the probe approaches an interface, the ionic current often decreases as the gap resistance between the probe and surface increases.[2] Thus, the ionic current can be used as feedback to position the probe near a substrate, and obtain topographical information by moving the probe.[2]

Since its inception,[1] there have been several key developments in both the feedback types and scan regimes that can be used for SICM.[2,9,10] These include the introduction of modulated feedback types[11–13] and hopping scan regimes[5,14,15] which have improved both the stability of the technique and its ability to successfully scan a range of samples. There has been a recent drive to develop SICM for multifunctional imaging,[10] begetting more complex scan regimes and probes to obtain a wealth of information on interfaces and interfacial processes. These capabilities include the detection of electrochemical reactions,[16] the surface charge of cellular membranes,[7,8,17,18] and quantitative monitoring of cellular uptake of electroactive molecules.[19] Several of these studies have demonstrated the importance of minimizing the applied bias in SICM experiments.[7,8,17] For example, it has been demonstrated that the larger the applied bias between the tip electrode and that in

bulk solution, the greater is the convolution of topographical information with other surface properties, particularly surface charge, with important implications for the precision of SICM topographical measurements.[20,17]

The tip and bathing solutions usually have the same composition, but some SICM studies and measurements with nanopipettes have used electrolyte solutions in the nanopipette and the bulk solution that are different in composition and/or concentration.[19,21,22] There are several advantages of such conditions, including the local delivery of molecules for printing and patterning,[22–24] or in studies of cellular uptake.[19] Hitherto, however, the effect of different electrolyte solutions on the equilibrium potentials of the tip and bulk electrodes, and thus the overall driving potential, has largely been ignored because the applied bias is often large compared to any differences in the equilibrium electrode potentials. As one attempts to minimize the bias in an SICM setup, it becomes important to understand how differences in the equilibrium potentials of the two electrodes affect the ionic current response.

In this contribution, we investigate the use of different concentrations of electrolyte solution in the tip and bulk solution, in particular, determining how the ionic concentration gradient between the probe and the bulk solution gives rise to a junction potential at the end of the nanopipette that allows an ionic current to flow. We demonstrate practically how this SICM mode, which we call differential concentration (ΔC)-SICM, can be used to map topography with a precision comparable to SICM in conventional operation, and use finite element method (FEM) simulations to verify our findings. Significantly, this approach can be used to improve the sensitivity of functional measurements with SICM. In particular, we show herein that ΔC-SICM can be used to probe cellular surface charge, under physiological conditions using a dilute electrolyte solution in the tip. The precision is better (wider dynamic range to surface charge) than previous SICM methods. Further, ΔC-SICM can be used with a higher electrolyte concentration in the tip compared to the bathing solution. This is applied as a new approach to image electrochemical reactions at an electrode surface purely via the SICM response, as exemplified with a study of dopamine oxidation at a carbon fiber electrode. The ability to tune the composition in the SICM tip, compared to the bulk solution, greatly expands the versatility of SICM.[23,25]

The work herein develops a comprehensive understanding of the potential distribution and mass transport in ΔC-SICM, solving for the electric field, concentration and flow simultaneously. In particular, we assess the importance of electroosmotic flow in ΔC-SICM compared to conventional SICM. Significant consequences of this work are that interfaces can be studied by SICM with minimal electric field effects and that topography and other effects can be deconvoluted in a robust manner, with enhanced resolution for functional mapping compared to conventional SICM.

4.3 Materials and Methods

4.3.1 Solutions: Milli-Q reagent grade water (resistivity ca. 18.2 MΩ cm at 25°C) was used for all solutions. PC12 cells were cultured and imaged in RPMI 1640 media containing 15% horse serum, 2.5% fetal calf serum, 5 mM glutamine, 100 U/mL penicillin and 100 μg/mL streptomycin (all Sigma Aldrich). The nanopipette tip, for topographical and surface charge measurements of living cells, contained a 1% dilution of the full cell culture media. For reaction mapping experiments, a 10 mM KCl solution was used as the bulk electrolyte whilst the nanopipette contained either 80 mM KCl (for control experiments) or 50 mM KCl and 30 mM dopamine hydrochloride (unbuffered, pH 6.7).

4.3.2 Nanopipettes and Electrodes: Nanopipettes were pulled from borosilicate glass capillaries (o.d. 1.2 mm, i.d. 0.69 mm, Harvard Apparatus) using a laser puller (P-2000, Sutter Instruments; pulling parameters: Line 1: Heat 330, Fil 3, Vel 30, Del 220, Pul -; Line 2: Heat 330, Fil 3, Vel 40, Del 180, Pul 120). The inner radius of probes was measured using a JEOL 2000FX transmission electron microscope (TEM) to be 90 nm ± 15 nm. Two Ag/AgCl quasi-reference counter electrodes (QRCEs), one in the nanopipette and a second in bulk solution, were used for both topographical and charge mapping. These were AgCl-coated wires prepared as described previously.[26] For reaction mapping experiments, an individual carbon fiber (CF) was used as a substrate and was electrically connected to allow a potential offset to be applied with respect to the bulk QRCE (see 'Substrate Preparation').

4.3.3 Cell Culturing Procedure: Adherent PC12 cells (ATCC-CRL-1721.1) were cultured in tissue culture flasks in the above-specified media until confluent, before trypsinization and transfer to Petri dishes. They were allowed 72 hours to adhere to the glass substrate before imaging in fresh media.

4.3.4 Substrate Preparation: The PC12 cells used were adherent to glass-bottomed petri dishes (3512, WillcoWells) and these were used as a support. Individual CFs (diameter 7 μm) were adhered to a glass microscope slide using a piece of Kapton tape placed over the top. The tape contained a hole of 500 μm diameter to leave part of the fiber exposed for scanning and electrochemistry. The bias applied to the CF was via a copper wire connected to one end of the fiber with conductive silver paint. This contact was then insulated with wax so that it was not exposed to the solution.

4.3.5 Instrumentation: The lateral movement of the sample was controlled using a two-axis piezoelectric positioning system with a range of 300 μm (Nano-BioS300, Mad City Labs, Inc.), while movement of the probe normal to the substrate was controlled using a piezoelectric positioning stage of range 38 μm (P-753-3CD, Physik Instrumente), to which the probe was mounted. As described previously,[9] the current-voltage converter used was made in-house, while user control of probe position, voltage output and data collection was via custom made programs in LabVIEW (2013, National Instruments) through an FPGA card (7852R, National Instruments).

4.3.6 Determination of Equilibrium Potentials: As the two QRCEs (AgCl-coated Ag wires as often employed in SICM)[2,12,27] used in ΔC-SICM were in solutions of different ionic strength and composition, they each have different equilibrium potentials. In order to quantify the equilibrium potentials of the QRCEs in both full RPMI media and in a 100-fold dilution, the QRCE potentials in these media were measured against a saturated calomel electrode (SCE) and were found to be 22 mV and 131 mV, respectively. For experiments which utilized 50 mM KCl and 30 mM dopamine hydrochloride, the potential was 36 mV vs. SCE, while in 10 mM KCl the potential was 71 mV vs. SCE. For 80 mM KCl, the potential was 34 mV vs. SCE. Knowledge of these potentials allowed us to control the driving force in SICM,

which operates as an electrochemical cell. The experimental setup also gives rise to a junction potential at the end of the nanopipette (Figure 4.1) where the two solutions of different concentration meet (and mix). In order to apply SICM using solely the junction potential, the measured equilibrium potential difference between the QRCEs was offset with an external bias that was equal in magnitude, but of opposite polarity.

4.3.7 ΔC-SICM Mapping: For the approach curves and topographical maps herein, the bulk electrolyte was the full RPMI 1640 media described above, the majority of which is 103 mM NaCl, 24 mM $NaHCO_3$ and 5 mM KCl, with the nanopipette containing a 100-fold dilution. This environment allowed the cells to function normally with the local environment near the end of the nanopipette transiently perturbed while making an SICM measurement.

For approach curve measurements, the nanopipette was approached towards the glass substrate (*z* direction) at a speed of 2 μm/s (with the position of the probe in the *x*-*y* plane of the substrate fixed). Topographical scans were performed in a scan hopping regime that generated pixel by pixel maps. A nanopipette approach and retract rate of 20 μm/s was used and a 2% decrease in the ionic current was used to sense the surface, corresponding to a tip-surface distance ca. 60 nm. After recording the distance of closest approach, the probe was retracted and moved to the next pixel, so as to cover an array of *x*, *y* points. Topographical maps contained 6400 pixels and were obtained in 15 minutes.

Charge mapping experiments were performed in a similar manner, but with a potential pulse (+0.4 V applied at the bulk QRCE for a period of 20 ms), during which the tip current-time response was measured, after the approach for each pixel.[8] For these experiments, a decrease of the current by 5% compared to the bulk recorded current was used to sense the substrate (topographical map), corresponding to a tip-substrate distance of 22 nm (*vide infra*). The average current that was measured during the last 1 ms of the pulse was normalized by the corresponding current, at the equivalent time, recorded by applying the same pulse protocol with the probe 7 μm from the surface (bulk solution) *at each pixel*. A full description of the surface charge mapping experimental regime can be found in section 4.6.1 of the Supporting Information.

Reaction mapping experiments also used a scan hopping regime, but with 10 mM KCl in the bath solution and 50 mM KCl and 30 mM dopamine hydrochloride present in the nanopipette, or 80 mM KCl in the nanopipette for control experiments. The applied bias between the two QRCEs for SICM feedback was 0 V throughout, while the potential applied to the substrate electrode was varied. During the approach of the nanopipette to the surface, the potential of the CF was held at -0.1 V vs. the Ag/AgCl electrode in bulk to ensure that no oxidation of dopamine took place.[28,29] Upon approach to the near-surface, detected by a drop of 3% in the ionic current, corresponding to a tip-surface distance ca. 35 nm, the potential of the CF was swept from -0.1 V to +0.4 V and back again to -0.1 V in a cyclic voltammogram (CV) at 1 V/s, and the SICM current was recorded simultaneously. The potential of the CF was held at -0.1 V while the nanopipette was retracted before repeating the same CV at the substrate with the probe in bulk solution (separation of 10 μm).

4.3.8 FEM Simulations: A 2D axisymmetric cylindrical model of the nanopipette at different distances from a substrate was constructed in COMSOL Multiphysics (version 5.2a) with the Transport of Diluted Species, Laminar Flow and Electrostatics modules. Full simulation details, including a schematic of the simulation domain and boundary conditions are presented in the Supporting Information, section 4.6.2. The dimensions of nanopipettes used experimentally were determined from TEM images to ensure that simulations faithfully modeled experiments.

4.4 Results and Discussion

4.4.1 General Considerations: In ΔC-SICM, because the solution environment of the two Ag/AgCl QRCEs is different, there is a potential difference between them:

$$\Delta E_{Electrode} = E_{Electrode,tip} - E_{Electrode,bulk} \qquad (4.1)$$

in which $\Delta E_{Electrode}$ is the difference in electrode potentials, $E_{Electrode,tip}$ is the potential of the QRCE inside the nanopipette, and $E_{Electrode,bulk}$ is the potential of the QRCE in the bulk solution. A further consideration is that the difference in concentration internally and externally, near the end of the nanopipette, gives rise to

a junction, or diffusion potential. Further, an external potential, $E_{external}$, can be applied across the two electrodes. Thus, considering SICM as an electrochemical cell (Figure 4.1), the overall potential in ΔC-SICM is:

$$E_{total} = \Delta E_{Electrode} + E_{junction} + E_{external} \qquad (4.2)$$

ΔC-SICM can be used flexibly, with the higher concentration electrolyte solution in the probe or the bulk solution (*vide infra*). For the live cell studies, where the electrolyte concentration is lower inside the nanopipette domain, $E_{Electrode,tip} < E_{Electrode,bulk}$ and thus $\Delta E_{Electrode}$ is negative, whilst $E_{junction}$ is positive. In experiments, where an external bias of 0 V was applied, and the current results from a combination of only $\Delta E_{Electrode} + E_{junction}$, currents typically around -500 pA were recorded with the nanopipette in bulk solution. Where $\Delta E_{Electrode}$ was cancelled by applying a counter bias, $E_{total} = E_{junction}$, which produced a current of around +50 pA.

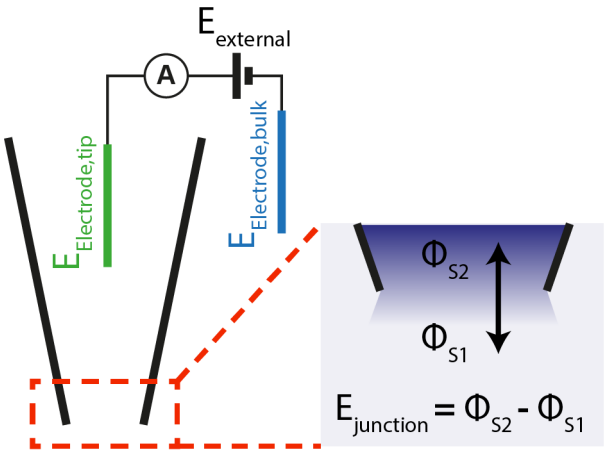

Figure 4.1. Schematic of the potential differences in a ΔC-SICM system. A difference in electrolyte concentration (composition) inside and outside of the nanopipette leads to different potentials, $E_{Electrode,tip}$ and $E_{Electrode,bulk}$, of the two QRCEs. A diffuse junction potential, $E_{junction}$, is present at the end of the nanopipette where the two solutions of potential ϕ_{S2} (in the tip) and ϕ_{S1} (in the bathing solution) meet. An external bias, $E_{external}$, may also be applied.

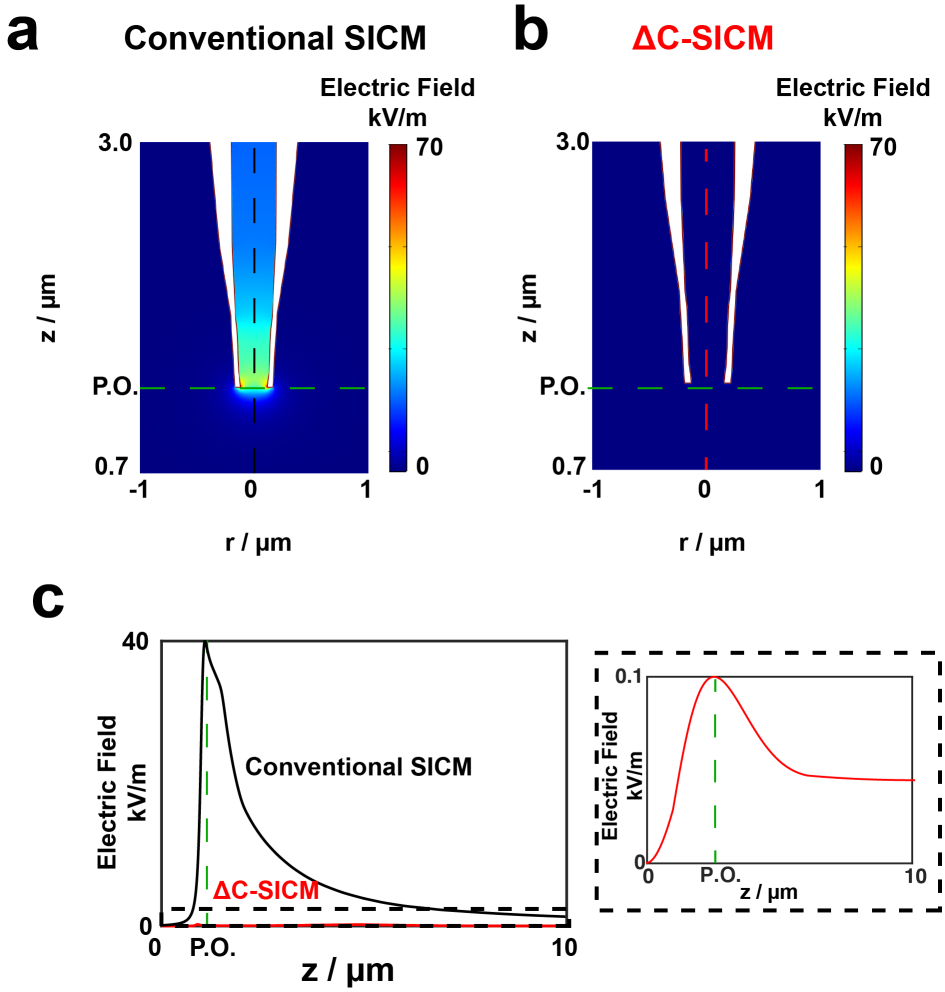

Figure 4.2. Comparison of electric field strength in conventional and ΔC-SICM. (a) Electric field magnitude at the end of a 90 nm radius nanopipette in standard imaging conditions with a 100 mV bias applied to the bulk electrode with the same electrolyte (103 mM NaCl, 24 mM $NaHCO_3$ and 5 mM KCl) present in both the pipette and bulk solutions. (b) Electric field magnitude at the end of a 90 nm radius nanopipette under ΔC-SICM conditions (103 mM NaCl, 24 mM $NaHCO_3$ and 5 mM KCl in the bath solution, 100-fold dilution in the tip) with the current driven only by $E_{junction}$. (c) Line profiles of the electric field strength in the z-direction up the axis of symmetry of the pipette with the peak corresponding to the nanopipette opening. Profile for typical SICM shown in black and ΔC-SICM in red, with the inset showing a zoom of the ΔC-SICM profile.

In the second configuration, where a higher electrolyte concentration was present in the nanopipette, i.e. the case where dopamine was delivered to a CF electrode, $E_{Electrode,tip} > E_{Electrode,bulk}$ and hence $\Delta E_{Electrode}$ is positive and $E_{junction}$ negative.

FEM simulations allowed the electric field at the end of the nanopipette to be readily calculated. It is informative to compare one of the cases herein, where the ionic current is generated solely by $E_{junction}$, (i.e. $E_{external} = -\Delta E_{Electrode}$), to conventional SICM imaging parameters (100 mV tip bias, within the normal range of values applied,[3–5,14,15,18,30] and the same concentration in the bath and tip). These cases are presented and compared in Figure 4.2, with the tip in bulk solution. Under the conventional SICM conditions (a), an electric field of up to 40 kV/m is established at the end of the nanopipette. It can be seen that with only the liquid junction potential (b), the only significant electric field arises from the double layer due to the negative charge on the walls of the charged nanopipette (σ_{tip}=-30 mC/m^2, considered as typical for these conditions[31]). In the region at the nanopipette opening, the electric field is at least two orders of magnitude less than when a bias of 100 mV is applied between the inside and outside of the nanopipette, with the effect of $E_{junction}$ spread over a long distance (Figure 4.2c). In cases where the applied SICM bias is greater than 100 mV, the electric field strength would be significantly greater. Consequently, for delicate substrates such as living cells, which can be perturbed/stimulated by the presence of an electric field,[32–34] ΔC-SICM will be much less perturbing and less invasive.

4.4.2 Topographical Mapping of Living Cells: For all of the work herein using PC12 cells, the bulk solution was full RPMI 1640 media (see 'Experimental' for details) with the nanopipette containing a 100-fold dilution of the same solution. $E_{external}$ was set to cancel out $\Delta E_{Electrode}$ (the case outlined in the preceding section), so that $E_{total} = E_{junction}$. Figure 4.3a presents an experimental approach curve of a nanopipette towards the glass support on which PC12 cells were cultured. It can be observed that at decreasing tip-substrate distances the ionic current decreases, in line with the traditional SICM response, and hence this feedback type can be used for topographical measurements.[2] FEM simulations were performed for the same conditions, at a range of tip-substrate separations to generate a theoretical

approach curve (Figure 4.3a and Supporting Information, Figure 4.11). This approach curve suggests the same behavior observed experimentally with a diminished ionic current at small tip-substrate distances.

ΔC-SICM was used to generate topographical maps of PC12 cells exhibiting different degrees of differentiation, as evidenced by the presence or absence of protrusions known as neurites from the cell body (Figure 4.3b,c).[35] It can be seen that ΔC-SICM provides a reliable feedback signal at an approach rate of 20 μm/s and generates comparable maps to those seen previously with more conventional feedback types.[8]

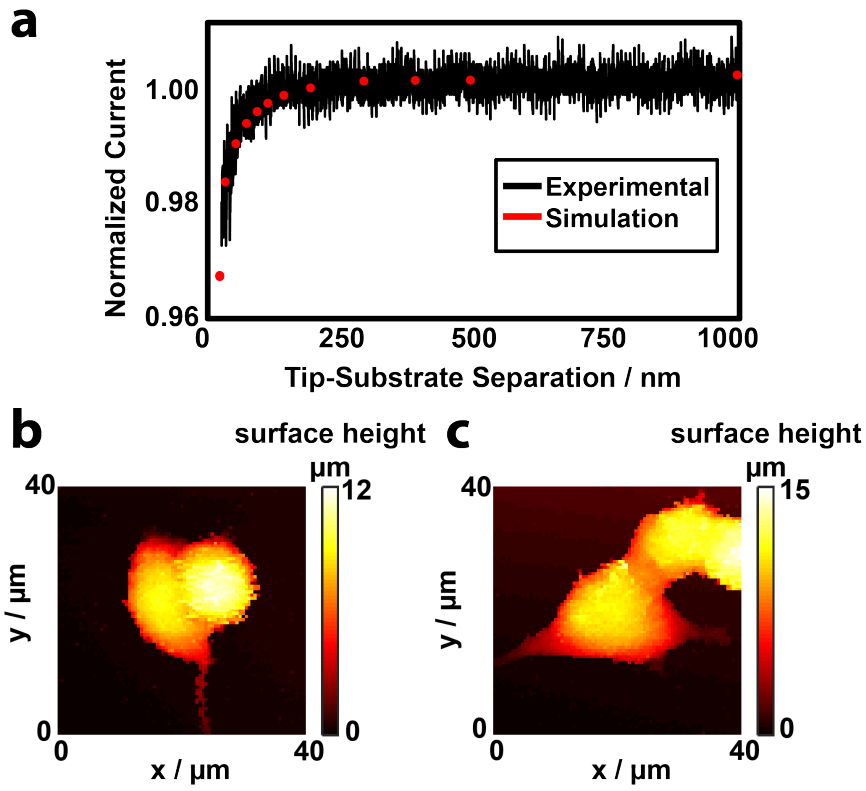

Figure 4.3. The use of ΔC-SICM as feedback for topographical imaging. (a) Experimental approach curve (black) of a ~90 nm radius nanopipette containing 100-times diluted RPMI media, in a bulk solution of full strength media, with $E_{total} = E_{junction}$. The nanopipette approach rate was 2 μm/s at each pixel. Simulated approach curve (red) of the conditions used experimentally. Topographical images of PC12 cells (b,c) collected in a scan-hopping regime at an approach rate of 20 μm/s with the same solutions and applied bias as (a). Note: there is no interpolation of data with scans containing 6400 pixels, collected in 15 minutes.

4.4.3 Surface Charge Mapping with ΔC-SICM: A recent development in SICM has been its use for surface charge mapping.[18,20] Significantly, we have shown that it is possible to map charge heterogeneities in cell membranes under physiological conditions (high ionic strength) even though the electrical double layer is compressed to a high degree. Our approach is to use a self-referencing pulsed-potential program, in which the tip current response is measured near the surface and compared to that in bulk solution at each and every pixel.[8] Although under physiological conditions (ionic strength ~130 mM), the Debye length is less than 1 nm, the diffuse layer extends beyond this.[36] For example, assuming the Gouy-Chapman model (as a simplification), at a distance 5 nm away from a uniformly charged interface, the ionic concentration, for a 1:1 electrolyte, deviates by around 0.5% from that of the bulk solution.[36] Most importantly, even though the SICM tip is stationed beyond this distance, e.g. herein at an approximate separation of 20 nm or more, when an external bias is applied, the double layer is perturbed by the electric field at the pipette orifice, and thus affects the current flow (*vide infra*). It is for this reason that in conventional SICM, we have advocated the use of either bias modulation[17] (with zero net bias) or a small DC current[8] to minimize perturbation of the double layer and obtain more faithful topographical information.

In order to assess the possibility of using ΔC-SICM for charge mapping, FEM simulations were performed with the nanopipette both in bulk solution and near a charged interface (27 nm separation, within the typical range of approach distances achieved). As part of these simulations, we also assess the importance of EOF in the SICM response. Previous studies have considered EOF to not significantly influence the SICM response under a range of conditions,[20,37,38]and it is often ignored due to computational expense.

The data presented in Figure 4.4 compares the normalized current response of conventional SICM, with and without EOF, to ΔC-SICM, with and without EOF, for a range of negative surface charges (as typically predominant on cell membranes[7]). There are several important points that are immediately apparent from these data. Most significantly, EOF is a particularly important consideration for ΔC-SICM and can never be ignored. Indeed, for reasons we explain below, the sensitivity of the normalized ΔC-SICM response to surface charge is due to EOF. In

the case of conventional SICM (100 mV bias applied, same concentration in both the bath and tip solutions), at the lower surface charge densities applied to the substrate, EOF has very little effect on calculated ionic currents, in line with previously reported studies.[10,20,37] However, as the surface charge increases beyond about -30 mC/m^2, EOF can be seen to be an important consideration. Thus, for high surface charge densities, even with conventional SICM, EOF should be treated to quantify surface charge with the highest accuracy.

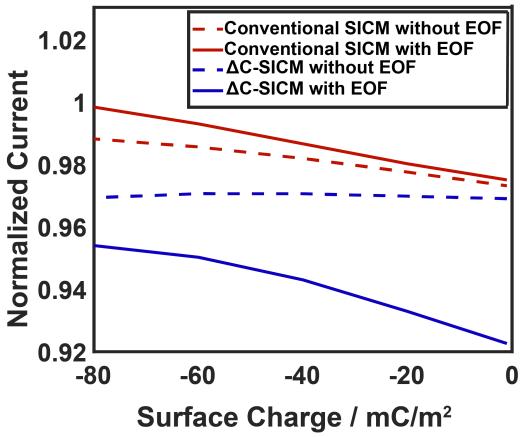

Figure 4.4. Normalized current versus substrate surface charge density for different modes and mass transport situations in SICM. Normalized currents were calculated 20 ms into an current-time (*I-t*) curve after applying an external bias of -400 mV to the nanopipette QRCE, jumped from the approach bias ($E_{external}$=$-\Delta E_{Electrode}$ in the case of ΔC-SICM, 100 mV for conventional SICM). The red lines depict the case where the same concentration (103 mM NaCl, 24 mM $NaHCO_3$ and 5 mM KCl) was present in both the nanopipette and bath. The blue lines were simulations performed with a 100-fold dilution of this solution in the nanopipette. The dashed lines represent simulations solving only the Nernst-Planck and Poisson equations, while the solid lines also included EOF. The raw simulated ionic currents underlying these data are shown in Supporting Information, Figure 4.12.

It can be seen from Figure 4.4, that diluting the nanopipette electrolyte concentration compared to the bulk solution enhances sensitivity (dynamic range) of the SICM current to surface charge with a range of 3.2% compared with the 2.3% in the conventional SICM case, over a range of 80 mC/m^2 (considering EOF, full

model). These may appear small changes in the signal, but are easily detected because of the pixel-level self-referencing technique inherent in the hopping mode protocol.

Differences between ΔC-SICM (Figure 4.5a) and conventional SICM (Figure 4.5b), in terms of concentration profiles, electric field strength, and velocity profiles (from EOF) at the end of a nanopipette, near the most extreme negatively charged substrate (-80 mC/m^2), are shown in Figure 4.5. As mentioned above, it is possible to sense the double layer, with conventional SICM, at large distances from the interface, compared to the double layer dimension, because the double layer becomes perturbed by the applied electric field from the tip. This is apparent in Figure 4.5b(i) where it can be seen that the distance over which a higher (compared to bulk) cation concentration near the negatively charged surface, extends greatly from the interface in the region under the center of the nanopipette.

In the case of ΔC-SICM, the double layer region is not perturbed in the same way (Figure 4.5a(i)) due to the greatly diminished electric field at the end of the pipette (Figure 4.5a(ii). This diminished electric field can be explained by considering the electrolyte concentrations present in the nanopipette and bulk domains. In ΔC-SICM, where a lower electrolyte concentration is initially present in the nanopipette domain, the end of the nanopipette becomes more concentrated as more concentrated solution from outside moves into the nanopipette. Consequently, the region at the end of the nanopipette becomes less resistive and hence, the electric field strength will be greatest further up the nanopipette where the ionic strength is still low. However, despite the double layer not being perturbed to the same degree, as Figure 4.4 revealed, and as experimental data presented later show, ΔC-SICM is sensitive to surface charge, and the sensitivity is due to EOF.

Figure 4.5a(iii) shows a fluid velocity profile in ΔC-SICM with $E_{external} = -0.4$ V. It can be seen that between the charged nanopipette wall and the substrate there is a significant radial velocity bringing solution from outside the pipette into the narrow gap under the nanopipette and fluid then flows up into the pipette domain. Under the ΔC-SICM conditions considered, this movement of fluid is from an area of higher concentration (external to the nanopipette) to lower (in the nanopipette), greatly changing the ionic composition in the lower region of the nanopipette. For conventional SICM (Figure 4.5b(iii)), EOF brings solution between

two regions of similar concentration. Thus, although the fluid velocity is higher in conventional SICM, compared to ΔC-SICM, (compare Fig 4.5a(iii) and Figure 4.5b(iii)), due to the higher electric field in the case of conventional SICM, the overall effect on mass transport, as compared to ion migration, is less. The velocity profiles give an indication as to the resolution of ΔC-SICM for surface charge mapping. It can be seen that the region of greatest velocity, driven by surface charge and EOF, is between the walls of the pipette and the substrate with the velocity quickly dropping off to bulk by around 3/2 times the pipette diameter. Future work could consider optimizing the nanopipette geometry, including the wall/lumen ratio, for enhancing surface charge sensitivity and resolution.

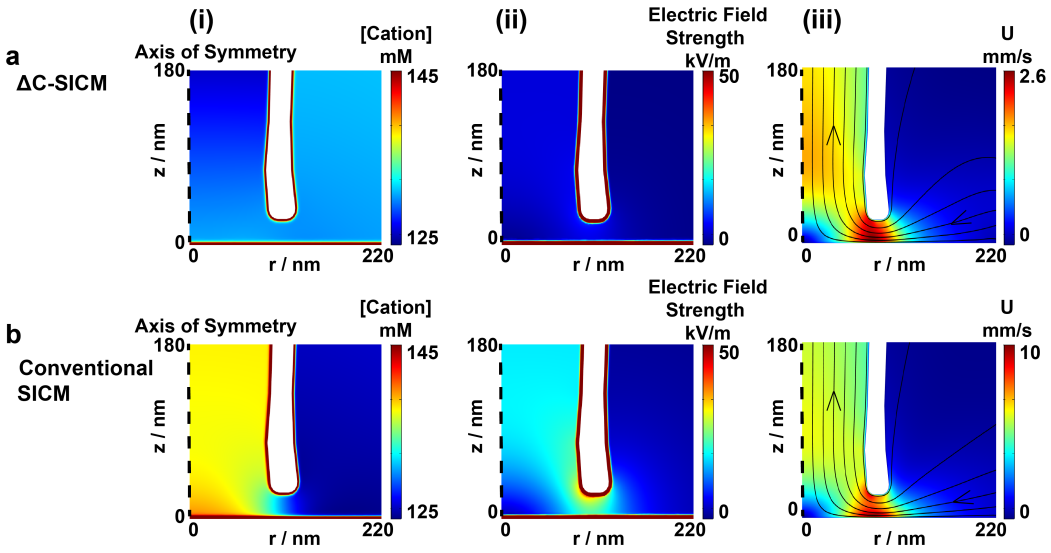

Figure 4.5. Dependence of electrolyte properties on SICM configuration. Cation concentration (i), Electric field strength (ii), and velocity profiles (iii) at the end of the nanopipette near a substrate with a surface charge of -80 mC/m^2 shown for: (a) ΔC-SICM with a 100-fold dilution in the nanopipette domain; and (b) conventional SICM case with identical concentrations in the nanopipette and bulk. All profiles are taken at t = 20 ms after jumping the potential of the nanopipette electrode to -400 mV from either $E_{external} = -\Delta E_{Electrode}$, in the case of ΔC-SICM (a), or from +100 mV in the case of conventional SICM (b).

4.4.4 ΔC-SICM Surface Charge Mapping using $E_{junction}$: ΔC-SICM measurements of surface charge and topography considered PC12 cells as the substrate. To minimize convolution between topography and other surface properties and to

reduce the electric field strength at the end of the nanopipette (Figure 4.2), only $E_{junction}$(~20 mV) was used as the topographical imaging potential. An external bias, $E_{external}$, of -109.1 mV was applied to counter $\Delta E_{Electrode}$ so that $E_{total} = E_{junction}$ (equation 4.2).

Figure 4.6a shows an optical micrograph of a cluster of differentiated PC12 cells. The area denoted by the white dashed rectangle indicates the SICM scan area mapped with the pulsed-potential regime described above. $E_{total} = E_{junction}$ was applied to map the topography of the cellular surface (Figure 4.6b). For comparison, Supporting Information, Figure 4.13b, presents the case where $E_{total} = E_{junction} + \Delta E_{Electrode}$ was the bias for topography imaging.

The simultaneously collected normalized current map (Supporting Information, Figure 4.14a) obtained during the chronoamperometric step, where the tip electrode potential was pulsed to -0.4 V for 20 ms, reveals heterogeneities, which can be attributed to surface charge. By employing FEM simulations, it becomes possible to quantify the surface charge density. Time-dependent simulations, after the potential was stepped to -400 mV, were performed with different surface charge densities applied. This allowed a calibration curve of normalized current to surface charge density to be calculated (Supporting Information, Figure 4.14b) from which Figure 4.6c was generated. It can be seen that the PC12 cell exhibited surface charge values of around -50 to -70 mC/m^2 with the glass having surface charge of around -20 to -40 mC/m^2, broadly in agreement with our previous measurements with conventional SICM,[8] that used the simplified model without EOF.

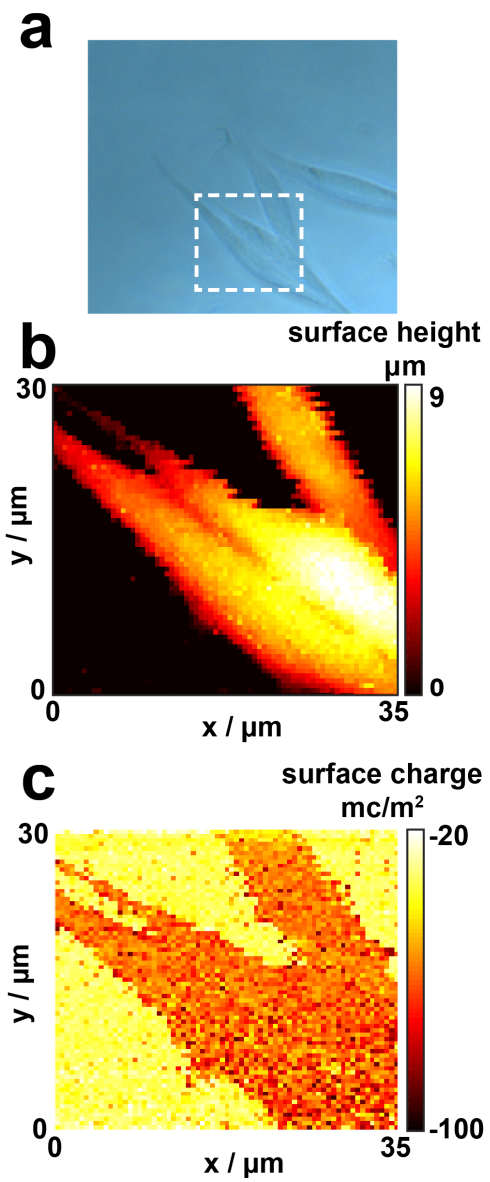

Figure 4.6. Surface charge mapping of PC12 cells using ΔC-SICM. (a) Optical micrograph of PC12 cells on a glass substrate, with the SICM scan area denoted by the white dashed rectangle. (b) Topographical map collected with a ~90 nm radius nanopipette using ΔC-SICM and a driving potential of $E_{total} = E_{junction}$. A decrease of 5% in the ionic current between the tip in bulk and near the surface was used as the set point, corresponding to a distance of 22 nm. (c) Corresponding surface charge map obtained by converting the normalized current map (see Materials and Methods section for normalization procedure) using a FEM simulated calibration curve. The normalized current map underpinning these data and the calibration curve are shown in Supporting Information, Figure 4.14. The SICM images each have 4200 pixels and there is no interpolation of data.

4.4.5 Reaction Mapping at a Carbon Fiber Electrode: A higher electrolyte concentration in the nanopipette, compared to the bulk solution, can be particularly useful for the local delivery of charged molecules of interest to a surface or interface.[16,22] Although previous studies have considered using nanopipettes for molecular delivery, the effect of concentration gradients on modifying the electric potentials applied and on the current response is only rarely considered during modeling,[39] and nanopipette surface charge is largely ignored. We now describe the use of ΔC-SICM for mapping electrochemical reactions. As an exemplar system, we consider dopamine oxidation (at pH 6.7) on a CF electrode (see Supporting Information, Figure 4.15a for an optical micrograph of the substrate). Such systems are widely used for studies of single neurons,[40] but there is little information on the response of CF electrodes at the local level.

ΔC-SICM data was collected in a scan hopping CV regime. The SICM bias between the two QRCEs was held constant at $\Delta E_{Electrode} + E_{junction}$ (i.e. no external potential applied) corresponding to E_{total} = 26 mV, a small positive value suitable for topographical imaging which also drives the migration of protonated dopamine (Dop^+),[29,40] out of the nanopipette, throughout the entire imaging process. Thus Dop^+ is pushed out the nanopipette by the inherent bias but the *rate* depends on the local environment (reactions) and is reflected in the *nanopipette current* (*vide infra*). During the approach of the nanopipette to the CF surface, the CF was held at a potential of -0.1 V vs. the Ag/AgCl QRCE in bulk so that no substrate electrode reaction occurred. When the nanopipette reached the near-surface (ca. 35 nm based on a set point of 3%), its position was fixed and the potential at the CF was swept from -0.1 V to 0.4 V and back again to -0.1 V in a CV at 1 V/s vs. the Ag/AgCl QRCE in bulk. The CF was then held at -0.1 V while the probe was retracted at a speed of 20 μm/s (retract distance 10 μm), and the same CV at the substrate was run with the probe now effectively in bulk solution. The tip ionic current response from the CV at the surface was normalized by that from the CV in bulk and is a measure of the relative conductance of the probe near the surface with respect to the bulk (see Supporting Information, section 4.6.6 for full details of the experimental setup and scanning regime).

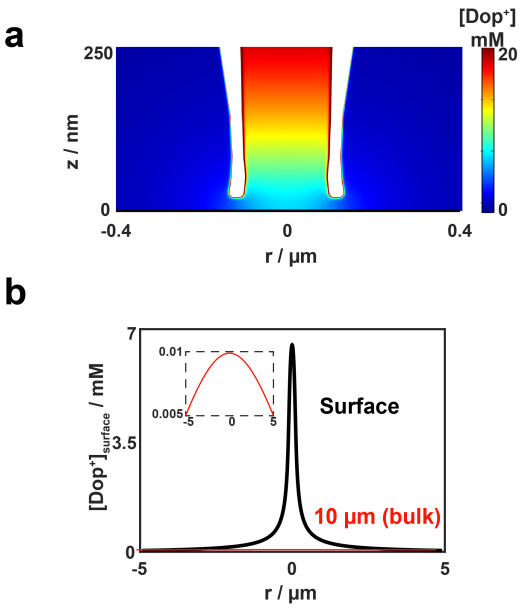

Figure 4.7. Effect of probe-surface separation on dopamine concentration. (a) Dopamine concentration profile around the end of the nanopipette (positioned 35 nm away from the substrate (distance corresponding to experimental feedback setpoint, see Supporting Information Figure 4.11b). (b) Surface concentrations of dopamine in the radial direction with the nanopipette 35 nm away from the surface (black line) and 10 µm away (red line) with the inset, showing a zoom of data for the 10 µm distance case.

An important consideration of these measurements is the spatial resolution of SICM for reaction mapping and delivery. This was explored using FEM simulations, with example results presented in Figure 4.7. For the conditions outlined above, Figure 4.7a shows a snapshot of the Dop^+ concentration around the pipette opening when the nanopipette was positioned 35 nm from the surface, before the reaction was driven. From this profile, we can see that at this separation distance, the high Dop^+ concentration is confined to the region directly beneath the pipette, suggesting the resolution of the technique is similar to the pipette dimensions. A profile of the Dop^+ concentration laterally along the substrate (z=0) is shown in Figure 4.7b for the case where the nanopipette was both at this approach distance (35 nm), as well as when it was at the retract distance (~10 µm from the surface). It can be seen that the region of the substrate underneath the pipette has the greatest Dop^+ concentration and so this is where the greatest change in ionic concentration owing to the reaction (by scanning the substrate potential) would occur. The profile, obtained where the tip

is 10 μm from the substrate reveals a much smaller concentration (max concentration of 0.01 mM) of Dop^+ present at the substrate surface and so very little dopamine oxidation signal should arise. Thus, 10 μm can be reasonably considered to be bulk solution. These profiles of surface Dop^+ concentration are beneficial for determining the lateral hopping distance that should be used in ΔC-SICM delivery experiments in order to ensure that each subsequent pixel has not been exposed to significant amounts of dopamine from the prior approach that may lead to fouling of the substrate during oxidation.[41]

This regime was repeated at a series of pixels to create a spatial array of nanopipette tip current-substrate potential data sets that were used to make videos of normalized nanopipette current in *x-y* space as a function of applied substrate potential. This maps the progress of the substrate reaction both spatially and with potential resolution. Snapshots from two movies at the extreme potential of +0.4 V *vs*. Ag/AgCl QRCE are shown in Figure 4.8, together with the simultaneously obtained topographical maps. Two scans were taken of different regions of the same CF. In the first, the probe contained only 80 mM KCl (control case), while in the second case the probe contained 50 mM KCl and 30 mM dopamine hydrochloride. In both experiments, the bulk solution contained 10 mM KCl (more dilute than the tip). Both of the topographical maps obtained during the imaging procedure (Figure 4.8a,d) suggest a diameter of 7-8 μm for the CF, consistent with the nominal value of 7 μm.

Both of the scans show a fairly homogeneous tip current response with the substrate potential at -0.1 V, corresponding to a condition where the oxidation of dopamine is switched off (Figure 4.8b,e). There is relatively little difference in the SICM response over the glass support and over the CF and a normalized current value approximating to 0.97 (the experimental set-point) is seen. However, with a potential of +0.4 V applied to the CF, dopamine oxidation occurs at a diffusion-controlled rate (bulk voltammetry shown in Supporting Information, Figure 4.16), and there is a clear difference between the scan in which dopamine is absent (Figure 4.8c) and the scan in which it is present in the nanopipette (Figure 4.8f). With dopamine present, the ionic current drops by a consistent 7-8% at each pixel across the surface of the CF.

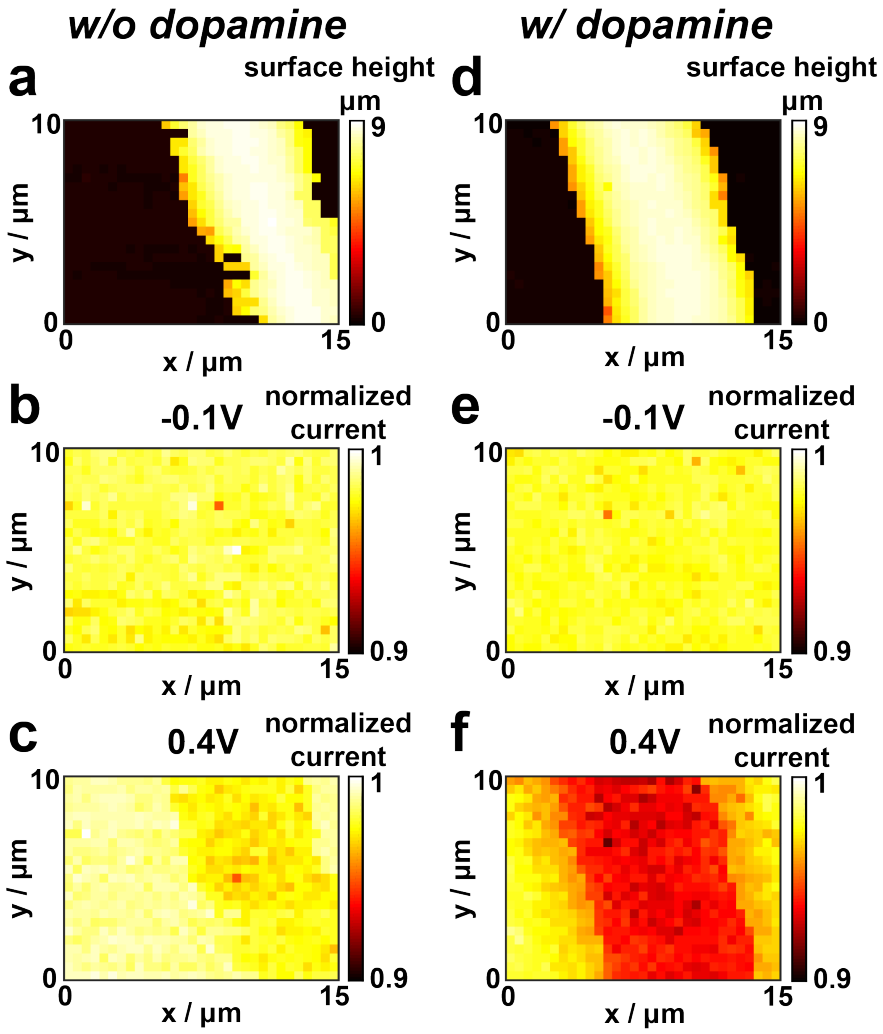

Figure 4.8. Reaction mapping over a CF electrode using ΔC-SICM, with a nanopipette containing (a-c) 80 mM KCl (control case) and (d-f) 50 mM KCl and 30 mM dopamine hydrochloride (pH 6.7). (a,d) Topographical maps of two different regions of the CF. (b,c,e,f) Individual frames taken from two videos of normalized nanopipette ionic current (in *x*,*y* as a function of substrate potential), either where no reaction occurred (-0.1 V: b,e) or at the substrate potential for dopamine oxidation (0.4 V: c,f). Each pixel corresponds to a particular approach of the nanopipette to the surface and there is no interpolation of data. Images contain 600 pixels.

This is because the substrate acts as an additional sink for Dop^+.[41] Whilst, a product of the Dop^+ electrooxidation is the release of protons,[29] which should enhance the conductivity of the gap, the majority of the resistance in SICM experiments comes from the nanopipette itself, and Dop^+ consumption depletes this

region, resulting in the decrease in the overall ionic current. This change in ionic current is also seen at the pixels surrounding the CF, a "diffusional broadening", caused by the sink-nature of the CF. A small decrease in the ionic current (1-2%) can also be seen over the surface of the CF for the control, suggesting that a small current is driven between the CF electrode and the QRCE in the probe. This is an interesting observation that could have future applications, but the effect is far less than with dopamine present. Thus ΔC-SICM can be used to map surface reactions at electrodes purely from the nanopipette ion current response.

4.5 Conclusions

In this study we have provided a full analysis of the electrochemical potentials in SICM, particularly pertinent to the case where different concentrations, or solution compositions, are employed in the nanopipette and bulk solutions. Through this analysis, we have demonstrated the versatility and advantages of using different ionic strength media in the SICM tip and bulk solution, in a mode we call ΔC-SICM. Notably, topographical imaging with a significantly reduced electric field than in conventional (applied bias) SICM becomes possible by driving the ionic current purely through the junction (diffusion) potential, that arises from the concentration gradient at the end of the pipette. Functional applications such as charge mapping with ΔC-SICM are more sensitive than conventional SICM with the charge sensitivity arising from significant EOF effects in this configuration. The model developed, which solves the Poisson, Nernst-Planck and Navier-Stokes equations with EOF, can also be applied to conventional SICM charge mapping measurements and allows for a more accurate determination of high surface charge densities than our previous approach. This work has expanded on the use of SICM for the delivery of charged molecules to a surface. One can envisage many applications where a nanopipette can be used for delivery and to measure the rate of delivery simply through the nanopipette current.

4.6 Supporting Information

4.6.1 SICM Pulsed-Potential Charge Mapping Regime: In previous studies, several different scan regimes have been employed to elucidate information about the surface charge of a substrate.[7,8,17,20,27]

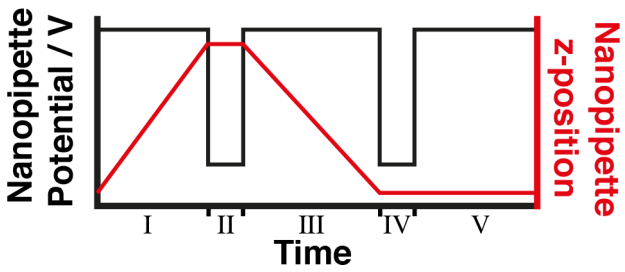

Figure 4.9. Schematic representation of the SICM pulsed-potential method for elucidating surface charge.

In this work, a pulse-potential regime was used, as represented in Figure 4.9.[8] The nanopipette was approached (I) towards the substrate with a fixed small SICM bias (either $E_{total} = E_{junction}$ or $E_{total} = \Delta E_{Electrode} + E_{junction}$). Upon detecting the surface via a decrease in the ionic current (see main text for typical tip-surface distances), the SICM bias was pulsed to a potential (II), where the ionic current became more sensitive to surface charge for a short, fixed time (typically 20 ms herein) before jumping back to the approach bias. The nanopipette was then retracted (III) away from the surface (typically 7 μm). When the nanopipette was far away from the surface an identical potential pulse was performed (IV). This provided a bulk current-voltage (*I-t)* curve to which the surface *I-t* curve could be normalized by taking an average of the last millisecond of each *I-t* curve. As outlined herein, this provided information about the surface charge properties. The probe was then moved laterally to the next *x*,*y* coordinate (pixel), holding the potential at the approach bias and keeping the *z* position constant (V).

4.6.2 FEM Simulation Details: Finite element method (FEM) simulations were constructed in COMSOL Multiphysics (v5.2a). A schematic of the FEM simulation domain is shown in Figure 4.10.

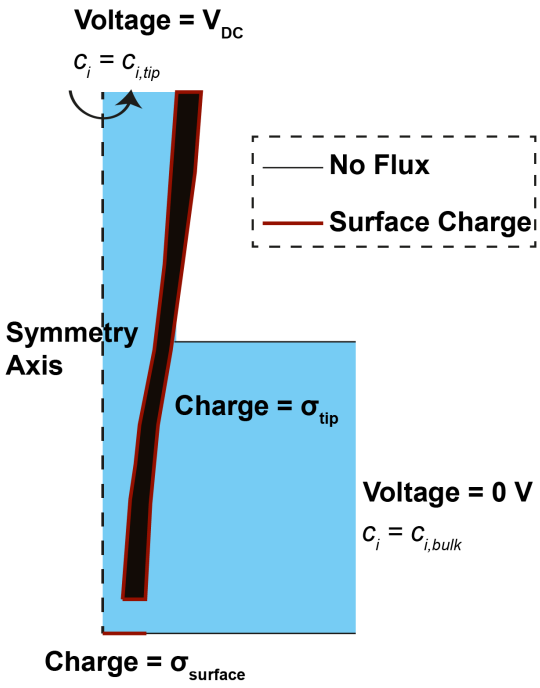

Figure 4.10. Schematic of FEM simulation domain with applied boundary conditions.

Typical dimensions of the nanopipettes used were extracted from TEM images and used to construct the nanopipette simulation domain. For simulations corresponding to the data in Figures 4.2-6, the species initially present in the simulations in the bulk domain were Na^+ (127 mM), K^+ (5 mM), Cl^- (108 mM) and HCO_3^- (24 mM) with 100-fold dilution in the tip. For simulations presented in Figure 4.7, K^+ (50 mM), Cl^- (80 mM), and Dop^+ (30 mM) were present in the nanopipette with K^+ (10 mM) and Cl^- (10 mM) initially present in the bulk domain. The electrostatics, transport of diluted species and laminar flow modules were used to model the experimental system. In all simulations the Nernst-Planck equation described ion transport (eq. 4.3):

$$J_i = -D_i \nabla c_i - z_i \frac{F}{RT} D_i c_i \nabla \phi \qquad (4.3)$$

where D_i z_i and c_i are the diffusion coefficients, charge number and concentrations of species i. Ion diffusion coefficients were taken from the CRC handbook[42] and the

simulations accounted for the effect of locally varying ionic strength in the simulations.[31] F, R and T are the Faraday constant, gas constant and absolute temperature. ϕ is the electric potential described by the Poisson equation (eq. 4.4):

$$\nabla^2\phi = -\frac{F}{\varepsilon\varepsilon_0}\sum_i z_i c_i \qquad (4.4)$$

where ε is the dielectric constant of the solution and ε_0 is the vacuum permittivity. The solution velocity was described by the incompressible Navier-Stokes equation with electroosmotic flow incorporated (eq. 4.5):

$$u\nabla u = \frac{1}{\rho}(-\nabla p + \mu\nabla^2 u - F(\sum_i z_i c_i)\nabla\phi) \qquad (4.5)$$

where ρ is the solution density, μ is the solution viscosity and p is the pressure. The molar volume was reasonably considered independent of ionic strength.[42]

Steady-state simulations were first performed for each of the experimental setups (high concentration tip or low concentration tip compared to bulk) to estimate the experimental working distance for functional measurements. These mimic the initial nanopipette approach curves (tip current versus distance). Simulations were performed at different probe-surface separations and the simulated approach curves compared to those obtained experimentally; see Figure 4.11 for typical examples for the surface charge mapping studies (a) and reaction mapping (b). From these, a working distance of 22 nm was obtained for surface charge mapping experiments (Figure 4.6), and 35 nm for reaction mapping experiments (Figure 4.8). Interestingly, in the reaction mapping configuration where a higher concentration was present in the nanopipette domain, the approach curve was much shallower and the nanopipette sensed the surface from a greater distance, (Figure 4.11b) whereas when the solution in the tip was more dilute (Figure 4.11a), a sharper approach was seen, despite the geometries being identical.

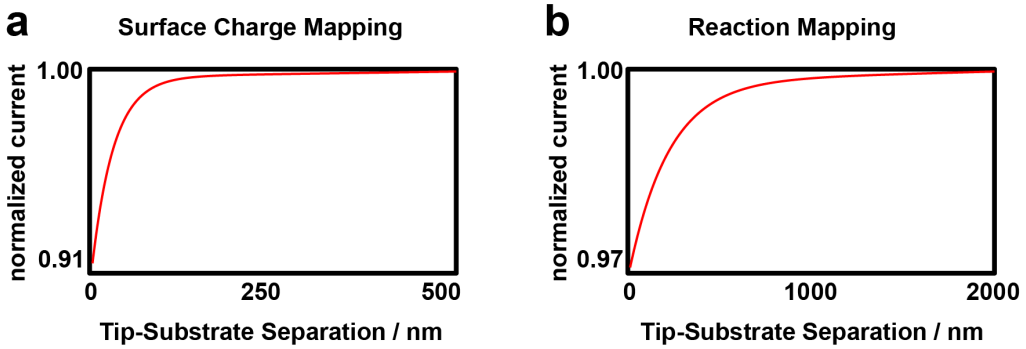

Figure 4.11. Simulated approach curves used to approximate experimental working distances for both surface charge (a) and reaction mapping (b) measurements.

4.6.3 Raw Current Data for Assessing EOF: Figure 4.4 in the manuscript shows the effect of EOF at a range of different surface charges on the normalized ionic current. Figure 4.12 shows the raw simulated currents in the case of conventional SICM (Figure 4.12a) and ΔC-SICM (Figure 4.12b). These currents are taken from *t* = 20 ms of the simulated time-dependent *I-t* pulse.

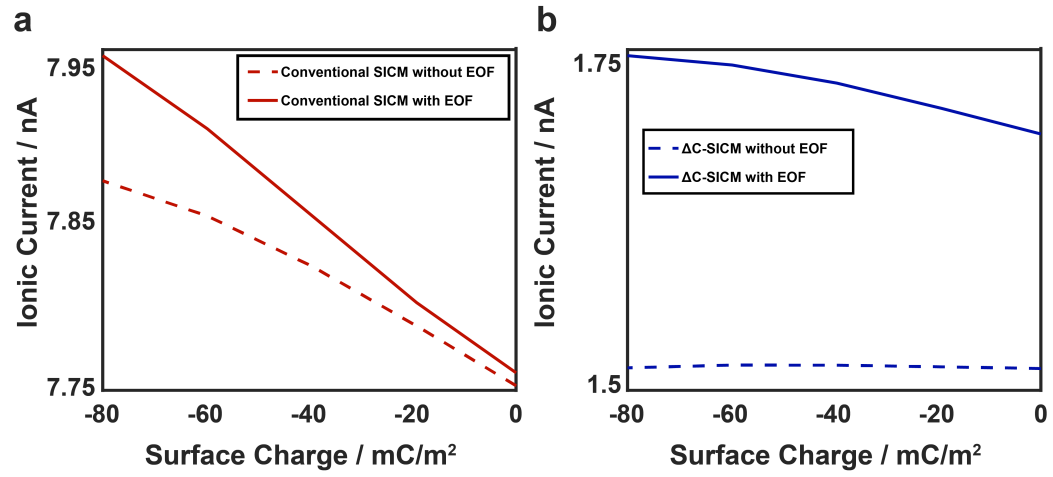

Figure 4.12. Raw currents corresponding to Figure 4.4 with the conventional SICM case shown in (a) and the ΔC-SICM case in (b).

4.6.4 Surface Charge Mapping with $E_{total} = \Delta E_{electrode} + E_{junction}$: Figure 4.13a shows an optical micrograph of several neuron-like PC12 cells that have undergone

spontaneous differentiation. These cells were imaged using ΔC-SICM with $E_{total} = \Delta E_{Electrode} + E_{junction} = -89$ mV for the nanopipette approach.

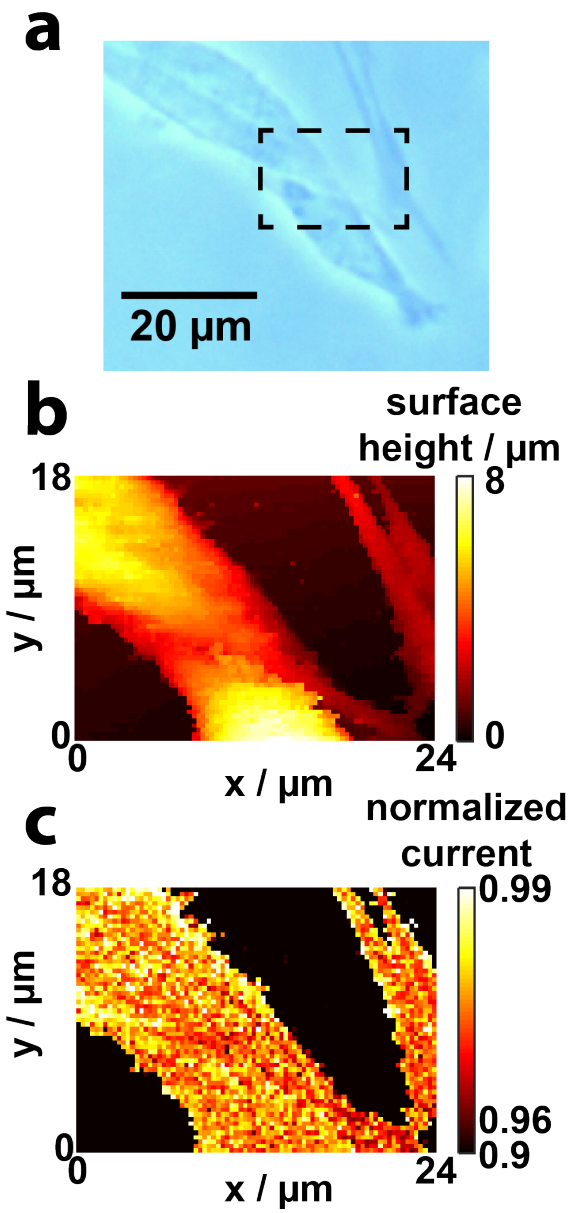

Figure 4.13. Surface charge mapping with $E_{total} = \Delta E_{electrode} + E_{junction}$. (a) Optical micrograph of PC12 cells on a glass substrate, scan area denoted by the black dashed rectangle. (b) Topographical map collected with a ~90 nm radius nanopipette using ΔC-SICM feedback. (c) Normalized current (defined in the text) map collected concurrently with the topography in (b).

The region scanned by ΔC-SICM is denoted by the black square and the topography from that scan is shown in Figure 4.13b. Several junctions can be identified between cells, notably between the two larger cells on the left-hand side of the scan, and in the bottom right of the image where two neurite-like protuberances are connected in what could potentially be a synapse. The normalized current map (Figure 4.13c) was collected at the same time as the topographical map in Figure 4.13b (see section 4.6.1 for definition of normalized current). The map in Figure 4.13c shows several heterogeneities in normalized current, an established proxy for surface charge density,[7,8] notably at the cellular junctions identified in the discussion of the topographical map above, with a clear region of lower normalized current along the divide between the two large cells on the left hand side of the image. This variation in localized charge could correspond to a higher density of certain proteins or lipids at the point where the two cells meet.

4.6.5 Quantifying Surface Charge: FEM simulations allowed normalized currents obtained experimentally in surface charge mapping experiments (Figure 4.6) to be converted to surface charge densities. Steady-state simulations were first performed with only the liquid junction potential as used for the initial approach of tip to the surface (topographical imaging). The results from these simulations were then used as initial conditions for time-dependent simulations where a potential of $E_{external}$ = -0.4 V was applied to the tip electrode and the SICM regime is more sensitive to surface charge. These simulations were repeated with different surface charge densities applied to the surface beneath the pipette. Simulations were also performed in bulk solution so that normalized currents corresponding to each surface charge density could be obtained. This allowed for a working curve (Figure 4.14b) to be generated was used to convert the experimental normalized current map (Figure 4.14a) to a map of surface charge densities (Figure 4.6c).

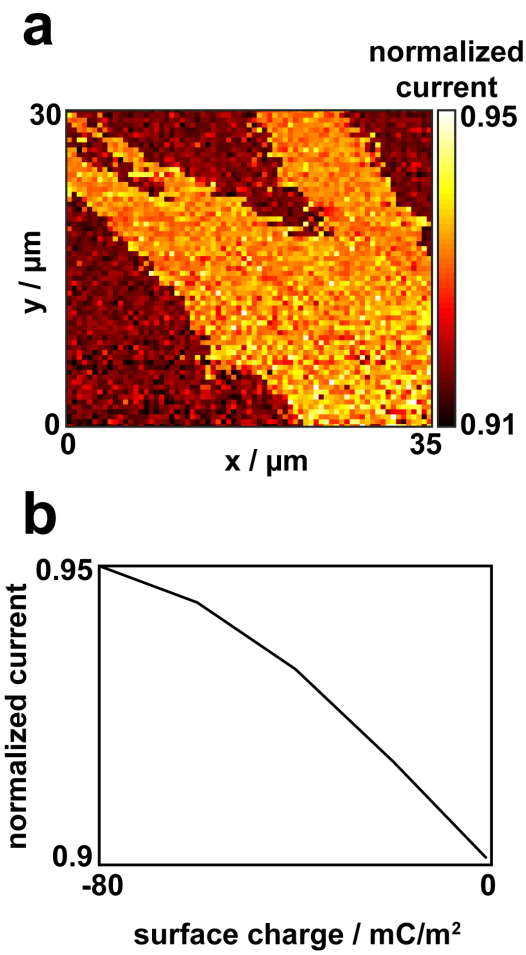

Figure 4.14. Conversion of raw data into surface charge density. (a) Experimental normalized currents obtained concurrently with the topography map in Figure 4.6b. (b) Simulated working curve to allow conversion of normalized current to surface charge density.

4.6.6 Schematic of Carbon Fiber Electrode Setup and Bulk Voltammetry: An optical micrograph of the CF electrode device on glass used as a substrate for reaction mapping is shown in Figure 4.15a, with a schematic of the setup shown in Figure 4.15b. Figure 4.16 shows a bulk substrate voltammogram performed in a 3-electrode set-up with the CF working electrode, a Pt counter electrode and a Ag/AgCl reference electrode. The solution contained 1 mM dopamine hydrochloride in 140 mM NaCl supporting electrolyte and 10 mM phosphate buffer and a scan rate of 100 mV/s was used.

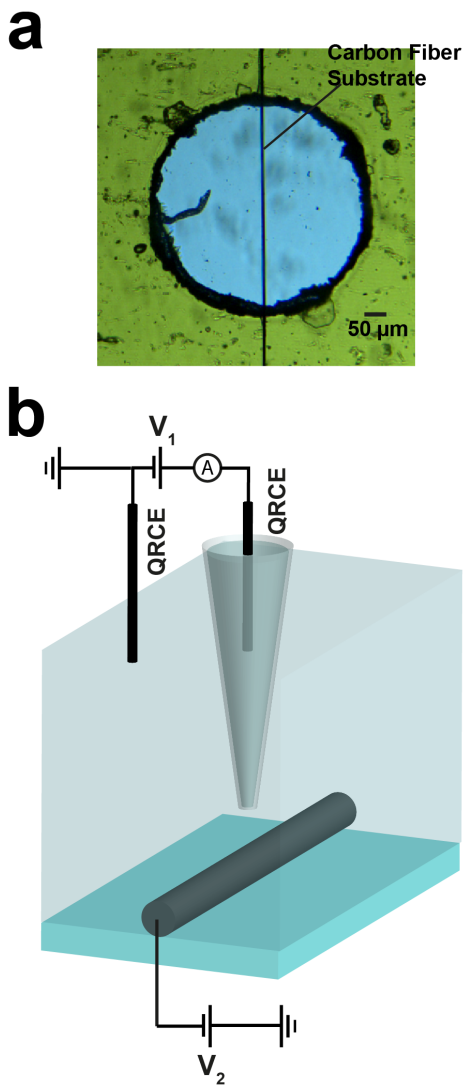

Figure 4.15. Setup for reaction mapping over an individual CF. (a) Optical micrograph of carbon fiber device used in SICM reaction mapping experiments. (b) Schematic of experimental setup with biases applied.

The ΔC-SICM reaction mapping setup was similar to that in the charge mapping experiments. However, the bias between the nanopipette and bulk electrode was held constant at $\Delta E_{Electrode} + E_{junction}$ = 26 mV. A CV was performed on the substrate CF electrode with a triangular scan of the potential from a value where dopamine oxidation did not occur (-0.1 V) up to 0.4 V and back to -0.1 V at a scan rate of 1 V/s. This profile was applied at each pixel, both with the nanopipette positioned near the substrate surface, and with the nanopipette in bulk solution. This allowed for nanopipette currents near the surface to be normalized to the nanopipette

response when in bulk solution as a function of substrate potential. Experiments were carried out with 30 mM dopamine hydrochloride and 50 mM KCl in the tip or with 80 mM KCl in the tip as a control.

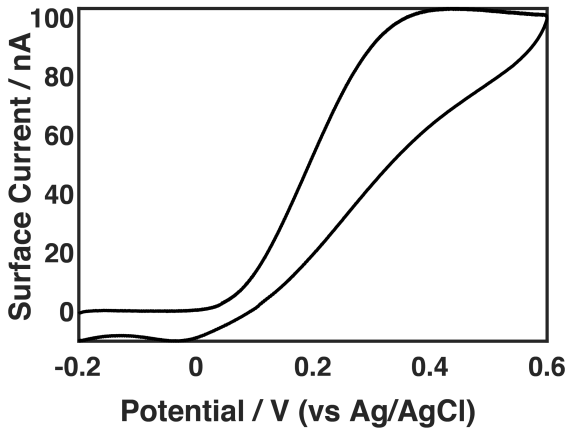

Figure 4.16. Voltammetry of the CF device in 1 mM dopamine hydrochloride with 140 mM NaCl supporting electrolyte with 10 mM phosphate buffer. A Ag/Ag/Cl reference electrode was used and a Pt wire served as the counter electrode. The scan rate was 100 mV/s.

4.7 References

(1) Hansma, P. K.; Drake, B.; Marti, O.; Gould, S. A.; Prater, C. B. *Science* **1989**, *243*, 641–643.

(2) Chen, C.-C.; Zhou, Y.; Baker, L. A. *Annu. Rev. Anal. Chem.* **2012**, *5* (1), 207–228.

(3) Korchev, Y. E.; Bashford, C. L.; Milovanovic, M.; Vodyanoy, I.; Lab, M. J. *Biophys. J.* **1997**, *73* (2), 653–658.

(4) Korchev, Y. E.; Milovanovic, M.; Bashford, C. L.; Bennett, D. C.; Sviderskaya, E. V; Vodyanoy, I.; Lab, M. J. *J. Microsc.* **1997**, *188* (1), 17–23.

(5) Novak, P.; Li, C.; Shevchuk, A. I.; Stepanyan, R.; Caldwell, M.; Hughes, S.; Smart, T. G.; Gorelik, J.; Ostanin, V. P.; Lab, M. J.; Moss, G. W. J.; Frolenkov, G. I.; Klenerman, D.; Korchev, Y. E. *Nat. Methods* **2009**, *6* (4), 279–281.

(6) Gorelik, J.; Zhang, Y.; Shevchuk, A. I.; Frolenkov, G. I.; Sánchez, D.; Lab, M. J.; Vodyanoy, I.; Edwards, C. R. W.; Klenerman, D.; Korchev, Y. E. *Mol.*

Cell. Endocrinol. **2004**, *217* (1–2), 101–108.

(7) Perry, D.; Paulose Nadappuram, B.; Momotenko, D.; Voyias, P. D.; Page, A.; Tripathi, G.; Frenguelli, B. G.; Unwin, P. R. *J. Am. Chem. Soc.* **2016**, *138* (9), 3152–3160.

(8) Page, A.; Perry, D.; Young, P.; Mitchell, D. A.; Frenguelli, B. G.; Unwin, P. R. *Anal. Chem.* **2016**, *88* (22), 10854–10859.

(9) Kang, M.; Momotenko, D.; Page, A.; Perry, D.; Unwin, P. R. *Langmuir* **2016**, *32*, 7993–8008.

(10) Page, A.; Perry, D.; Unwin, P. R. *Proc. R. Soc. A* **2017**, *473*, 20160889.

(11) Chen, C.-C.; Baker, L. A. *Analyst* **2011**, *136* (1), 90–97.

(12) McKelvey, K.; Perry, D.; Byers, J. C.; Colburn, A. W.; Unwin, P. R. *Anal. Chem.* **2014**, *86* (7), 3639–3646.

(13) Li, P.; Liu, L.; Yang, Y.; Zhou, L.; Wang, D.; Wang, Y.; Li, G. *J. Lab. Autom.* **2015**, *20* (4), 457–462.

(14) Takahashi, Y.; Murakami, Y.; Nagamine, K.; Shiku, H.; Aoyagi, S.; Yasukawa, T.; Kanzaki, M.; Matsue, T. *Phys. Chem. Chem. Phys.* **2010**, *12* (34), 10012–10017.

(15) Yang, X.; Liu, X.; Zhang, X.; Lu, H.; Zhang, J.; Zhang, Y. *Ultramicroscopy* **2011**, *111* (8), 1417–1422.

(16) Momotenko, D.; McKelvey, K.; Kang, M.; Meloni, G. N.; Unwin, P. R. *Anal. Chem.* **2016**, *88* (5), 2838–2846.

(17) Perry, D.; Al Botros, R.; Momotenko, D.; Kinnear, S. L.; Unwin, P. R. *ACS Nano* **2015**, *9* (7), 7266–7276.

(18) Klausen, L. H.; Fuhs, T.; Dong, M. *Nat. Commun.* **2016**, *7*, 12447.

(19) Page, A.; Kang, M.; Armitstead, A.; Perry, D.; Unwin, P. R. *Anal. Chem.* **2017**, *89* (5), 3021–3028.

(20) McKelvey, K.; Kinnear, S. L.; Perry, D.; Momotenko, D.; Unwin, P. R. *J. Am. Chem. Soc.* **2014**, *136* (39), 13735–13744.

(21) Schobesberger, S.; Jönsson, P.; Buzuk, A.; Korchev, Y.; Siggers, J.; Gorelik, J. *Biophys. J.* **2016**, *110* (1), 141–146.

(22) Momotenko, D.; Page, A.; Adobes-Vidal, M.; Unwin, P. R. *ACS Nano* **2016**, *10* (9), 8871–8878.

(23) Bruckbauer, A.; Ying, L.; Rothery, A. M.; Zhou, D.; Shevchuk, A. I.; Abell,

C.; Korchev, Y. E.; Klenerman, D. *J. Am. Chem. Soc.* **2002**, *124* (30), 8810–8811.

(24) Rodolfa, K. T.; Bruckbauer, A.; Zhou, D.; Korchev, Y. E.; Klenerman, D. *Angew. Chem., Int. Ed.* **2005**, *44* (42), 6854–6859.

(25) Ying, L.; Bruckbauer, A.; Rothery, A. M.; Korchev, Y. E.; Klenerman, D. *Anal. Chem.* **2002**, *74* (6), 1380–1385.

(26) Edwards, M. A.; Williams, C. G.; Whitworth, A. L.; Unwin, P. R. *Anal. Chem.* **2009**, *81* (11), 4482–4492.

(27) Sa, N.; Lan, W. J.; Shi, W.; Baker, L. A. *ACS Nano* **2013**, *7* (12), 11272–11282.

(28) Harreither, W.; Trouillon, R.; Poulin, P.; Neri, W.; Ewing, A. G.; Safina, G. *Anal. Chem.* **2013**, *85* (15), 7447–7453.

(29) Patel, A. N.; Tan, S. Y.; Miller, T. S.; Macpherson, J. V.; Unwin, P. R. *Anal. Chem.* **2013**, *85* (24), 11755–11764.

(30) Takahashi, Y.; Ito, K.; Wang, X.; Matsumae, Y.; Komaki, H.; Kumatani, A.; Ino, K.; Shiku, H.; Matsue, T. *Electrochemistry* **2014**, *82*, 331–334.

(31) Perry, D.; Momotenko, D.; Lazenby, R. A.; Kang, M.; Unwin, P. R. *Anal. Chem.* **2016**, *88* (10), 5523–5530.

(32) Al-Sakere, B.; André, F.; Bernat, C.; Connault, E.; Opolon, P.; Davalos, R. V; Rubinsky, B.; Mir, L. M. *PLoS One* **2007**, *2* (11), e1135.

(33) Davalos, R. V; Rubinsky, B. Tissue ablation with irreversible electroporation, 2004.

(34) Miklavčič, D.; Beravs, K.; Šemrov, D.; Čemažar, M.; Demšar, F.; Serša, G. *Biophys. J.* **1998**, *74* (5), 2152–2158.

(35) Das, K. P.; Freudenrich, T. M.; Mundy, W. R. *Neurotoxicol. Teratol.* **2004**, *26* (3), 397–406.

(36) Bard, A. J.; Faulkner, L. R. *Electrochemical Methods: Fundamentals and Application*; Wiley, 1980.

(37) White, H. S.; Bund, A. *Langmuir* **2008**, *24* (5), 2212–2218.

(38) Momotenko, D.; Cortes-Salazar, F.; Josserand, J.; Liu, S.; Shao, Y.; Girault, H. H. *Phys. Chem. Chem. Phys.* **2011**, *13*, 5430–5440.

(39) Babakinejad, B.; Jönsson, P.; López Córdoba, A.; Actis, P.; Novak, P.; Takahashi, Y.; Shevchuk, A.; Anand, U.; Anand, P.; Drews, A.; Ferrer-

Montiel, A.; Klenerman, D.; Korchev, Y. E. *Anal. Chem.* **2013**, *85* (19), 9333–9342.

(40) Bath, B. D.; Michael, D. J.; Trafton, B. J.; Joseph, J. D.; Runnels, P. L.; Wightman, R. M. *Anal. Chem.* **2000**, *72* (24), 5994–6002.

(41) Patel, A. N.; McKelvey, K.; Unwin, P. R. *J. Am. Chem. Soc.* **2012**, *134* (50), 20246–20249.

(42) Haynes, W. M. *CRC Handbook of Chemistry and Physics*; CRC press, 2014.

5 Write-Read 3D Patterning with a Dual-Channel Nanopipette

With a setup that combines the dual-channel approach of Chapter 2 with the single open-barrel techniques in Chapters 3 and 4, this chapter adds functionality to the conventional SICM setup via the use of a dual-channel theta pipette. One channel is used to deliver copper ions to a surface while the other is used to track the deposition and retract the probe simultaneously. The parameters of deposition (such as the delivery and substrate biases) are optimized and the deposition of simple (pillar) and complex (zig-zag) nanoscale structures is demonstrated. The multifunctional flexibility of SICM is shown by the use of the same nanopipette probe to map the topography of a deposition immediately after it has been deposited.

The programmatic design of the two-channel deposition was done by the author, while Dr. Dmitry Momotenko carried out the experiments. All electron microscopy herein was performed by Dr. Momotenko and Dr. Maria Adobes-Vidal. Dr. Momotenko wrote the manuscript, with input from the author.

Write-Read 3D Patterning with a Dual-Channel Nanopipette

Dmitry Momotenko,[1,] Ashley Page,[1,2] Maria Adobes-Vidal[1] and Patrick R. Unwin[1,*]*

[1]Department of Chemistry and [2]MOAC Doctoral Training Centre, University of Warwick, Coventry, CV4 7AL, United Kingdom

*corresponding authors

p.r.unwin@warwick.ac.uk

d.momotenko@warwick.ac.uk

5.1 Abstract

Nanopipettes are becoming extremely versatile and powerful tools in nanoscience for a wide variety of applications from imaging to nanoscale sensing. Herein, the capabilities of nanopipettes to architect and build complex free-standing three-dimensional (3D) nanostructures are demonstrated using a simple double-barrel nanopipette device. Electrochemical control of ionic fluxes enables highly localized delivery of precursor species from one channel, and simultaneous (dynamic and responsive) ion conductance probe-to-substrate distance feedback with the other, for reliable high-quality patterning. Nanopipettes with 30–50 nm tip opening dimensions of each channel allowed confinement of ionic fluxes for the fabrication of high aspect ratio copper pillars, zigzag and Γ-like structures, as well as permitting the subsequent topographical mapping of the patterned features with the *same nanopipette probe* as used for nanostructure engineering. This approach offers versatility and robustness for high resolution 3D "printing" (writing) and read-out at the nanoscale.

5.2 Introduction

Three-dimensional (3D) micro- and nanostructures can offer unique and intriguing physical and optical properties that find applications in numerous research and technology disciplines spanning electronics,[1] sensing and analysis,[2] biotechnology and biomedicine,[3] tissue engineering,[4] nanoscale motion devices[5] and many others. The fabrication of 3D objects with a high degree of control over shape and size, however, still presents many challenges. Techniques that enable 3D patterning

include template methods[6,7] (typically, lithography followed by an appropriate way of filling cavities in a resist, *e.g.* electroplating, physical or chemical vapour deposition *etc.*), electron- and ion beam-induced structuring[8,9] that allow modification of surfaces using precursors from gas or liquid phases, self-assembly (based on, for instance, DNA strains as building blocks[10] or DNA origami[11]) and scanning probe microscopy (SPM) methods. The family of SPM techniques offers powerful capabilities for the direct manipulation of matter at the tip of the probe, and on the fabricated object, with no need for a mask or template. This opens up single step processing, without post-fabrication operations on the patterned structures, as well as providing high versatility, as SPMs enable operation in gas and liquid environments and under vacuum.[12] Surface modification with SPMs is possible in many different ways, including the manipulation of "building blocks" such as nanoparticles,[13,14] deposition in a layer-by-layer fashion,[15] local removal of material by scratching or thermal desorption,[16] modification of local environment using ultramicroelectrodes,[17–19] or confined delivery using, for example, micro- and nanopipette probes.[1,13,20–31] Approaches using multiplexed probes, such as microelectrode arrays,[32] multiple cantilevers for atomic force microscopy (AFM)[33,34] and dip-pen lithography,[35] for high-throughput patterning have also been developed, which offer great opportunities to speed up probe-based fabrication processes.

Nanopipettes are particularly useful tools in nanoscience as they allow the precise spatiotemporal control, analysis and manipulation of material fluxes.[36,37] Most recently nanopipettes have proven powerful as probes for multifunctional imaging, as exemplified by simultaneously mapping topography and reactivity,[36,38,39] and for probing heterogeneously distributed surface charge magnitudes alongside topography.[40–42] We develop this multifunctional capability herein, demonstrating 3D writing and reading with nanopipette probes.

For nanofabrication purposes, nanopipettes filled with electrolyte can serve as a local reservoir of desired molecules/ions for deposition and can therefore provide a highly localized flux of species towards the substrate. Nanopipettes enable surface modification both in electrolyte solution[22,23,27] and in a scanning droplet cell configuration,[21,43,44] and the deposition of metals from precursors and nanoparticle dispersions has been shown for the fabrication of complex planar and 3D features at interfaces.[1,13,24,25,30,45,46] However, the main difficulty in fabricating arbitrary 3D

shapes is the issue of controlling the probe-to-substrate distance during deposition (positional feedback). This is a crucial aspect, as it affects the quality of the deposited structures. Recently, these issues were addressed by the implementation of hollow microfluidic AFM cantilevers, so-called FluidFM probes,[47] which enabled the microscale fabrication of complex 3D objects by electroplating copper. The deposition occurred under the aperture of an AFM tip with simultaneous force control of tip-to-substrate distance, as well as accurate regulation of electrolyte flow by physically flowing solution through the hollow AFM tip.[48,49]

Herein, we demonstrate the deposition of complex high aspect ratio objects using simultaneous electrochemical delivery and distance control, with a simple dual-barrel nanopipette probe. This approach to 3D patterning achieves higher resolution than presently possible with AFM devices, and is accomplished without any need for flow systems. In addition, nanopipette probes allow the read-out of the resulting patterns using the topographical mapping capabilities of scanning ion conductance microscopy (SICM)[50,51] with the same dual probe.

5.3 Materials and Methods

5.3.1 Chemicals: Sodium sulfate (anhydrous, analytical grade, Fisher Scientific), copper sulfate (technical grade, Fisons Scientific Equipment) and sulfuric acid (≥95%, density 1.83 g ml^{-1}, analytical reagent grade, Fisher Scientific,) were used as received. Deionized (DI) water produced by Purite Select HP system, with resistivity 18.2 MΩ cm (25 °C) was used to prepare aqueous solutions. Electrolyte solution in the bulk and in the SICM pipette barrel contained Na_2SO_4 (0.5 M) and H_2SO_4 (3 mM), while the nanopipette barrel used as a source of copper ions (Cu^{2+}) was filled with $CuSO_4$ (56 – 270 mM) and H_2SO_4 (3 – 100 mM).

5.3.2 Nanopipette Probes: Nanopipettes were pulled from dual-barrel quartz capillaries with filament (QTF120-90-100, Friedrich & Dimmock) using a laser pipette puller (P-2000, Sutter Instruments). Nanopipette probes were filled with electrolyte solutions using syringes with Microfill capillaries MF34G-5 (World Precision Instruments). Importantly, the nanopipette filling process does not cause significant cross-contamination between the different electrolytes in the nanopipette barrels (from a small liquid droplet that can form at the tip) to any significant level

(see Supporting Information, section 5.6.1). Geometric characterization of nanopipette probes was carried out on either gold-coated pipette tips imaged with a field-emission scanning electron microscope (FE-SEM, Zeiss SUPRA 55 VP) or on uncoated nanopipette tips, with geometries determined at high resolution[52,53] using a transmission electron microscope (TEM) JEOL 2000FX at 200 kV accelerating voltage.

5.3.3 Scanning Ion Conductance Microscopy (SICM) Setup: Nanopipette probes, mounted on a custom made probe holder, were coarsely positioned over a sample with a mechanical micropositioner (Newport, M-461-XYZ-M) under control of a 3 megapixel digital camera (PixeLink PL-B776U) with a 4X magnification lens. A 38 μm-range single axis nanopositioner (Physik Instrumente, P-753.3CD) was used for precise control and translation of the probe in the vertical (z) direction (normal to the substrate). A small vertical oscillation of the probe (40 nm peak-to-peak) at a frequency typically in the range 270 – 290 Hz was applied using a lock-in amplifier (Stanford Research Systems, SR830). This induced an alternating current (AC), the magnitude of which served as positional feedback (distance-modulated SICM).[54,55] In general, AC-SICM techniques provide very stable probe positioning.[54,55] The sample, 60 nm gold thin film on 3 nm chromium layer deposited on silicon wafer, with an exposed to electrolyte solution surface area of about 3 mm^2, was biased using a custom built bipotentiostat. The sample was mounted on the stage of an inverted microscope equipped with a high-precision XY nanopositioning piezoelectric stage (MadCityLabs, Nano-Bio300 and Physik Instrumente, model P-733.2DD). The setup was mounted inside a faraday cage (to reduce electrical noise), which was built on an optical table (Newport, RS 2000) to avoid mechanical vibrations. To reduce thermal drift of the piezoelectric positioners, vacuum insulating panels (Kevothermal) and aluminium heat sinks were mounted inside the faraday cage. Electrochemical measurements were performed with a custom-built bipotentiostat equipped with a high sensitivity current follower to measure nanopipette probe currents from both channels. The SICM setup was controlled through an FPGA card (PCIe-7852R, National Instruments) using a home-written program in a LabVIEW interface that was also used for all data acquisition.

5.4 Results and Discussion

5.4.1 Operational Principle: High quality 3D patterning at an interface with a probe-based technique requires simultaneous responsive control of the probe-to-substrate distance and accurate on-demand delivery of material to the substrate. This can be implemented by using a dual-barrel nanopipette in which one of the nanopipette barrels is a local source of precursor material while the other is used for local ion conductance measurements in an SICM setup, providing feedback for precise probe positioning.[50,51] Herein, this concept is demonstrated for the electrodeposition of copper structures using the setup shown in Figure 5.1a. This configuration allows: i) independent control of electrochemical potential on the gold thin film substrate for copper plating (or stripping, if desired) via E_{sub} and V_{ref}; ii) regulation of ion flow through the SICM nanopipette barrel, used for distance feedback and induced by the potential difference, V_{ref}, between the quasi-reference counter electrodes (QRCEs) in the nanopipette and solution bulk; and iii) management of the Cu^{2+} ion flux through the other nanopipette barrel, determined by the applied bias value ($V_{delivery}$-V_{ref}) to the QRCE in the pipette, used for local delivery of precursor species. Importantly, the applied potentials in this setup are controlled independently and simultaneously (with the aid of specifically designed LabVIEW code in combination with the hardware), and all the potentials are reported with respect to the QRCE in the solution bulk. In this way, for the engineering of 3D features at interfaces, there is very fine control of the deposition rate (via both the applied substrate potential and regulation of the Cu^{2+} flow current by the applied bias), coupled with the maintenance of a constant probe-to-substrate distance, enabling automatic probe retract as a feature grows, ensuring high quality patterning. SICM feedback was induced by a constant DC bias (in the range ±0.2 V, except for the example shown in Figure 5.3a where the SICM bias was set to -0.25 V, *vide infra*). The possibility to control the nanopipette bias polarity could be beneficial for the technique operation, for example to prevent the nanopipette tip from clogging, although this is not the case for copper deposition exemplified herein.

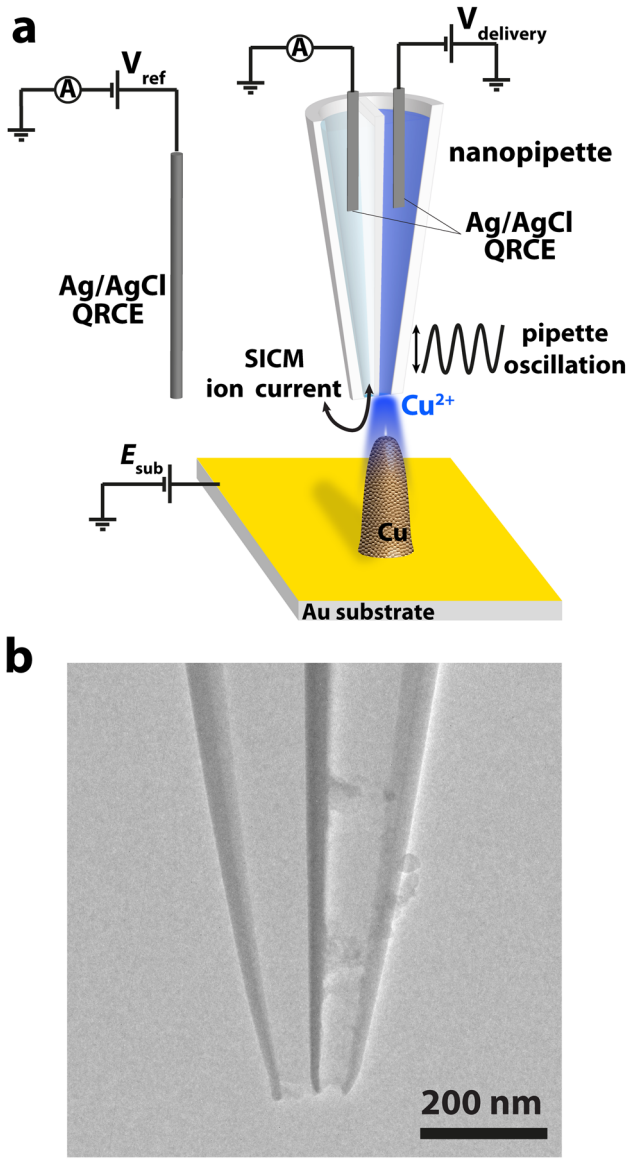

Figure 5.1. Setup and probe used for copper deposition. (a) Schematic representation of the experimental setup employed for deposition of 3D high aspect ratio Cu features on a gold electrode surface. (b) TEM image of a typical dual-barrel nanopipette probe used for nanoscale patterning with SICM positional feedback.

An important attribute of nanopipette methods is the simplicity and the low cost of probe fabrication, especially when compared to probe manufacture for other SPMs: pulling capillaries with diameters that are highly tuneable, and range from tens of microns down to a few nanometers is a simple and routine task, that does not require any special facilities (except a laser pipette puller). This is an important consideration, as the size of the nanopipette probe is a factor determining both the mass transport rates through the nanopipette orifice[52] and the lateral dimensions of

the deposit; the smaller the probe, the higher the confinement of the reagent flow and thus the smaller the lateral dimension of the patterned feature. Figure 5.1b is a TEM image of a typical dual-barrel nanopipette employed herein for patterning of high-aspect ratio copper structures. The overall pipette tip diameter (taking into account the thickness of glass walls that reaches 14 nm at the tip) is about 120 nm, whereas the opening dimensions of each of the nanopipette barrels are around 30 – 50 nm. This is about an order of magnitude smaller than the opening size of FluidFM probes (300 nm – 1 μm) recently employed for patterning of free-standing 3D copper microstructures.[49]

5.4.2 Patterning: Figure 5.2 demonstrates the evolution of probe position as well as DC ion current and AC amplitude (used as feedback) during a typical deposition experiment used to produce a Cu tower on a substrate. Prior to patterning, the nanopipette approaches the gold substrate (region marked "I" in Figures 5.2a and b) until the AC amplitude (due to the oscillation of the probe normal to the substrate) reaches a specified feedback set point (1.5 pA in the case of Figure 5.2), indicating close proximity of the probe to the sample interface; see Materials and Methods section. During the approach the pipette barrel that contains Cu^{2+} ions is biased at a slightly negative potential (value between -0.1 to -0.3 V) to ensure minimum precursor (Cu^{2+}) flux towards the substrate. As the nanopipette reaches the approach set point, typically corresponding to a distance of slightly more than the nanopipette opening radius from the interface, the bias at the QRCE in the precursor-containing probe barrel is changed to a certain positive value (with respect to QRCE in solution bulk), driving copper ions through the nanopipette opening for local delivery. A sudden change of ion flux in the probe-to-substrate gap due to the rapid switch in bias causes a spike in both the DC and AC ion current through the barrel employed for SICM distance control, leading to the fast retract of the pipette by a few hundred nanometers (at a time of ca. 35 s in the region marked "II" in Figures 5.2a and b) before reapproaching to the set point distance as the current spike flattens out. After this short period (usually, a few hundreds of ms long), positional feedback stabilizes the probe above the substrate (also during region "II"). As the deposition process starts, promoted by the bias applied to the substrate electrode (*vide infra*), SICM automated positioning maintains a constant probe-to-substrate distance by a slow

retract of the probe due to the feature growth underneath the nanopipette orifice (Figures 5.2a and b, marked "III").

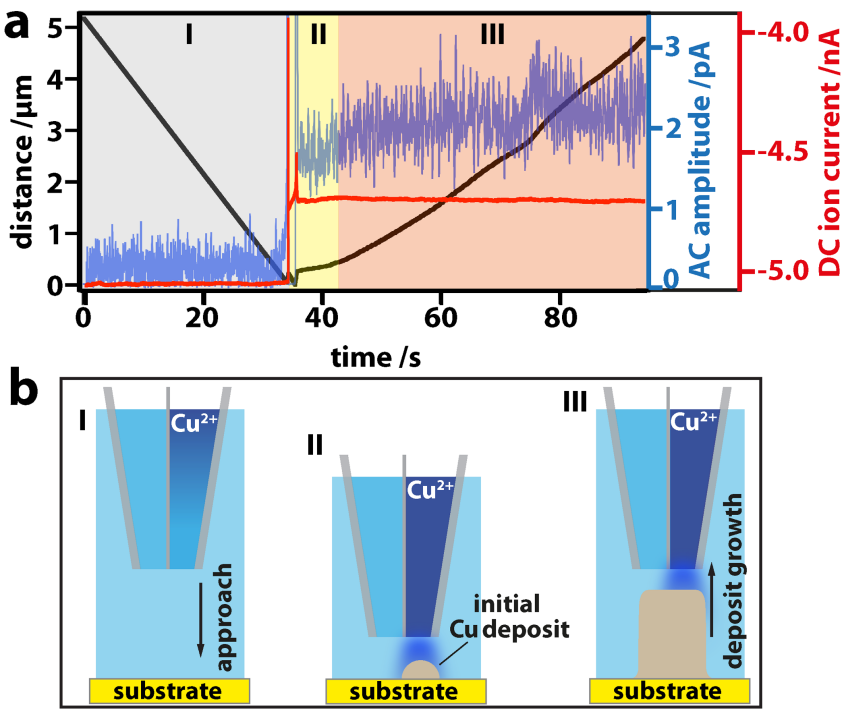

Figure 5.2. Typical z-position and current profiles during a deposition. (a) Variation with time of the probe vertical position (black), pipette AC and DC ion currents (for the barrel employed for distance control; blue and red, respectively) during the growth of a Cu pillar on a gold substrate. The data reveal the following: (I) approach of the probe to the substrate at a rate of 150 nm s^{-1} (negative bias of -0.2 V applied to the pipette barrel containing Cu^{2+}) with a stable (bulk) DC ion current (SICM bias -0.2 V) and zero AC amplitude. (II) The DC current shows a steep decline over a distance of ~200 nm inducing an increase in AC amplitude. Having reached the AC amplitude set point there is commencement of the deposition of an initial ~100 nm section of the Cu pillar following a switch of the Cu^{2+} delivery channel to 1 V. (III) Growth of the deposit in the vertical direction with the AC amplitude maintained slightly above 1.5 pA and the DC ion current value being consistent for the whole duration of the deposition. The probe retracts from the surface as the Cu pillar grows and the rate of tip movement is the growth rate. Note that the images are not to scale (*i.e.* the deposit under the nanopipette is usually 10 times larger than the opening size of a channel in the nanopipette). The color code on the ordinate axes corresponds to the line colors on the graph. Schematic illustrations in (b) depict the position of the pipette with respect to substrate and the growing deposit feature during patterning.

Figure 5.3a demonstrates the importance of the substrate potential, E_{sub}, on the patterning quality. Herein, the substrate was held at a constant potential throughout the entire experimental routine, from the initial probe approach and until the end of the deposition. However, it would be possible to vary the substrate potential during depositions without significant influence on the feedback (unless the potential was stepped sharply to another value, that could cause a spike in the DC and AC pipette currents and hence a retraction of the pipette for a short period of time due to the feedback mechanism). Typically, copper deposition starts at about -0.3 to -0.4 V *vs*. Ag/AgCl QRCE. However, at a low deposition overpotential (-0.4 V) the kinetics of deposition is sluggish and so the collection of the delivered Cu^{2+} ions at the substrate occurs over a large substrate area leading to rather unconfined electrodeposition, from which 3D features evidently cannot be constructed on this timescale. At larger electroplating driving forces (E_{sub} = -0.5 to -0.7 V) the patterns start exhibiting more pillar-like structures as the increased overpotential significantly enhances the local deposition rate leading to a more confined collection of the precursor (Cu^{2+} reduction to Cu) at the substrate directly underneath the nanopipette probe. The increase of the substrate overpotential, E_{sub}, also results in a faster growth of the features; the deposition rate gradually increases from an average of ~2 nm s^{-1} (-0.4 V) to 21 nm s^{-1} (-0.5 V) and then to 29 and 66 nm s^{-1} (-0.6 and -0.7 V, respectively), allowing the construction of taller pillars within the fixed deposition time considered (180 s). These data highlight that for a given Cu^{2+} flux from the nanopipette, the substrate potential ultimately determines the upper limit of the deposition rate, which otherwise is controlled by the magnitude of Cu^{2+} flow to the substrate (determined by the bias value applied to the QRCE in the nanopipette delivery channel). Importantly, the diffusional flux (0 V bias applied to the copper-containing barrel) does not provide sufficiently high mass transport of Cu^{2+} towards the substrate and therefore does not result in the deposition of features (at least, within a timescale considered). At larger driving potential, the migration of ions in the electric field dominates the mass transport and can result in much higher deposition rates and taller pillars (Figure 5.3a). Furthermore, the flux of Cu^{2+} ions can be controlled by the precursor concentration: the higher the concentration of Cu^{2+} in the electrolyte, the lower the bias value required to drive the flow of Cu^{2+}

towards the substrate at a given rate. The overall quality of the deposits (feature thickness, shape and roughness) appears consistent under inspection by SEM and is not significantly influenced by the bias value that drives Cu^{2+} through the pipette opening at a constant E_{sub}, at least for this range of bias magnitudes. The substrate potential evidently has most effect on feature growth, controlling the electrochemical kinetics of deposition and to some extent leading to a small variation of feature thickness (similar to deposition with FluidFM probes),[48] while the mass transport of Cu^{2+} ions from the nanopipette is mainly controlled by the bias on the QRCE in the delivery barrel.

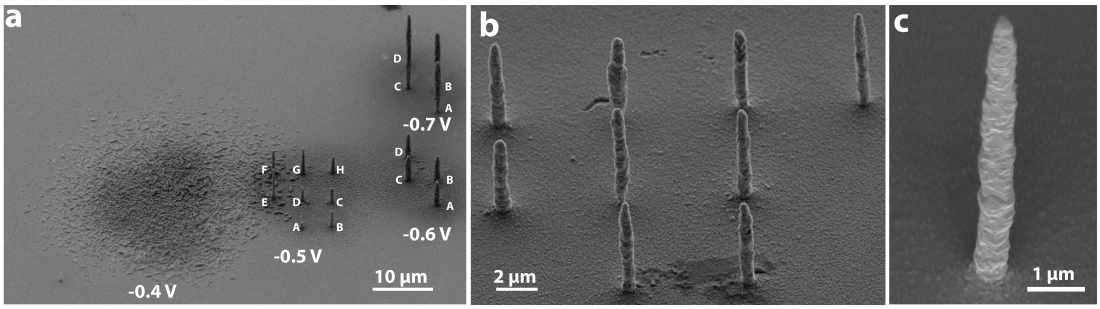

Figure 5.3. SEM micrographs (taken at a 45° inclination angle) of copper pillars patterned on gold substrates. (a) The effect of the substrate potential on deposition. Features at substrate potentials of -0.4 V and -0.5 V contained eight depositions, while arrays grown at E_{sub} = -0.6 V and E_{sub} = -0.7 V consisted of four individual pillars. The bias in the $CuSO_4$-filled barrel was between 0.3 V and 1V for substrate potentials of -0.4 V and -0.5 V (marked from "A" to "H") and from 0.8 to 1.1 V (in 0.1 V increments, "A" to "D") for substrate potentials of -0.6 V and -0.7 V. The SICM bias was fixed at -0.25 V and the deposition time was set to 180 s. (b) An array of nine pillars deposited at E_{sub} = -0.75 V, SICM bias 0.2 V and the bias in a copper reservoir barrel of 1 V. Deposition time was set to 60 s. (c) A magnified view of one of the pillars, deposited under similar conditions as in (b), except that the bias value in the copper-containing pipette barrel was 1.2 V.

Under the conditions used herein (*i.e.* acidic electrolyte, high salt concentrations) the ion fluxes through the nanopipette follow ohmic behaviour, rather than diode-like characteristics. This is attributed to the fact that ion current rectification,[56] which is related to surface charge on the conical nanopipette inner walls,[57] is weak as the silanol groups (pK_a around 4.5 and 8.5) on the glass/quartz

surface are protonated (neutral charge) as the electrolyte pH is around 2-3, and the rectification effect is further diminished by the high salt concentration (small Debye length).[40]

Figure 5.3b illustrates the reproducibility of fabrication, showing a set of 9 pillars deposited at different regions of a gold substrate. A deposition rate of 115 nm s^{-1} was reasonably consistent within this set (relative standard deviation of 12%). An electron microscope image at high magnification of one of the fabricated pillars is shown in Figure 5.3c. As can be seen, the deposit has a fairly uniform thickness from the base to the top. Slight variations of the pillar thickness and shape are most likely due to the polycrystalline nature of the deposit as also seen in pillars deposited by the FluidFM probe.[49] Potentially, the use of surfactants and additives could allow the fabrication of smoother nanoscale features and some tailoring of the aspect ratio. Interestingly, the structure diameter (400 – 600 nm) is about 10 times larger than the opening size of the pipette barrel (30 – 50 nm). In the jet-printing configuration of patterning with FluidFM probes the features patterned were at least three times thicker than the opening diameter of the probe.[49] This effect, for both methods, is attributed to the broadening of the interfacial concentration field of the confined precursor species at close probe-to-substrate distances. At least in part, this can be attributed to sluggish deposition kinetics compared to the mass transport rate, especially in relation to the nucleation and growth of copper on gold. The absence of any growth features, other than a deposited layer of copper at low substrate overpotential values (Figure 5.3a) also supports this hypothesis.

The technique outlined is capable of deposition of more complex 3D structures, which can be used further for optical and nanomechanical applications, as unconventional SPM probes and in nanoelectronic devices as interconnects.[1,58–60] Figure 5.4a shows two freestanding 25 μm and 27 μm – tall zigzag features (both structures are ~500 nm thick). These structures were grown by the deposition of a vertical pillar (3 μm in height), followed by the copper electroplating with a laterally translated nanopipette at a rate of 50 nm s^{-1}, which allowed the construction of a metal wire in a diagonal configuration, with each diagonal inclined at about 60 degrees with respect to the substrate. These structures arise from the retraction of the nanopipette (positional feedback) with the growing feature (rate of electrodeposition *ca.* 100 nm s^{-1}) and the simultaneous lateral movement of the probe. These two

factors determine the geometric characteristics of the resulting 3D shape and could easily be tuned.

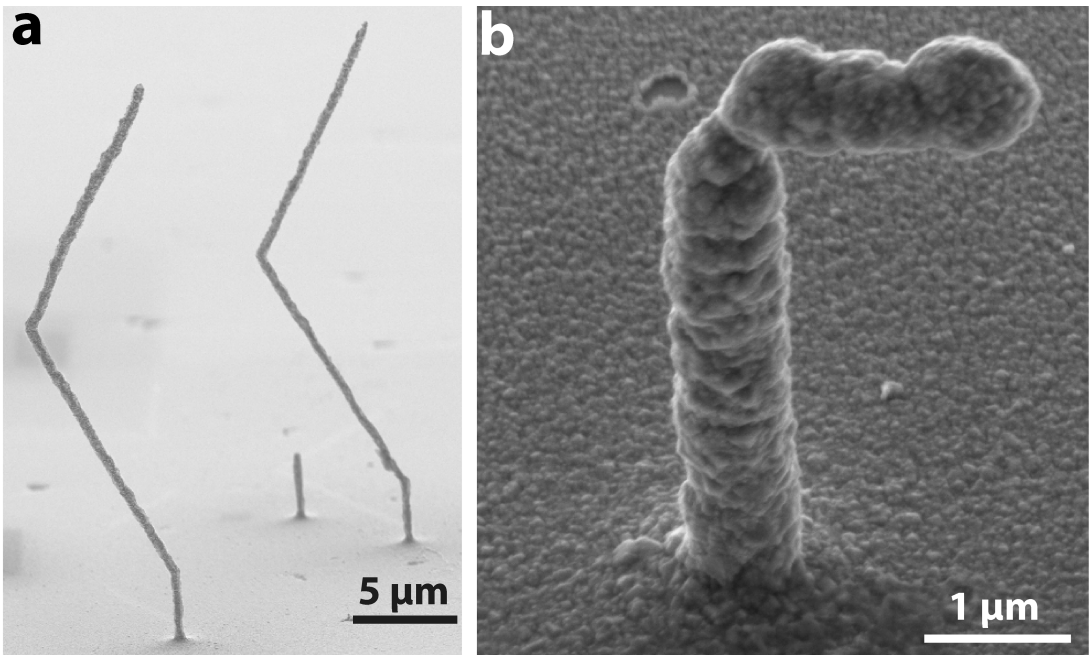

Figure 5.4. SEM images of complex 3D features fabricated with a dual-channel nanopipette. (a) Two zigzag structures, created by driving Cu^{2+} ions from the delivery channel at a bias of +0.7 V with positional SICM feedback (image taken at a 15° angle). The vertical pillar at the structure base was fabricated by holding the nanopipette for 45 s above the substrate (*i.e.* fixed x, y co-ordinate; feedback on z-position). Diagonal parts of the structure were deposited by translating the nanopipette for 6 µm laterally at 50 nm s^{-1}. (b) Fabricated Γ-like feature (image taken at a 45° angle), deposited at 0.75 V driving voltage. The top bar of the Γ was deposited by translating the nanopipette probe laterally at 40 nm s^{-1} without SICM positional feedback. The substrate was held at a potential E_{sub} = -0.75 V throughout. SICM barrels in both deposition experiments were biased at 0.2 V *vs*. QRCE in the solution bulk.

Finally, we point out that if positional feedback is turned off at certain points during patterning, and the probe is then translated laterally, Γ-like structures can be deposited. Figure 5.4b shows a fabricated freestanding Γ feature, consisting of a vertical (5.5 µm height) and horizontal (2.2 µm length) copper wire. Note that this is

about an order of magnitude thinner (800 nm in diameter) than a previously reported similar pattern, deposited with the microfluidic hollow AFM cantilever technique.[49]

The grown complex features were subjected to all the necessary sample manipulation and preparation (thorough rinsing, removal of the substrate from the sample holder, mounting on the holder for SEM, transfer to SEM) needed for further characterization, and no mechanical damage was observed on the fabricated objects. This confirms the reasonable mechanical stability of the features, which are likely to be mechanically similar to those fabricated by FluidFM.[49]

5.4.3 SICM Imaging of Fabricated Objects: In addition to fine control over surface modification, the nanopipette patterning method presented here also offers the possibility to map the patterned area using the imaging capabilities of the *same probe* as used for fabrication. The advantage of imaging the features immediately after the fabrication has several important benefits, such as: i) "quality control" after particular preparation steps in the multistep fabrication of complex objects; ii) almost immediate characterization, with a reasonably quick image acquisition time, with no need for *in-situ* sample manipulation/preparation for the use of other characterization techniques; and iii) the possibility of imaging materials that could be changed or modified outside the fabrication conditions (*e.g.* damaged in an electron beam, oxidized by oxygen present in the ambient atmosphere *etc*).

Figure 5.5a shows a 750 nm by 750 nm high-resolution SICM image (2500 pixels, 15 nm pixel pitch) of a copper pillar (as deposited height 2.83 ± 0.08 μm) obtained with a dual-barrel nanopipette of 100 nm total diameter (SICM barrel internal opening size was ~30 nm). A hopping mode was used as described in the Materials and Methods section. The image demonstrates the elliptic shape of the 2.95 μm μm-tall feature (measured by SICM) with *ca.* 400 and 500 nm dimensions along the semi-minor and semi-major axes. The pillar has some roughness on the side walls, similar to the other deposited structures (*e.g.* as in Figure 5.3c) and this structural characteristic is clearly visualized by SICM. It is important to note that imaging of such three-dimensional objects of high aspect ratio (tall and narrow, with vertical sidewalls) is a challenging task for most SPMs, including AFM, due to steric difficulties attributed to the geometry of the probes. An advantage of SICM probes is their high aspect ratio. We note that the FluidFM probe has a geometry designed for

fluid flow, rather than imaging, so that high resolution writing and reading is not possible.

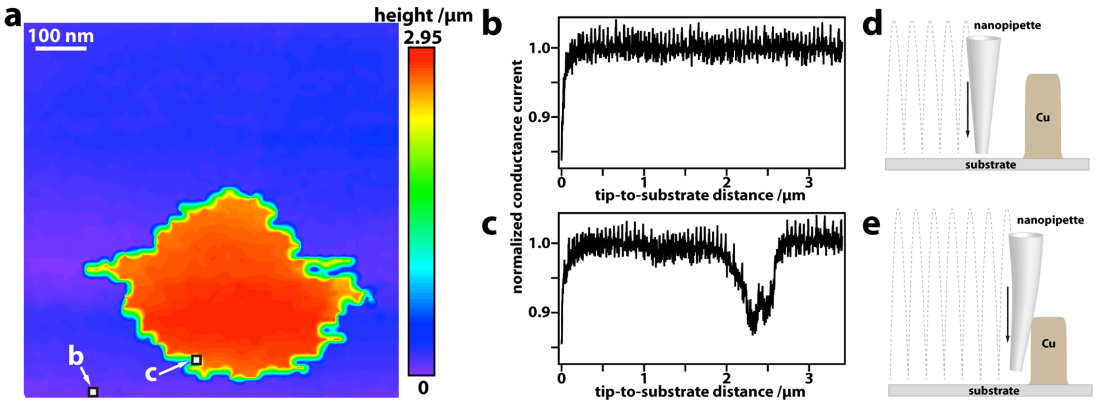

Figure 5.5. SICM mapping of deposits using the same probe. (a) Hopping mode SICM image (750 by 750 nm, 2500 pixels, 15 nm pixel pitch) of a deposited Cu pillar, taken with the *same nanopipette probe* as used for patterning (deposition at E_{sub} =-0.75 V, SICM bias 0.2 V, copper-barrel bias 0.7 V, 60 s). (b), (c) Probe approach curves recorded at positions "b" and "c" as marked on (a). Schematics in (d) and (e) illustrate possible nanopipette bending in (b) and (c), respectively.

Although SICM imaging with a nanopipette probe is feasible even on structures with such a shape as that shown in Figure 5.5a, particular care has to be taken to avoid probe-substrate crash. Figures 5.5b and 5.5c exhibit approach curves recorded during SICM topographical mapping. A classical SICM current-distance characteristic[50] (Figure 5.5b) is recorded over the flat featureless part of the substrate (pixel marked "b" in Figure 5.5a). Similar current-distance curves are recorded on the central part of the pillar (not shown). However, the current-distance response over the edges of the copper structure (*e.g.* marked "c" in Figure 5.5a) is rather different. Figure 5.5c shows such a current-distance characteristic, which exhibits two minima, one below the feedback set point (at the position of closest approach, 0 µm on the graph) and another slightly above the set point value (at a probe-to-substrate distance *ca.* 2.5 µm). The former minimum most likely indicates the vicinity of the probe to the flat part of the substrate, similar to the classical ion current response over the planar interface (as illustrated on Figure 5.5d). The latter minimum is attributed to the ion current magnitude drop due to the steric limitation

of the mass-transport in close proximity to the pillar (*i.e.* a vertical wall). The gradual flattening of the minimum indicates the change of the mutual arrangement of the nanopipette tip and the deposited structure and is most likely due to nanopipette bending. Indeed, this scenario is quite possible, taking into account the nanopipette semi-angle (about 8°) and the distance between pixels (15 nm), which means that mechanical contact between the probe and the copper pillar can be established (as shown schematically in Figure 5.5e), causing further probe/structure bending during the approach. Despite this issue, the SICM channel of the dual-function probe can generally be used for post-fabrication read-out of the deposited features.

5.5 Conclusions

This work has demonstrated the capabilities of double-barrel nanopipettes for highly controlled deposition of 3D structures, using Cu deposition as an exemplar material. The methodology is based on the electrochemical management of ionic fluxes for highly localized electrochemically-driven delivery and deposition, as well as for ion conductance regulation of the probe-to-substrate distance. This approach has been illustrated with the fabrication of simple (pillars) and more complex objects, such as free-standing zigzag and Γ-like structures. Advantages of the nanopipette technique include relatively straightforward operation, simple electrochemical control of delivery (without any need for a flow system), with simultaneous monitoring and feedback, and facile adjustment of the deposition parameters and growth rates by simultaneous tuning of the bias that drives precursor ions and the substrate potential.

As well as being able to produce (write) features, the same probe can be used to image (read) the deposited features using the powerful high-resolution imaging capacity of SICM. Furthermore, any difficulties of surface wettability and stability of meniscus-confined methods are overcome by operation under a thick layer of electrolyte solution. In principle, the technique should be capable of using the voxel-by-voxel fabrication strategy reported previously for the fabrication of even more complex object architectures[49] and should be compatible with the electroplating of a variety of materials, spanning conducting polymers, nanoparticles and metals. In this regard, it is important to point out the ease with which multi-barrel pipettes can be constructed,[61] which would enable the construction of multi-component structures, of spatially varying composition if desired, via (adaptive) potential-space-time control.

5.6 Supporting Information

5.6.1 Estimation of Cross-Contamination in the Nanopipette Barrels: Filling the double-barrel glass nanopipettes with electrolyte solutions of different composition may result in a cross-contamination of the solutions in the barrels from the liquid droplet formed at the probe tip. To estimate the degree of such contamination, a simple mathematical treatment can be developed. First of all, one can consider spherical diffusion of the species from the probe tip into the pipette. For simplicity, in the first approximation one can provide an estimate for the diffusion into a single-barreled pipette, as schematically illustrated in Figure 5.6.

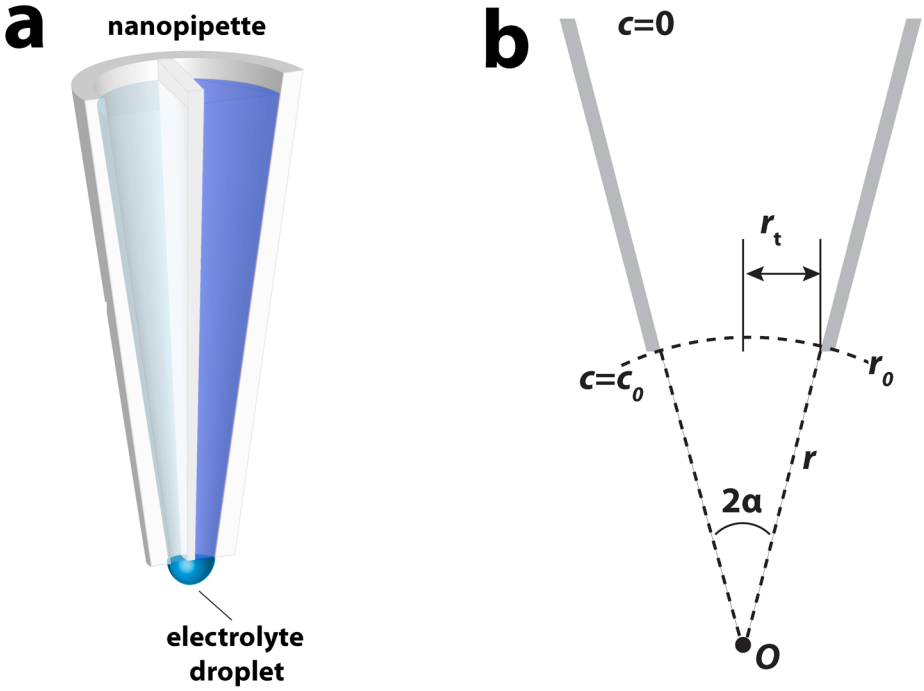

Figure 5.6. Formation of cross-contamination model. (a) Schematic representation of the double-barrel nanopipette with an electrolyte droplet at the tip. (b) Geometrical interpretation of the mass transport in the nanopipette with concentration boundary conditions for modeling.

The model reasonably assumes the flux conservation equation applies (only mass-transport, no chemical reactions involved):

$$\nabla J = 0 \qquad (5.1)$$

where J is the flux of species, given by the Fick's law:

$$J = -D\nabla c \tag{5.2}$$

and D and c denote the diffusion coefficient and species concentration, respectively. In spherical coordinates, (5.1) therefore reads:

$$-D\left(\frac{\partial^2 c}{\partial r^2} + \frac{2}{r}\frac{\partial c}{\partial r}\right) = 0 \tag{5.3}$$

The solution to (5.3) is:

$$c = -\frac{A}{r} + B \tag{5.4}$$

where the integration constants can be calculated from the boundary conditions $A = c_0 r_0$ and $B = 0$ as $c(r = r_0) = c_0$ and $c(r = \infty) = 0$; c_0 denotes bulk concentration in the droplet). Therefore, the complete solution to (5.3) reads:

$$c = \frac{c_0 r_0}{r} \tag{5.5}$$

The flux of species at $r = r_0$, obtained by differentiation of (5.5):

$$J = \frac{D c_0}{r_0} \tag{5.6}$$

allows the calculation of the amount of species entering the nanopipette within a time, t, taking into account the area, S, of a spherical cap at $r = r_0$. The concentration change caused by the cross-contamination (the pipette volume, V, can be estimated is the capillary dimensions are known, for example an internal diameter d = 0.9 mm and length l = 5 cm):

$$\Delta c = \frac{JS}{V}t = \frac{D c_0}{r_0}\frac{\pi(r_t^2 + (r_0 - r_0\cos a)^2)}{\pi(\frac{d}{2})^2 l}t \tag{5.7}$$

where a is the pipette semi-angle (8° herein) and r_0 is given as:

$$r_0 = \frac{r_t}{\sin a} \tag{5.8}$$

One can assume the time required to fill both pipette barrels to be about 300 s (typically, this value is even lower in real experimental practice) and the concentration of species (with D = 10^{-9} m^2 s^{-1}) in the liquid droplet at the tip of 1 M (which is, indeed, set very high, in order to calculate the upper limit of the cross-contamination effect). Under such assumptions, the concentration change due to the cross-contamination in the pipette reaches 82.9 μM. This is typically a negligible change for the 10s to 100s millimolar concentrations of electrolyte present in the nanopipette barrels.

5.7 References

(1) Hu, J.; Yu, M.-F. *Science* **2010**, *329* (5989), 313–316.

(2) Stewart, M. E.; Anderton, C. R.; Thompson, L. B.; Maria, J.; Gray, S. K.; Rogers, J. A.; Nuzzo, R. G. *Chem. Rev.* **2008**, *108* (2), 494–521.

(3) Xiang, Z.; Liu, J.; Lee, C. *Microsystems Nanoeng.* **2016**, *2*, 16012.

(4) Meng, D.; Erol, M.; Boccaccini, A. R. *Adv. Eng. Mater.* **2010**, *12* (9), B467–B487.

(5) Li, J.; Rozen, I.; Wang, J. *ACS Nano* **2016**, *10* (6), 5619–5634.

(6) De Angelis, F.; Malerba, M.; Patrini, M.; Miele, E.; Das, G.; Toma, A.; Zaccaria, R. P.; Di Fabrizio, E. *Nano Lett.* **2013**, *13* (8), 3553–3558.

(7) Yesilkoy, F.; Flauraud, V.; Ruegg, M.; Kim, B. J.; Brugger, J. *Nanoscale* **2016**, *8* (9), 4945–4950.

(8) Jesse, S.; Borisevich, A. Y.; Fowlkes, J. D.; Lupini, A. R.; Rack, P. D.; Unocic, R. R.; Sumpter, B. G.; Kalinin, S. V; Belianinov, A.; Ovchinnikova, O. S. *ACS Nano* **2016**, *10* (6), 5600–5618.

(9) Fisher, J. S.; Kottke, P. A.; Kim, S.; Fedorov, A. G. *Nano Lett.* **2015**, *15* (12), 8385–8391.

(10) Ke, Y.; Ong, L. L.; Shih, W. M.; Yin, P. *Science* **2012**, *338* (6111), 1177–1183.

(11) Han, D.; Pal, S.; Nangreave, J.; Deng, Z.; Liu, Y.; Yan, H. *Science* **2011**, *332*

(6027), 342–346.

(12) Meyer, E.; Hug, H. J.; Bennewitz, R. In *Scanning Probe Microscopy: The Lab on a Tip*; Springer: Berlin, Heidelberg, 2004; pp 15–44.

(13) Iwata, F.; Metoki, J. In *Manipulation, Manufacturing and Measurement on the Nanoscale (3M-NANO), 2014 International Conference on*; 2014; pp 304–307.

(14) Resch, R.; Baur, C.; Bugacov, A.; Koel, B. E.; Madhukar, A.; Requicha, A. A. G.; Will, P. *Langmuir* **1998**, *14* (23), 6613–6616.

(15) Zhao, J.; Swartz, L. A.; Lin, W.; Schlenoff, P. S.; Frommer, J.; Schlenoff, J. B.; Liu, G. *ACS Nano* **2016**, *10* (6), 5656–5662.

(16) Pires, D.; Hedrick, J. L.; De Silva, A.; Frommer, J.; Gotsmann, B.; Wolf, H.; Despont, M.; Duerig, U.; Knoll, A. W. *Science* **2010**, *328* (5979), 732–735.

(17) El-Giar, E. M.; Said, R. A.; Bridges, G. E.; Thomson, D. J. *J. Electrochem. Soc.* **2000**, *147* (2), 586–591.

(18) McGeouch, C.-A.; Peruffo, M.; Edwards, M. A.; Bindley, L. A.; Lazenby, R. A.; Mbogoro, M. M.; McKelvey, K.; Unwin, P. R. *J. Phys. Chem. C* **2012**, *116* (28), 14892–14899.

(19) Borgwarth, K.; Heinze, J. *J. Electrochem. Soc.* **1999**, *146* (9), 3285–3289.

(20) Laslau, C.; Williams, D. E.; Kannan, B.; Travas-Sejdic, J. *Adv. Funct. Mater.* **2011**, *21* (24), 4607–4616.

(21) Kim, J. T.; Seol, S. K.; Pyo, J.; Lee, J. S.; Je, J. H.; Margaritondo, G. *Adv. Mater.* **2011**, *23* (17), 1968–1970.

(22) Bruckbauer, A.; Ying, L.; Rothery, A. M.; Zhou, D.; Shevchuk, A. I.; Abell, C.; Korchev, Y. E.; Klenerman, D. *J. Am. Chem. Soc.* **2002**, *124* (30), 8810–8811.

(23) Bruckbauer, A.; Zhou, D.; Ying, L.; Korchev, Y. E.; Abell, C.; Klenerman, D. *J. Am. Chem. Soc.* **2003**, *125* (32), 9834–9839.

(24) Iwata, F.; Nagami, S.; Sumiya, Y.; Sasaki, A. *Nanotechnology* **2007**, *18* (10), 105301.

(25) So, I.; Futoshi, I. *Jpn. J. Appl. Phys.* **2011**, *50* (8S3), 08LB15.

(26) Abhijit, P. S.; Min-Feng, Y. *Nanotechnology* **2007**, *18* (10), 105305.

(27) Zhou, M.; Yu, Y.; Blanchard, P.-Y.; Mirkin, M. V. *Anal. Chem.* **2015**, *87* (21), 10956–10962.

(28) Suryavanshi, A. P.; Yu, M.-F. *Appl. Phys. Lett.* **2006**, *88* (8), 83103.

(29) Müller, A.-D.; Müller, F.; Hietschold, M. *Appl. Phys. A* **1998**, *66* (1), S453–S456.

(30) Müller, A. D.; Müller, F.; Hietschold, M. *Thin Solid Films* **2000**, *366* (1–2), 32–36.

(31) Zhang, H.; Wu, L.; Huang, F. *J. Vac. Sci. Technol. B* **1999**, *17* (2), 269–272.

(32) Lesch, A.; Vaske, B.; Meiners, F.; Momotenko, D.; Cortes-Salazar, F.; Girault, H. H.; Wittstock, G. *Angew. Chem., Int. Ed.* **2012**, *51* (41), 10413–10416.

(33) ul Haq, E.; Liu, Z. M.; Zhang, Y. A.; Ahmad, S. A. A.; Wong, L. S.; Armes, S. P.; Hobbs, J. K.; Leggett, G. J.; Micklefield, J.; Roberts, C. J.; Weaver, J. M. R. *Nano Lett.* **2010**, *10* (11), 4375–4380.

(34) Vettiger, P.; Despont, M.; Drechsler, U.; Durig, U.; Haberle, W.; Lutwyche, M. I.; Rothuizen, H. E.; Stutz, R.; Widmer, R.; Binnig, G. K. *IBM J. Res. Dev.* **2000**, *44* (3), 323–340.

(35) Loh, O. Y.; Ho, A. M.; Rim, J. E.; Kohli, P.; Patankar, N. A.; Espinosa, H. D. *Proc. Natl. Acad. Sci. U. S. A.* **2008**, *105* (43), 16438–16443.

(36) Aaronson, B. D. B.; Güell, A. G.; McKelvey, K.; Momotenko, D.; Unwin, P. R. In *Nanoelectrochemistry*; CRC Press, 2015; pp 655–694.

(37) Kang, M.; Momotenko, D.; Page, A.; Perry, D.; Unwin, P. R. *Langmuir* **2016**, *32*, 7993–8008.

(38) Momotenko, D.; McKelvey, K.; Kang, M.; Meloni, G. N.; Unwin, P. R. *Anal. Chem.* **2016**, *88* (5), 2838–2846.

(39) Momotenko, D.; Byers, J. C.; McKelvey, K.; Kang, M.; Unwin, P. R. *ACS Nano* **2015**, *9* (9), 8942–8952.

(40) Perry, D.; Al Botros, R.; Momotenko, D.; Kinnear, S. L.; Unwin, P. R. *ACS Nano* **2015**, *9* (7), 7266–7276.

(41) McKelvey, K.; Kinnear, S. L.; Perry, D.; Momotenko, D.; Unwin, P. R. *J. Am. Chem. Soc.* **2014**, *136* (39), 13735–13744.

(42) Perry, D.; Paulose Nadappuram, B.; Momotenko, D.; Voyias, P. D.; Page, A.; Tripathi, G.; Frenguelli, B. G.; Unwin, P. R. *J. Am. Chem. Soc.* **2016**, *138* (9), 3152–3160.

(43) McKelvey, K.; O'Connell, M. A.; Unwin, P. R. *Chem. Commun.* **2013**, *49*

(29), 2986–2988.

(44) Rodolfa, K. T.; Bruckbauer, A.; Zhou, D.; Korchev, Y. E.; Klenerman, D. *Angew. Chem., Int. Ed.* **2005**, *44* (42), 6854–6859.

(45) An, S.; Sung, B.; Noh, H.; Stambaugh, C.; Kwon, S.; Lee, K.; Kim, B.; Kim, Q.; Jhe, W. *Nano-Micro Lett.* **2014**, *6* (1), 70–79.

(46) Futoshi, I.; Yosuke, S.; Akira, S. *Jpn. J. Appl. Phys.* **2004**, *43* (7S), 4482.

(47) Gabi, M.; Behr, P.; Studer, P.; Niedermann, P.; Bitterli, J.; Liley, M.; Heinzelmann, H.; Zambelli, T.; Meister, A.; Gabi, M.; Behr, P.; Studer, P.; Vörös, J.; Niedermann, P.; Bitterli, J.; Polesel-Maris, J.; Liley, M.; Heinzelmann, H.; Zambelli, T. *Nano Lett.* **2009**, *9* (6), 2501–2507.

(48) Hirt, L.; Gruter, R. R.; Berthelot, T.; Cornut, R.; Voros, J.; Zambelli, T.; Grüter, R. R.; Berthelot, T.; Cornut, R.; Vörös, J.; Zambelli, T.; Grüter Raphael, R.; Berthelot, T.; Cornut, R.; Vörös, J.; Zambelli; Tomaso. *RSC Adv.* **2015**, *5* (103), 84517–84522.

(49) Hirt, L.; Ihle, S.; Pan, Z.; Dorwling-Carter, L.; Reiser, A.; Wheeler, J. M.; Spolenak, R.; Vörös, J.; Zambelli, T. *Adv. Mater.* **2016**, *28* (12), 2311–2315.

(50) Chen, C.-C.; Zhou, Y.; Baker, L. A. *Annu. Rev. Anal. Chem.* **2012**, *5* (1), 207–228.

(51) Hansma, P. K.; Drake, B.; Marti, O.; Gould, S. A.; Prater, C. B. *Science* **1989**, *243*, 641–643.

(52) Perry, D.; Momotenko, D.; Lazenby, R. A.; Kang, M.; Unwin, P. R. *Anal. Chem.* **2016**, *88* (10), 5523–5530.

(53) Sa, N.; Baker, L. A. *J. Electrochem. Soc.* **2013**, *160* (6), H376–H381.

(54) Shevchuk, A. I.; Gorelik, J.; Harding, S. E.; Lab, M. J.; Klenerman, D.; Korchev, Y. E. *Biophys. J.* **2001**, *81* (3), 1759–1764.

(55) Li, C.; Johnson, N.; Ostanin, V.; Shevchuk, A.; Ying, L.; Korchev, Y.; Klenerman, D. *Prog. Nat. Sci.* **2008**, *18* (6), 671–677.

(56) Wei, C.; Bard, A. J.; Feldberg, S. W. *Anal. Chem.* **1997**, *69* (22), 4627–4633.

(57) Momotenko, D.; Cortes-Salazar, F.; Josserand, J.; Liu, S.; Shao, Y.; Girault, H. H. *Phys. Chem. Chem. Phys.* **2011**, *13*, 5430–5440.

(58) Butt, F. K.; Cao, C.; Khan, W. S.; Safdar, M.; Fu, X.; Tahir, M.; Idrees, F.; Ali, Z.; Nabi, G.; Yu, D. *CrystEngComm* **2013**, *15* (11), 2106–2112.

(59) Zhou, X. T.; Sham, T. K.; Shan, Y. Y.; Duan, X. F.; Lee, S. T.; Rosenberg, R.

A. *J. Appl. Phys.* **2005**, *97* (10), 104315.

(60) Göring, G.; Dietrich, P.-I.; Blaicher, M.; Sharma, S.; Korvink, J. G.; Schimmel, T.; Koos, C.; Hölscher, H. *Appl. Phys. Lett.* **2016**, *109* (6), 63101.

(61) Nadappuram, P. B.; McKelvey, K.; Byers, J. C.; Güell, A. G.; Colburn, A. W.; Lazenby, R. A.; Unwin, P. R. *Anal. Chem.* **2015**, *87* (7), 3566–3573.

6 Conclusions and Outlook

This thesis demonstrates the rise of SICM as an increasingly powerful tool for the investigation of solid-liquid interfaces. In addition to the topographical imaging for which it has been most widely used, the ionic current measured during an SICM experiment is shown to be highly sensitive to a range of additional interfacial phenomena, including cellular uptake, surface charge density and electrochemical reactions. Developments in both the nanopipette configuration and the potential-control function used, allow these phenomena to be probed directly, and their contribution to the SICM signal extracted using FEM simulations. This combination of experimental and theoretical approaches significantly extends the scope of SICM, allowing quantitative, multifunctional imaging of both biological and inert surfaces.

Chapter 2 described the development of a SICM-SECM device capable of simultaneously mapping the topography and molecular uptake of a viable cell. By localising a molecule of interest to the open barrel of the dual-channel probe, nanoscale uptake measurements can be taken at an array of points on the cell surface, a setup tested on the model system of hexaammineruthenium(III) and *Zea mays* root hair cells. In this system, the SICM-SECM probe had the precision to differentiate between the uptake rates of several subcellular regions, and these qualitative experimental differences were then quantified using FEM simulations.

The SICM-SECM probe used in Chapter 2 has considerable potential for further uptake studies, as the careful design of both the material used for the SECM electrode and the potential applied to that electrode would allow any electrochemically active molecule to be detected. Herein, hexaammineruthenium(III) was chosen due its favourable outer-sphere electron transfer kinetics, but the setup would be very similar for the study of molecules such as oxygen (O_2), commonly detected via a reduction reaction. One area of research to which this study could be particularly applicable is pharmaceutical design. Many drugs, particularly those that selectively cause cell death, operate via the disruption of some intracellular pathway. There are therefore two requirements of an effective drug molecule: (i) ability to cross the cellular membrane; and (ii) effective disruption of the desired pathway within the cell. The majority of assays currently used to test drug efficacy do not separate these two factors, considering large populations of cells and the percentage

of that population that have undergone cell death after the application of some concentration of a drug. SICM-SECM could be used to deconvolute these two aspects of drug design by extracting quantitative values of the uptake rate constant for a range of molecules. This would add an additional optimisation step to the design process, as some drugs that have high intracellular activity may only require small structural changes in order to cross the lipid bilayer effectively. Initial studies could validate the technique by screening of an array of electroactive molecules via repeated approach curves to the surface of several cell types. In addition to the cellular application discussed above, SICM-SECM could also be used to study 'uptake' at synthetic membranes, separating topography and molecular transport in a setup analogous to P-SICM.

The second approach to multifunctional SICM, in which the traditional single-channel nanopipette is used in combination with a carefully designed potential-control function, was introduced in Chapter 3. Previous studies had shown the potential of SICM as a technique to measure interfacial charge density and topography simultaneously. This capability was significantly enhanced in Chapter 3, with both the feedback type (for topographical mapping) and the voltage regime (for charge mapping) optimised to reduce the pixel acquisition time from over 5 s to less than 500 ms. This improved regime was then applied to both polymeric and cellular substrates, revealing previously unreported nanoscale heterogeneities in surface charge density.

The developments presented in Chapter 3 significantly increase the feasibility of SICM charge mapping as a technique. In the previous regime, the time taken to acquire a scan, coupled with the low pixel density of that scan, were not in line with what has come to be expected of scanning probe methodologies. However, the advances herein only increase the pixel acquisition time by several tens of milliseconds when compared to purely topographical SICM, allowing images of a high quality to be attained on a timescale comparable to conventional ion conductance microscopy. As with Chapter 2, Chapter 3 is a proof of concept study of a method that could be used in a diversity of systems. The wide range of electrolyte concentrations in which SICM charge mapping has been shown to function allow it to be applied to almost any solid-liquid interface at which a charge is presented. The ability to correlate structure and function could be further advanced by performing

uptake or charge mapping experiments in tandem with a complimentary technique such as confocal microscopy. Such an approach would allow the more accurate rationalisation of biological phenomena from the SICM data. In addition to these applications, advancements in both electronics (faster piezoelectric positioners and current followers) and probe manufacture (smaller aperture nanopipettes) would increase the power of the technique further, as higher resolution and pixel density could be achieved. However, smaller nanopipettes suffer from an increased contribution of the nanopipette surface charge on the ionic current measured, and thus the probes may have to be treated with a process such as silanisation in order to successfully extract the substrate charge density.

Chapter 4 also developed multifunctional imaging with a single-barrel nanopipette. While it presented simultaneous topography-charge and topography-reaction maps of both cellular and electrode substrates, the primary advancement was a complete consideration of the potential differences in the SICM system, and the tuning of those potentials to optimise imaging. The standard SICM setup, in which both the probe and the bath contain the same electrolyte solution, was perturbed such that the probe and bath contained solutions of different composition and concentration. FEM simulations were used to demonstrate that in such a 'differential concentration' setup, the electric field at the end of the nanopipette was significantly reduced, limiting the potential damage to delicate samples such as living cells. In addition, a full treatment of the importance of electroosmotic flow on the ionic current measured in an SICM experiment was also included.

The consideration of all of the potential differences in SICM discussed in Chapter 4 provides a more generalised outlook on the technique. Previous theoretical treatments of SICM have assumed that the electrolyte solution in the probe and the bath are the same, and those studies in which the compositions are not the same have not taken this difference into account when applying an external voltage. This work provides a platform upon which future theoretical investigations can be built, particularly with regard to the optimisation of experimental conditions for a desired functional purpose. An example of such an application would be the quantitative delivery of molecules from a nanopipette. If some species is to be brought to a surface via a scanning probe, then the solutions inside and outside of that probe will

necessarily be of differing composition, and this should be taken into account when calculating the rate of delivery.

As in Chapter 2, Chapter 5 demonstrated the use of a dual-barrel nanopipette as a multifunctional tool. In this study, both barrels of the probe were left open to the bulk solution, one as a source of Cu^{2+} ions and the other for topographical feedback, which together facilitated the deposition of microscale 3D copper structures on a gold surface. The rate and localisation of the deposition were shown to be dependent on the voltage applied to the surface, and variation of the probe feedback regime allowed the deposition of both simple (pillar) and complex (zig-zag) structures with high aspect ratios. The flexibility of SICM was then utilised to read out the topography of the structures using the same probe that had been used to deposit them.

The theta-pipette deposition protocol outlined in Chapter 5 holds several advantages over conventional 3D printing setups. Firstly, the resolution is significantly higher than in other systems. Structures deposited herein routinely achieved a critical dimension of less than one micron, while macroscale resin printing creates layers around 100 μm thick, and FluidFM has a limiting resolution of around 10 μm. Future work may focus on increasing the resolution of deposition further still, either by reducing the size of the nanopipette used or by using a smaller probe-substrate separation in order to restrict the diffusion-limited deposition footprint. A second advantage of 3D printing with electrochemical deposition is that it does not require the integration of a microfluidic system into the probe, making it less prone to blocking. However, in order to compete with other 3D printing techniques, future work should focus on layer-by-layer deposition, as a development on the column-based printing herein. Increasing the flexibility of electrochemical deposition would make it a formidable tool for nanoscale fabrication.

In summary, this thesis provides examples of several different routes towards multifunctional imaging with SICM, highlighting its flexibility both as a standalone technique, and when integrated into a multi-channel probe. When combined with FEM simulations, it is capable of creating quantitative maps of a variety of surface phenomena. As probe fabrication and scanning regimes are improved, the scope of SICM will only increase further, making it an ever more powerful tool than can be applied to functional imaging in a diverse array of systems.